DEPARTAMENTO DE ASTROFÍSICA

Universidad de La Laguna

Optical spectroscopy as a tracer of accretion processes in transient X-ray binaries

Thesis submitted by
D. Felipe Jiménez Ibarra
As a requirement for the degree of
Doctor by the University of La Laguna

INSTITUTO D ASTROFISÍCA D CANARIAS
December 2019

Examination date: January 17, 2020
Thesis supervisor: Dr. Teodoro Muñoz Darias
Prof. Jorge Casares Velázquez

ISBN: xx-xxx-xxxx-x
Depósito legal: TF-xxxx/2018

A mis padres,
a Cris y Lucas.

Resumen

Las binarias de rayos X son sistemas estelares compuestos por una estrella de neutrones o un agujero negro que acrece por incorporación de masa proveniente de una estrella compañera. El material transferido transporta momento angular, lo que de manera natural hace que se forme un disco de acreción alrededor del objeto compacto. Allí, las fuerzas disipativas transforman la energía potencial del gas en calor. En el proceso el gas se va moviendo hacia el interior a medida que el disco se calienta. Este mecanismo es más eficiente en las regiones internas del disco, donde las temperaturas alcanzan los $\sim 10^7$ K, y así la mayor parte de la energía es liberada en el rango de los rayos X.

Las binarias de rayos X son las fuentes persistentes más brillantes del cielo en dicha banda espectral. Fueron descubiertas a mediados del siglo XX en los primeros días de la astronomía de rayos X, abriendo una nueva vía para el estudio observacional no sólo de la física de los objetos compactos, sino también de los procesos de acreción en el régimen de campos gravitatorios intensos. Tienen la ventaja de ser en su mayoría objetos galácticos, de manera que están cerca (en comparación con los núcleos activos de galaxias o cuásares) y por lo tanto son más brillantes y fáciles de estudiar. Además, presentan variabilidad en tiempos característicos accesibles a las vidas humanas (desde fracciones de segundo a años). Aunque son fuentes brillantes en rayos X, algunos de los progresos más importantes en el campo de las las binarias de rayos X surgieron de estudios en distintas longitudes de onda a lo largo de todo el espectro electromagnético.

En esta tesis analizaremos tres fuentes catalogadas como binarias de rayos X poco masivas (LMXB, por sus siglas en inglés); una subclase de binaria de rayos X donde la estrella compañera es menos masiva que el Sol. Utilizaremos la espectroscopía óptica como herramienta principal para el estudio de distintas propiedades del disco de acreción, incluyendo parámetros de escala (como su radio y extensión vertical), así como las eyecciones de masa desde el disco en forma de vientos, íntimamente ligadas al proceso de acreción.

En el primer trabajo presentamos el análisis de MAXI J1807+132, una LMXB transitoria descubierta durante una erupción en 2017. El estudio se basa en observaciones en el rango óptico y en rayos X realizadas a lo largo de más de 125 días durante el declive de este evento. Discutimos algunas características importantes de MAXI J1807+132 como su distancia, el tipo espectral de la estrella compañera, el tamaño del disco de acreción, y la naturaleza del objeto compacto en base a la fenomenología observada y por comparación con otros sistemas.

En el segundo trabajo estudiamos Aquila X-1, una LMXB con estrella de neutrones que muestra erupciones regulares cada dos años aproximadamente. Utilizando el Gran Telescopio Canarias realizamos un seguimiento espectroscópico óptico durante tres erupciones consecutivas (en 2011, 2013 y 2016), obteniendo 65 espectros que muestrean el ciclo orbital completo. Esto

nos permitió medir la velocidad radial, $K_{\rm em}$, que traza el movimiento de la cara irradiada de la estrella compañera. Para ello, aplicamos la técnica de tomografía Doppler utilizando las líneas estrechas de la mezcla de Bowen. Basándonos en la $K_{\rm em}$ medida, y en combinación con otros parámetros dinámicos del sistema, realizamos un análisis de Monte Carlo para determinar empíricamente el ángulo de apertura del disco de acreción por primera vez.

Finalmente, obtuvimos fotometría y espectroscopía óptica de alta resolución temporal de Swift J1357.2–0933 durante la erupción de 2017. Descubierto en 2011, este sistema transitorio es una LMXB con agujero negro que se caracteriza por mostrar caídas de brillo (conocidas en inglés como *dips*) cuasi periódicas en su curva de luz en el visible. Estos son, además, de corta duración (tiempo característico de minutos) y se repiten con una cuasi periodicidad creciente a medida que la erupción decae. En nuestro estudio utilizamos el Gran Telescopio Canarias para resolver espectroscópicamente los *dips* por primera vez. Observamos absorciones desplazadas hacia el azul durante los *dips* que demuestran que estos están asociados con vientos fríos (poco ionizados). Discutimos las propiedades y el posible mecanismo de producción de estas eyecciones.

Esta tesis muestra el potencial de la espectroscopía óptica, complementada con datos de rayos X, para limitar la naturaleza de las binarias de rayos X, así como las propiedades de sus discos de acreción y las eyecciones de masa asociadas. Los tres trabajos aquí presentados se publicaron en Monthly Notices of the Royal Astronomical Society entre los años 2018 y 2019.

Abstract

X-ray binaries are stellar systems composed of a neutron star or a black hole that accretes mass from a companion star. The transferred material carries angular momentum and an accretion disc is naturally formed around the compact object. There, the dissipative forces transform the potential energy of the gas into heat. In the process, the gas moves inward as the disc heats up. This mechanism is most efficient in the inner regions, where the temperature reaches $\sim 10^7$ K and most of the energy is released in X-rays.

X-ray binaries are the brightest persistent sources of the X-ray sky. They were discovered in the early days of X-ray astronomy, in the mid-20th century, opening a new avenue to the observational study not only, of the physics of compact objects, but also of accretion processes in the strong gravity regime. They have the advantage of being mostly Galactic objects; they are nearby (compared to active galactic nuclei or quasi-stellar objects) and thus brighter and easier to study. In addition, they present variability on timescales accessible to human lives (from fractions of a second to years). Although X-ray binaries are bright X-ray sources, some of the most important progress in the field has come from multi-wavelength studies.

In this thesis we will analyse three sources catalogued as low-mass X-ray binaries (LMXB), a subclass of X-ray binaries where the companion star is less massive than the Sun. We will use optical spectroscopy as the main tool for studying different properties of the accretion disc, going from scale parameters (radial size and vertical extent) to disc related outflows, which are intimately linked to the accretion process.

The first work presents the analysis of MAXI J1807+132, a transient LMXB discovered in 2017 during an outburst episode. The study is based on X-ray and optical observations spanning over 125 days during the decline of this event. We discuss some important characteristics of MAXI J1807+132 like its distance, the companion star spectral type, the accretion disc size, and the nature of the compact object on the basis of the observed phenomenology and by comparison with other systems.

In the second work we study Aquila X-1, a neutron-star LMXB that shows regular outbursts about every two years. We used the Gran Telescopio Canarias to carry out an optical spectroscopic follow-up during three consecutive outbursts (2011, 2013, and 2016), obtaining 65 spectra that sample the entire orbital cycle. This allowed us to measure the $K_{\rm em}$ velocity, which traces the motion of the irradiated face of the companion star. We achieved this by applying the Doppler tomography technique to the narrow lines of the Bowen blend. Based on the measured $K_{\rm em}$, and in combination with other dynamical parameters of the system, we carried out a Monte Carlo analysis to empirically determine the accretion disc opening angle for the first time.

Finally, we present high-time resolution optical spectroscopy and imaging of Swift J1357.2–0933 during its 2017 outburst. Discovered in 2011, this transient system is a black-hole LMXB characterised by showing quasi-periodic optical dips in its light curve. These features have short durations (timescale of minutes) and repeat with increasing quasi-periodicity as the outburst decays. In our work, we used the Gran Telescopio Canarias to spectroscopically resolve the dips for the first time. We observe blue-shifted absorptions during these dips, that demonstrate that these features are associated with cold (low ionisation) winds. We discuss the properties of this outflow and the possible wind launching mechanism.

This thesis shows the potential of optical spectroscopic studies complemented by X-ray data to constrain the nature of X-ray binaries as well as the properties of the X-ray heated discs and associated outflows. The three works presented here have been published in Monthly Notices of the Royal Astronomical Society between 2018 and 2019.

Contents

1

Introduction

THE development of X-ray astronomy in the second half of the 20th century brought to light a new population of high-energy sources, witnesses of an extreme Universe. The brightest X-ray source in the sky, Scorpius X-1 (Sco X-1), was discovered by Giacconi et al. (1962), who used X-ray detectors on board rockets in sub-orbital flights in order to surmount atmospheric opacity at these wavelengths.

Sandage et al. (1966) first identified the optical counterpart of Sco X-1, but it was Shklovsky (1967) who, after analysing this observation, suggested accretion as a source of power by extension of the same idea proposed for quasars by Salpeter (1964) and Zel'dovich (1964).

In the following years, the launch of Uhuru, the first astronomy-dedicated X-ray satellite, led to hundreds of detections. In addition, this allowed follow up of already known X-ray sources. A data set spanning a year of Centaurus X-3 observations revealed the existence of X-ray pulsations, which hinted at the binary nature of (at least) some of these objects (Schreier et al., 1972).

After more than 50 years of X-ray astronomy up to 300 X-ray binaries have been discovered, including both galactic and extragalactic objects (e.g. Liu et al., 2006, 2007). Sco X-1, the prototype X-ray binary, is still the brightest persistent X-ray source, although it is sometimes outshone by transient events (e.g. gamma-ray bursts; Ackermann et al., 2014).

The standard picture defines X-ray binaries as systems comprising a compact stellar remnant, either a black hole (BH) or a neutron star (NS), accreting material from a *regular* companion star. The gas forms an accretion disc around the accretor, where it is heated up to 10^7 K because of the friction caused by differential rotation in the gravitational well of the compact object. The thermal energy is radiated mainly in the X-ray regime, reaching luminosities in the range $L_{\rm X} \sim 10^{31}$–10^{39} erg s^{-1}. X-ray binaries provide a unique context in which both the compact object and the strong-field accretion physics are observationally revealed.

In the pursuit of a comprehensive understanding of these systems, the exploitation of the full range of the electromagnetic spectrum is mandatory. We dedicate this thesis to studying, using an optically based approach, some of the fundamental parameters of X-ray binary accretion discs.

1.1 X-ray binary classification

X-ray binaries are generally classified according to the mass of the companion star (also referred to as the "donor"). High-mass X-ray binaries (HMXBs) contain an early type (O-B) massive ($M \gtrsim 10M_{\odot}$) donor, which dominates the optical emission ($L_{\rm opt}/L_{\rm X} > 1$). They belong to a young population, mainly distributed in the Galactic plane (Coleiro & Chaty, 2013). These objects typically show long binary periods of the order of days.

Low-mass X-ray binaries (LMXBs) host a low-mass ($M \lesssim 1M_{\odot}$), late-type (K-M) secondary star. They may comprise a main sequence star, an evolved star, or white a dwarf, whose emission is generally outshone by that of the accretion disc ($L_{\rm opt}/L_{\rm X} \sim 0.001$). They are systems with short orbital periods (typically a few hours) and are associated with an old population, mostly distributed in the galactic bulge and in globular clusters (Grimm et al., 2002).

There are two mechanisms through which mass transfer can occur between the components in a binary system. Their efficiency depends on the nature of the donor. In HMXBs, mass is transferred mainly by ultraviolet-driven stellar winds. These are produced by radiation pressure in the external layers of the luminous, supergiant companion, and can account for mass loss rates as high as $10^{-5}M_{\odot}$ yr^{-1}. In the case of LMXBs, such strong stellar winds are not produced by the late-type companion. Instead, the accretion disc is fed by gas that overflows the gravitational well of the secondary star, as we outline in Sec. 1.2.1.

In the range of masses between these two groups systems are classified as intermediate-mass X-ray binaries (IMXBs). Three IMXBs with accreting BHs have been identified so far (V4641 Sgr, GRO J1655–40, and 4U 1543–475) but only one with an accreting NS: Her X-1, a system harbouring a $\sim 2\ M_{\odot}$ donor (Reynolds et al., 1997). The lack of an IMXB population with NSs could be explained in terms of a selection effect derived from the properties of the mass transfer mechanisms in this mass range. On the one hand, Roche-lobe overflow is unstable in NS IMXBs (see Sec. 1.3) and occurs on very short timescales ($\sim 10^7$ yr; Kalogera & Webbink, 1996), until the companion star loses a large fraction of its mass. This makes these systems unlikely to be observed. On the other hand, stellar winds in an intermediate-mass companion are not powerful enough to efficiently feed the accretion disc if the companion is not filling its Roche lobe. This results in low X-ray luminosities, which are difficult to detect.

As a result, practically all the known X-ray binaries are classified as either HMXBs or LMXBs. This thesis will focus on LMXB systems.

1.2 The Roche potential

The effective gravitational potential of an LMXB is described by the Roche potential. It is obtained by combining the gravitational attraction with the centrifugal force, while assuming that the components are moving in circular orbits around their common centre of mass. In a frame of reference with the origin in the centre of mass that corotates with the binary, the Roche potential per unit mass in Cartesian coordinates is given by:

$$\Phi_{\rm R}(x,y,z) = -\frac{GM_1}{\sqrt{(x+a\mu)^2+y^2+z^2}} - \frac{GM_2}{\sqrt{(x-a+a\mu)^2+y^2+z^2}} - \frac{1}{2}\omega^2\left(x+y\right)^2 \qquad (1.1)$$

where M_1 and M_2 are the masses of the components, a the binary separation, ω the angular velocity of the binary and $\mu = M_2/(M_1+M_2)$.

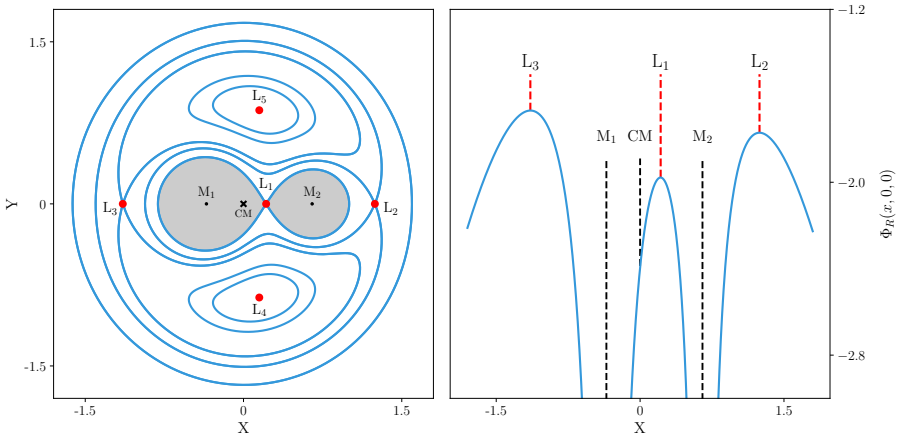

FIGURE 1.1— Roche potential per unit mass (Eq. 1.1) set to $G = 1$, $a = 1$, $M_1 + M_2 = 1$ and $P = 2\pi$. Left panel: intersection of some representative equipotential surfaces with the binary orbital plane ($z = 0$). Right panel: potential along the line joining the two components ($y = z = 0$).

Within this potential, the points with the same Φ_R value define an equipotential surface (see Fig. 1.1). There are four local maxima of Φ_R; these are saddle points where the gravitational force exerted over a test particle is perfectly balanced by the centrifugal force of the orbit at this position. These are the Lagrangian points, labelled L_{1-4} in Fig. 1.1. The equipotential surface that passes through the inner Lagrangian point (L_1) defines two drop-shape volumes called Roche lobes around each component of the system. The matter orbiting inside a Roche lobe is gravitationally bound to the star contained in it. Thus, the easiest way for mass to be transferred between the two stars in the binary is through the L_1 point, where the two Roche lobes are in contact. Note that if one of the stars eventually fills its Roche lobe, its surface will be distorted from the spherical in a tear-drop-shape following an equipotential of Φ_R.

The size of the Roche lobe will be completely determined by a and the mass ratio of the components ($q = M_2/M_1$). In the range of mass ratios relevant to LMXBs ($0.1 \lesssim q \lesssim 0.8$) the Paczyński approximation (Paczyński, 1971) yields:

$$\frac{R_2}{a} \simeq \frac{2}{3^{3/4}} \left(\frac{q}{1+q} \right)^{1/3} \tag{1.2}$$

where R_2 is the equivalent Roche lobe radius, defined as the radius of the sphere that contains the same volume as the Roche lobe around M_2. Note that Eq. 1.2 implies that the mass transfer in accreting binaries has a direct effect on the Roche lobe size, since q, and also a, will change in the conservative case (i.e. when the total mass and angular momentum are kept constant).

1.2.1 Roche lobe overflow

In order to quantitatively study how mass transfer affects the Roche lobe size, we are going to consider a system where a donor star of mass M_2 is transferring matter ($\dot{M}_2 < 0$) by overflowing its Roche lobe onto an accreting star of mass M_1. If the total mass is conserved ($\dot{M}_1 + \dot{M}_2 = 0$), the evolution of R_2 can be derived from Eq. 1.2 (Frank et al., 1992):

$$\frac{\dot{R}_2}{R_2} = \frac{2\dot{J}}{J} - \frac{2\dot{M}_2}{M_2}\left(\frac{5}{6} - q\right) \tag{1.3}$$

where $J = M_1 M_2 \sqrt{Ga/(M_1 + M_2)}$ is the total angular momentum.

According to Eq. 1.3, in a conservative scenario ($\dot{J} = 0$), $q = 5/6$ sets two different cases:

$q > 5/6$. The Roche lobe of the donor shrinks because of the mass loss. In addition, the donor star expands because it is driven out of thermal equilibrium. Therefore, the Roche lobe shrinkage and donor expansion will further enhance mass transfer, which in turn will shrink the Roche lobe in a runaway process. The violent overflowing proceeds on thermal timescales ($\sim 10^7$ years; Kalogera & Webbink, 1996) until the mass transfer makes $q < 5/6$. The angular momentum loss will exacerbate this process. Note that such unstable episode always takes place when mass flows from the more massive to the less massive star.

$q < 5/6$. In this case, the Roche lobe will expand as result of the mass transfer. Thus, to maintain mass transfer, it will be necessary that either (i) the system loses angular momentum to balance the second term in Eq. 1.3, or (ii) the donor star expands as a consequence of its evolution, moving in step with a swelling Roche lobe. In both these situations, or even in a combination of them, mass transfer can take place in a stable way; that is, sustained during a relatively long period of time.

As will be discussed in the next section, both cases are thought to be involved in different stages during the formation and evolution of LMXBs. However, the observation of 'steady' X-ray sources implies that most LMXBs stay in a stable mass transfer regime (i.e. $q < 5/6$; Paczyński, 1971).

1.3 Formation scenarios

It is generally accepted that LMXBs are descendants of compact binaries composed of a primary star of $\gtrsim 10 M_\odot$ and a secondary of $\lesssim 1 M_\odot$. This extreme mass ratio sets the evolution of the system. The massive star evolves faster than the secondary, expanding until it overflows its Roche lobe, thus starting an unstable mass transfer phase. The mass is transferred too fast to be accreted by the secondary, so the gas accumulates in an external envelope enclosing the system. This is known as the common-envelope phase (Paczyński, 1976). The binary orbiting inside this envelope transfers angular momentum to the common envelope that is heated and spun up. At the end of this stage, the common envelope is expelled, carrying away angular momentum from the system, while the binary orbit has shrunk substantially. This phase does not affect the core of the massive star, which continues its evolution until its final stage, collapsing

into a BH or a NS. This results in a detached system comprising the collapsed core and a main sequence low-mass secondary in orbits with typical periods of ~ 0.5–10 days (King et al., 1996).

At this point, King et al. (1996) distinguishes three evolutionary paths that bring the companion into Roche-lobe contact, and hence the system to a stable mass transfer phase. The path to be followed will depend on the timescales of the expansion of the secondary (which eventually leaves the main sequence, $t_{\rm MS}$) and the shrinkage of the orbit due to angular momentum loss ($t_{\rm AML}$):

1. $t_{\rm MS} \ll t_{\rm AML}$. The secondary star evolves off the main sequence and fills its Roche lobe. The mass is redistributed and, in order to conserve the total angular momentum, the system migrates to longer periods. This results in systems with an evolved companion with orbital periods of $\sim$ 2–100 days.

2. $t_{\rm AML} \ll t_{\rm MS}$. The system loses angular momentum because of some mechanism (e.g. magnetic braking or gravitational wave emission). That causes the Roche lobe to shrink over the companion, starting the mass transfer when it is still on the main-sequence. The systems derived from this situation have short orbital periods (of the order of hours) with a main sequence companion.

3. $t_{\rm MS} \sim t_{\rm AML}$. The mass transfer is started by overflow of the evolved companion, but angular momentum loss shrinks the Roche lobe below the star's equilibrium radius causing the nuclear evolution of the secondary to cease. This ends in a short-period binary but with an evolved secondary.

This evolutionary scheme succeeds in explaining most of the observed population of LMXBs. Smith & Dhillon (1998) studied the relation between the orbital period and the spectral type of the secondaries in LMXBs. They found that systems with short orbital periods ($\sim$7 h) contain main sequence or somewhat evolved companions, while those with longer periods were observed to harbour evolved stars.

However, it is thought that some LMXBs may in fact be descendants of IMXB systems. This alternative scenario was independently proposed by King & Ritter (1999) and Podsiadlowski & Rappaport (2000), who demonstrated that an IMXB precursor with a secondary of $\sim 3.5 M_{\odot}$ can successfully explain the observed properties in the NS-LMXB Cyg X-2. Within this evolutionary picture, the IMXB progenitor undergoes unstable mass transfer ($q > 5/6$) until mass redistribution reverses the mass ratio and the mass transfer becomes stable. During the process, the companion loses a significant fraction of its mass, resulting in an evolved low-mass companion star with a non-degenerate He core and H-burning in a shell. Nonetheless, attempts to explain the entire population of LMXBs as IMXB descendants fail because the donor stars in LMXBs are seen to be cooler than predicted by model simulations (see Justham et al., 2006).

1.4 The accretion disc

The angular momentum carried by the gas leaving the donor forces it into orbit forming a ring around the compact object. Within the ring, the angular momentum is transported outward by the action of viscosity, and the gas is distributed in a thin disc. During the process, the gas spirals towards the compact object as it loses gravitational energy. A fraction of this energy

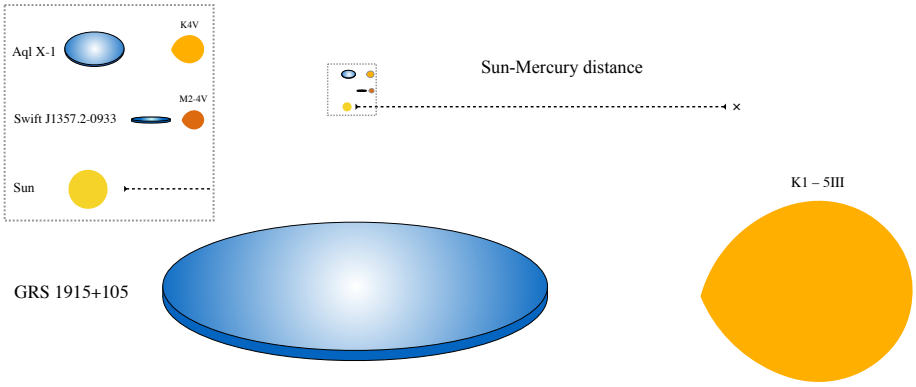

FIGURE 1.2— Scaled model of three LMXBs. The Sun-Mercury distance and the Sun size are also represented to scale for comparison. Swift J1357.2–0933 and Aquila X-1 are the systems studied in this thesis with a well-determined orbital period (shown in the zoomed area; dashed-line box) and GRS 1915+105 is by far the longest period LMXB ($\sim$ 34 d; Steeghs et al., 2013). The orbital inclination (i, the angle subtended by the orbital axis with respect to the observer line of sight) is also represented and the spectral type of the companion star is indicated for each case. Typical angular sizes of LMXBs are of the order of μarcsec. For instance, considering a distance of $\sim$ 9 kpc (Reid et al., 2014), GRS 1915+105 subtends $\sim$ 50 μarcsec.

is eventually released in the form of electromagnetic radiation. This mechanism is especially efficient in LMXBs, as approximately 10% of the rest mass energy (mc^2) can be released in the process (Pringle, 1981).

1.4.1 The standard accretion disc model

The model proposed by Shakura & Sunyaev (1973) is considered the standard solution for the structure of an accretion disc. It presents one of the most simple solutions to the equations of conservation of mass, angular momentum, and energy, and provides the starting point for more complex and specific models. The accretion disc is assumed to be axially symmetric and stationary; that is, with a constant mass transfer rate ($\dot{M}$) at any radius. The disc is also assumed to be in local thermal equilibrium, which means that the gas can efficiently radiate the viscous heat locally. Consequently, the accretion disc comprises a relative cool gas distributed in a geometrically thin disc (i.e. $H \ll R$, where R is the disc radius and H the scale height).

For accretion to take place, there must be some mechanism whereby the gas loses its angular momentum. The ordinary microscopic viscosity is not enough to account for this loss, so Shakura & Sunyaev (1973) proposed turbulence viscosity as the source of momentum dissipation (see also Pringle, 1981). However, the precise form of this viscosity is not well understood. In order to address this problem, in the Shakura-Sunyaev model the viscosity is expressed as a function of a dimensionless parameter (α) in the form $\nu = \alpha c_s r$ (where c_s is the sound speed in the disc, r is the radial coordinate, and the turbulent motion is supposed to be subsonic, i.e. $\alpha \lesssim 1$).

There is no detailed model for α that tells us about the precise viscosity mechanism. The

dissipation process is still the main source of uncertainty in the accretion disc theory. Nevertheless, Balbus & Hawley (1991) proposed that the magneto-rotational instability caused by an axial magnetic field could provide efficient angular momentum transport in the gas to explain the accretion of material onto the compact object.

The solutions obtained from the Shakura-Sunyaev disc depend weakly on α and many observables can be explained by the model. The derived effective temperature goes as $T_{\rm eff}(r) \propto r^{-3/4}$. The local thermal equilibrium condition in an optically thick disc implies that every annulus radiates as a blackbody at $T_{\rm eff}(r)$. Hence, accretion disc emission would be the superposition of multi-temperature blackbody spectra distributed according to the predicted temperature profile. The X-ray emission is thus produced in the inner region, where temperatures can reach $\sim 10^7$ K. This is in good agreement with the observed LMXB X-ray spectra to a first-order approximation (e.g. Mitsuda et al., 1984). Nevertheless, it is necessary to consider more realistic and complex models in order to achieve a higher degree of accuracy in the spectral modelling (see Sec. 1.5.1).

By assuming a Keplerian isothermal disc, a flared and concave geometry is derived. The accretion disc radial profile goes as $h(r) \propto r^{9/8}$, where $h(r)$ is the disc height at a given radius. This radial flaring is particularly important in X-ray binaries since a fraction of the X-ray radiation produced in the inner regions will be re-absorbed by the outer (and vertically higher) part of the disc. This process affects the temperature profile of the disc and hence its geometry.

Vrtilek et al. (1990) studied the irradiated disc structure by considering an extra heating input due to X-ray irradiation in a Shakura-Sunyaev disc. They found that such irradiation produces a flatter temperature profile $T_{\rm eff}(r) \propto r^{-3/7}$, while causing a thickening of the disc according to $h(r) \propto r^{9/7}$. In this regard, in Ch. 3 we present the first empirical measurement of the vertical structure of an accretion disc in an LMXB, and this is consistent with the irradiated disc scenario.

1.4.2 The Eddington luminosity

There is a maximum luminosity that an accreting object in hydrostatic equilibrium can radiate. Above this luminosity, the outward radiation pressure would exceed the inward gravitational attraction and, as a consequence, accretion would cease. This is known as the Eddington luminosity ($L_{\rm Edd}$) and is determined by the mass of the accretor:

$$L_{\rm Edd} \simeq 1.3 \times 10^{38} \frac{M_1}{M_\odot} \quad {\rm erg\,s^{-1}} \tag{1.4}$$

This expression assumes a steady and spherically symmetric accretion flow composed of fully ionised hydrogen, and can be generally applicable as an order-of-magnitude estimate. Thus, for typical NS and BH masses (1.4 $M_\odot$ and 10 $M_\odot$, respectively) the maximum luminosities allowed by Eq. 1.4 are $L_{\rm Edd}({\rm NS}) \sim 10^{38}$ erg s^{-1} and $L_{\rm Edd}({\rm BH}) \sim 10^{39}$ erg s^{-1}.

1.4.3 The disc instability model: persistent and transient systems

According to their long-term brightness variability, LMXBs can be classified as persistent or transient systems. Persistent sources are always in a luminous ($L_{\rm X} \sim 10^{38} - 10^{39}$ erg s^{-1}) and nearly stable state. Transient systems are usually in a faint ($L_{\rm X} \sim 10^{30} - 10^{33}$ erg s^{-1}), quiescent state, only interrupted by sporadic outbursts when they increase their luminosity by several orders of magnitude (typically $\gtrsim 0.1\ L_{\rm Edd}$). Since the emission from the disc is ultimately

regulated by the accretion rate, a variable luminosity implies a variable $\dot{M}$ and thus the steady disc condition is no longer fulfilled.

The behaviour of transient LMXBs can be described by the so-called disc instability model (DIM, Osaki, 1974). Van Paradijs & Verbunt (1984) showed that, when self-irradiation effects are taken into account (i.e. heating of the outer parts of the disc by the X-ray emission coming from the inner regions), the transient-persistent dichotomy in X-ray binaries could be associated with a thermal-viscous instability in the accretion disc.

The DIM is based on the partial ionisation of hydrogen in the accretion disc. The radial temperature profile leads to the coexistence of two regions determined by the radius at which the disc temperature is that of hydrogen ionisation, $T(r_{\rm ion}) \sim 10^4$ K. In the inner regions ($r < r_{\rm ion}$) hydrogen is ionised and exists in a hot (viscous) state, while in the outer regions ($r > r_{\rm ion}$) hydrogen starts to recombine and free electrons become less mobile. Both the bound-free and free-free cross-sections increase so does the opacity of the gas. The viscosity is lower in the neutral hydrogen region, and the angular momentum loss is less efficient than in the ionised region, causing mass to accumulate in the external disc. The outer regions become progressively denser and more opaque, so the temperature increases until an instability occurs. The thermal-viscous instability results in an ionisation front that propagates throughout the neutral region, triggering the X-ray brightening observed in transient system during outbursts (see Lasota 2001 for an extended review).

Since the temperature profile depends on $\dot{M}$ (and thus on the mass source $\dot{M}_2$), the DIM predicts the existence of a critical mass transfer rate ($\dot{M}_{\rm crit}$) that will determine whether a system is transient or persistent. King et al. (1996) studied the DIM model, taking into account the X-ray self-irradiation effects in the accretion disc to obtain:

$$\dot{M}_{\rm crit} \simeq 5 \times 10^{-11} M_1^{2/3} P_3^{4/3} \tag{1.5}$$

where $\dot{M}_{\rm crit}$ is given in $M_\odot$ yr^{-1} and P_3 is the orbital period in 3-hour units. A given system showing $\dot{M}_2 > \dot{M}_{\rm crit}$ will be persistent, while transient systems have $\dot{M}_2 < \dot{M}_{\rm crit}$.

For NS-LMXBs ($M_1 \sim 1.4 M_\odot$) Eq. 1.5 yields $\dot{M}_{\rm crit} \sim 10^{-10} M_\odot$ yr^{-1}, while for BH-LMXBs ($M_1 \sim 10 M_\odot$) corresponds to a larger $\dot{M}_{\rm crit} \sim 10^{-9} M_\odot$ yr^{-1}. This indeed agrees with what is observed: most BH systems are transients, whereas NS totally dominate the population of persistent systems (Coriat et al., 2012).

It is noteworthy that $\dot{M}_{\rm crit}$ also depends on the size of the accretion disc. This is expected since larger accretion discs (longer orbital periods) will need higher accretion rates to keep all the disc in a hot, ionised state; therefore, systems with long orbital periods are more likely to be observed as transient systems.

1.5 Observational properties

1.5.1 The spectral energy distribution

Even though the bulk of the emission in LMXBs is radiated in the X-ray regime, deeper insights into the various emission mechanisms involved, the region where they are produced, and how their contribution to the continuum evolves through different states of the system, come from studies across the entire electromagnetic spectrum (e.g. Chaty et al., 2003b; Gallo et al., 2007). However, these objects are extremely variable on many timescales and are intrinsically faint in

other spectral ranges (e.g. in outburst, typically fainter than 15 mag in the optical). This makes multi-wavelength analysis an arduous and frequently unfeasible task, given the limited and competitive observing time available. Nonetheless, some progress has been made in understanding the spectral energy distribution (SED) of LMXBs, either by exhaustive multi-wavelength observations of the same object (e.g. the BH-LMXBs GRS 1915+105; Fuchs et al., 2003; Rahoui et al., 2010), or by the cumulative study of different sources.

The SED varies from one object to another and depends on many factors, such as the nature of the compact object or the accretion state (luminosity) when it is observed. It is thought that five main components contribute to LMXB spectra, which arise from different regions of the binary system (see Fig. 1.3) and involve a wide variety of physical mechanisms:

Accretion disc. Accretion disc emission consists of a thermal component that can be well modelled with a multicolour blackbody with temperatures ranging $10^3 - 10^7$ K. Since most of the accretion energy is released in the inner (and hotter) tenth part of the disc (Frank et al., 1992), the thermal component peaks in the range of 0.7–1.5 keV. The so-called soft X-ray regime (i.e. energies below ~ 10 keV) is dominated by the inner accretion disc component, while the outer parts emit dimly at longer wavelengths, from the ultraviolet to the infrared (IR). Several recombination lines are observed superposed on the continuum. These emission lines are broad (FWHM $\sim$ 500–2000 km s^{-1}) and typically show a double-peak profile indicative of a Keplerian accretion disc geometry (see Sec. 1.6).

Boundary layer. Once the accreted gas reaches the innermost stable circular orbit (ISCO), nearly half of the gravitational energy carried by the gas has yet to be released. If the accretor is a BH, the matter leaving the ISCO can no longer follow a circular orbit and falls through the event horizon, advecting the gravitational energy contained in it. If the compact object is a NS, matter accumulates between the ISCO and the surface of the NS in a region that is known as the boundary layer. Since the NS typically rotates several times more slowly than the Keplerian frequency near its surface, the matter is decelerated down as the NS is spun-up . Therefore, before matter reaches the NS surface, a huge amount of kinetic energy is converted into other forms in the boundary layer (Syunyaev & Shakura, 1986). As a consequence, NS systems will display an extra spectral component emitted in this region. This component was observed to be thermal and as luminous as that of the accretion disc, but typically harder (peaking in the range 5–10 keV; e.g. Gilfanov & Revnivtsev, 2005; Armas Padilla et al., 2017).

In NSs with strong magnetic fields this picture is no longer applicable since the magnetic torques in the surroundings of the NS can disrupt the disc, dramatically modifying the inner structure of the accretion flow (see Sec 1.5.3).

Companion star. The emission of a late-type companion star (with effective temperature in the range $T_{\rm eff} \sim 4000 - 7000$ K) peaks in the optical to near-infrared (NIR) regime. Typically, this contribution is completely veiled by the emission from the accretion structures in either persistent or transient systems in outburst. However, in most transients the quiescent spectrum is dominated by the companion in the optical-NIR and their spectroscopic features can be distinguished. This provides an opportunity to investigate the nature of the donor star and the dynamical properties of the binary (see Sec. 1.7).

Relativistic jet. From radio to mid-IR wavelengths there is no significant radiation from either the accretion disc or the companion star. During the hard state (a phase associated with the initial rise to outburst and characterised by a hard X-ray spectrum peaking around 100 keV ; see Sec. 1.5.2) this spectral range is dominated by synchrotron emission produced by high-energy (relativistic) electrons spiralling in a magnetic field within a collimated jet. This component is predominantly observed in BH-LMXBs at relatively low accretion rates. It is emitted through both optically thick and thin regimes (Blandford & Königl, 1979; Falcke & Biermann, 1995). In the optically thick case, the flux density is well described by a flat or weakly-inverted power law ($F_\nu \propto \nu^\alpha$, with $-0.1 < \alpha < 0.7$) that extends from the radio to the mid-IR (e.g. Corbel & Fender, 2002; Hynes et al., 2003; Migliari et al., 2006). Beyond that, α decreases to $-1.0 < \alpha < -0.4$ in the optically thin regime (Russell et al., 2013). It is thought that the optically thick spectrum arises from a conical self-absorbed compact jet, while the optically thin spectrum reflects the non-self-absorbed base of the jet.

Corona. A hard ($\gtrsim$ 10 keV) X-ray tail is concurrently observed with the jet emission (e.g. Gallo et al., 2004). This emission may arise from a region above the inner disc, where a *corona* of high-energy electrons (hot, optically thin plasma) scatters, by means of the inverse Compton effect, the soft photons coming from the disc and/or the NS surface (Begelman et al., 1983). This results in a nearly flat high-energy continuum that can be roughly modelled by a power law, which also shows several spectral features arising from reprocessing and reflection of a fraction of the corona emission in the accretion disc (Fabian et al., 1989).

The geometry and properties of the corona are still under debate. Some authors suggest that it is actually the base of the jet. The jet and the corona emission has shown correlated variability in many cases (e.g. Gandhi et al., 2017, and references therein) and both are inferred to arise in the vicinity of the inner accretion disc, so that it is reasonable to assume that a component of the high-energy (non-thermal) electrons that produce the comptonisation is also responsible for the synchrotron emission in the jet (e.g. Fender, 2001; Gallo et al., 2003).

1.5.2 Accretion states

The study of the evolution of transient BH-LMXBs during outburst led to the identification of different accretion states, that were empirically established based on their spectral and timing properties (Miyamoto et al., 1992, 1993; McClintock & Remillard, 2006; Belloni et al., 2011). These states were also observed to be associated with a distinctive phenomenology, such as collimated radio jets and accretion disc winds (see e.g. Ponti et al., 2012; Fender & Belloni, 2012; Fender & Muñoz-Darias, 2016).

For a given source, the accretion state can be identified by its position in a hardness-intensity diagram (HID; Homan et al., 2001; Belloni et al., 2005). The HID represents the time evolution of the X-ray intensity as a function of the hardness ratio, defined as the ratio of the X-ray luminosity in a *hard* band ($\sim 5 - 50$ keV) to that in a *soft* band ($\sim 0.1 - 5$ keV).

Along their evolution through the outburst, BH transients that cover all the states follow a hysteresis pattern within the HID (Miyamoto et al., 1995). During this cycle they show three

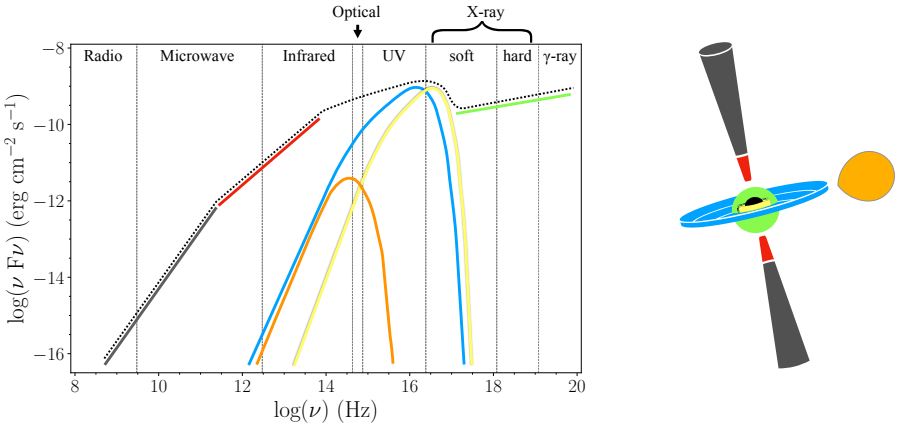

FIGURE 1.3— Left: schematic spectral energy distribution of an LMXB. The five main components described in the text (Sec. 1.5.1) are represented. The sum of all the components is displayed with a black dotted line. Right: cartoon of an LMXB. The colour indicates the emission region that corresponds to each spectral component in the schematic SED following the same colour code. Blue indicates the disc blackbody component, red and grey the jet emission (optically thick and thin, respectively), orange corresponds to the companion star, green to the corona, and yellow to the boundary layer.

main accretion states. A hard state is observed during the initial rise of the outburst until, at some point (typically above $0.1L_{\rm Edd}$), the X-ray spectrum becomes gradually softer. This is the intermediate state, a fast (i.e. days) transitional phase occurring at roughly constant luminosity. After that, the system enters into the soft state, where the luminosity slowly (weeks to months) decays. Henceforth, a reverse transition to the hard state, also at nearly constant flux, is observed. Each of the states presents distinctive observational properties:

Hard state. It is characterised by a hard X-ray component (coming mainly from the corona) that peaks around 100 keV and dominates the X-ray spectrum. During this state strong synchrotron emission associated with a powerful and quasi-steady jet is observed. The hard state is also associated with a high level of rapid X-ray variability.

Intermediate state. During this phase the thermal component produced in the accretion disc rises and the X-ray spectrum softens. This state is characterised by the discrete ejection of plasma that is bright at radio wavelengths. In several cases, the blobs of plasma are spatially resolved moving away at relativistic speeds from the central source (e.g. GRS 1915+105; Mirabel & Rodríguez, 1994; Fender et al., 1999).

Soft state. This is the most radiatively efficient phase of the outburst, and is characterised by a low level of fast X-ray variability. The disc thermal component (peaking at ~ 1 keV) completely dominates the X-ray spectrum in this state. The jet emission is no longer observed. Instead, highly-ionised (hot) accretion disc winds are detected as absorption

lines in the X-ray spectra (typically Fe XXV and Fe XXVI), and are only observed in sources seen at high inclination (Ponti et al., 2012). The later implies an equatorial geometry for the wind.

Accretion disc winds are thought to be characteristic of the soft state. However, low-ionisation (cold) winds were detected in the BH-LMXB V404 Cygni at optical wavelengths during the hard state (Muñoz-Darias et al., 2016). Optical winds have also been observed during this phase in V4641 Sgr (Chaty et al., 2003a; Muñoz-Darias et al., 2018) and MAXI J1820+070 (Muñoz-Darias et al., 2019). These findings triggered the interpretation that winds could be present in most of the accretion states (see Sec. 1.8).

In addition to using purely spectral properties, Muñoz-Darias et al. (2011) showed that the X-ray rapid variability can be used as a tracer of the accretion state in BH systems and demonstrated that hysteresis is also observed in the X-ray variability-intensity diagram during outburst (see also Heil et al., 2012). NS systems, on the other hand, show a more complex behaviour in the HID, probably as a consequence of the extra component coming from the boundary layer (e.g. Lin et al., 2007). However, by studying a large sample of these systems, Muñoz-Darias et al. (2014) showed that those accreting below 30 % of $L_{\rm Edd}$ follow a hysteresis cycle in an X-ray variability-intensity diagram similar to that observed in BHs. This sets a common framework for both populations, where accretion states can be determined by their location in such diagrams (see Fig. 1.4).

1.5.3 Compact object identification

Dynamical mass measurements are the most robust method for determining the nature of a compact object (i.e. a NS or BH accretor; see Sec. 1.7). However, a dynamical approach is only applicable to a handful of sources (19 BHs dynamically confirmed, Casares & Jonker, 2014; Corral-Santana et al., 2016). When the mass measurement is not feasible, the possible nature of the compact object can be elucidated based on other observables:

Coherent X-ray pulsations. Some NSs possess strong enough magnetic fields (for a given accretion rate) to truncate the disc and funnel the accretion flow onto their magnetic poles. This produces one or two X-ray spots where the gas meets the NS surface. The spots rotate when the magnetic axis is tilted with respect to the spin axis of the NS and thus the focusing effects produce periodic X-ray flux pulsations with recurrence of fractions of a second to minutes. These are the so-called accretion-powered pulsars.

The orbital motion of the NS around the centre of mass of the binary system produces a modulation in the arrival time of the observed pulse. This modulation traces the orbit of the NS. Hence, by measuring the evolution of the X-ray pulsations throughout an orbital period, the K_1 velocity (i.e. the radial velocity semi-amplitude of the compact star) can be accurately determined (precisions of up to $\sim$1 km s^{-1}; e.g. Jonker & van der Klis, 2001).

Thermonuclear X-ray bursts. During outburst, some systems show bright X-ray flares lasting 10–100 s that can be recurrent on timescales of hours. These are thermonuclear bursts produced by runaway fusion of material accumulated on the surface of the compact object (Narayan & Heyl, 2002). X-ray bursting behaviour is interpreted as distinctive of

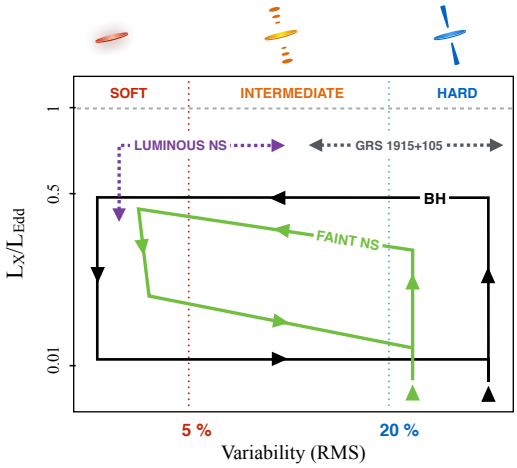

FIGURE 1.4— Qualitative sketch of the hysteresis cycle in the X-ray variability-intensity diagram. Variability is shown as the fractional root mean square (RMS) amplitude, while the luminosity is scaled to the Eddington luminosity. The cycle is a clockwise loop starting at high variability and low luminosity. The black loop indicates the evolution of BHs and the green one that of faint ($\lesssim 0.3 L_{\rm Edd}$) NSs. The position in the diagram of luminous, persistent NSs is shown in purple, while the only persistent BH known (GRS 1915+105) is indicated in grey. Above the panel are shown the accretion states and (schematically) the corresponding outflow properties: accretion disc winds, discrete ejections and steady jet (red, orange, and blue, respectively). Adapted from Muñoz-Darias et al. (2014).

NS systems since, in the absence of a solid surface, the matter cannot be stored in the BH's event horizon.

The NS nature of X-ray pulsars and burster systems is consistent with their dynamically derived masses, which are found to be smaller than $\sim 2M_{\odot}$ (Thorsett & Chakrabarty, 1999; Charles & Coe, 2006).

X-ray spectral fitting. In order to account for the emission from the boundary layer (see Sec. 1.5.1), the X-ray spectral modelling of NS systems usually requires an extra component (e.g. Lin et al., 2007).

The optical/X-ray luminosity diagram. Russell et al. (2006) found an empirical correlation between the nature of the compact object and its optical-NIR to X-ray luminosity ratio based on observations of a large number of LMXBs. This approach relies strongly on the distance to the source, but produces a qualitative classification when the latter is properly determined (see Ch. 2).

1.6 The optical spectrum

There are two main sources contributing to the optical spectrum of an LMXB: the donor star and the accretion disc. The optical emission from the disc is produced in its outer radii. There, a sizeable fraction of the X-ray photons (coming from the innermost regions) are absorbed and subsequently re-emitted at lower energies. The emission coming from the late-type companion typically peaks at optical wavelengths but it is relatively faint in comparison to that of an active disc (i.e. outburst or persistent source). The optical light is then generally dominated by the accretion disc contribution (see van Paradijs & McClintock, 1995, for a review). Consequently, LMXBs typically show a blue spectrum, given the thermal continuum of the disc (see Fig. 1.3). Only in quiescent LMXBs and long-period, persistent LMXBs (e.g. Cyg X-2) the companion dominates over the accretion disc emission.

Superposed on the continuum, the optical spectrum shows broad emission lines (FWHM $\sim$ 500–2000 km s^{-1}) mostly from neutral H and He transitions. These features are mainly produced in the outer accretion disc, where the temperatures are low enough for these elements to recombine ($\sim 10^3$ K). In most sources, the emission lines show a double-peaked profile, a signature of gas orbiting in a Keplerian accretion disc geometry (Smak, 1969).

The peak-to-peak separation and broadening of the emission lines are driven by the projected velocity distribution (see Fig. 1.5). Thus, both the shape (i.e. single- or double-peaked) and the width of the lines depend on the inclination of the accretion disc (Horne & Marsh, 1986). Narrow emission lines will be observed in face-on systems (i.e. $i \sim 0$), while the largest double-peak separations and broadest lines will be characteristic of edge-on sources (Torres et al., 2004; Corral-Santana et al., 2013, XTE J1118+480 and Swift J1357.2–0933, respectively).

The observed spectral properties are different in transient systems between quiescence and outburst, while the spectra of persistent systems resemble that of transients in outburst.

1.6.1 Outburst

At high accretion rates, the disc is bigger and hotter than in quiescence (Krzemiński, 1965; Paczyński, 1965; Smak, 1971, 1984). Thus, the accretion disc completely dominates the optical

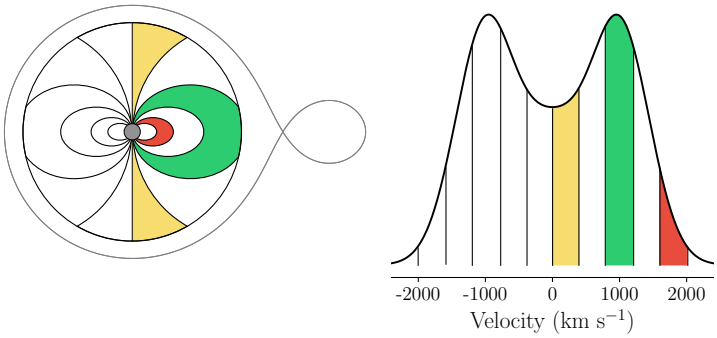

FIGURE 1.5— Diagram of the constant projected velocity regions in a Keplerian accretion disc (left) and its corresponding contribution to the emission line profile (right, adapted from Horne & Marsh, 1986).

spectrum and the companion star emission is outshone even at NIR wavelengths. Regions with lower temperatures move towards the edge of the heated disc. For this reason, the recombination of hydrogen and helium occurs at larger radii, i.e. at lower Keplerian velocities. Thus, smaller velocities contribute to the profile during outburst and the emission lines get narrower. In this phase, the X-ray irradiation of the system becomes significant and, as a consequence, higher ionisation features, such as the Bowen blend, are observed in the optical spectrum (see Fig. 1.8, top panel).

The Bowen blend

As a result of the strong irradiation, a large population of He II-Lyα photons are produced through X-ray reprocessing in different regions of the binary. Subsequently, these photons trigger a fluorescence resonance through cascade recombination of O III, which in turn produces N III lines (see Fig. 1.7; McClintock et al., 1975). The latter are the strongest components of the so-called Bowen blend. This blend of high-excitation lines is likewise composed by O II and C III transitions that are also produced because of the effect of the strong irradiation (see Table 1.1). The Bowen blend is observed at optical wavelengths in the region from 4630 to 4660 Å.

Based on high resolution spectroscopy of Sco X-1, Steeghs & Casares (2002) observed many emission lines at the core of the broad Bowen blend. These components were very narrow (FWHM ~ 50 km s^{-1}), which is a clear indication of being produced in a compact region with a small velocity dispersion. In addition, they found these lines to move in antiphase with respect to the compact star. This is in agreement with an origin on the irradiated face of the companion star. Several objects have revealed that narrow components within the Bowen blend arise from the irradiated side of the companion star, opening up a new avenue for the determination of K_2 in systems in the companion star is veiled by the brightness of the accretion structures (see Sec.1.7.5).

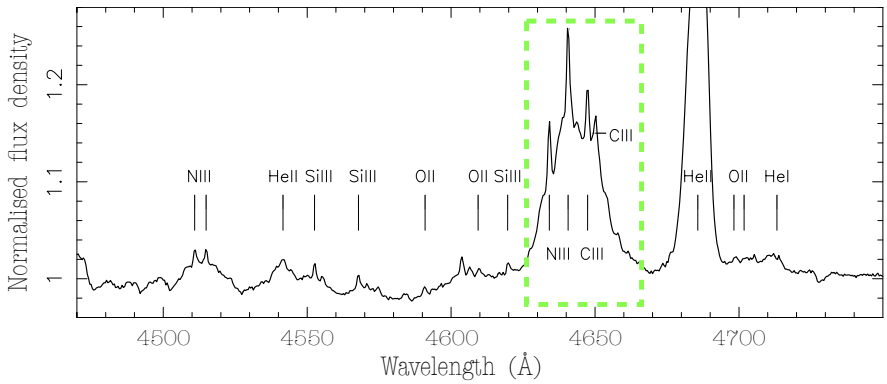

FIGURE 1.6— Average normalised spectrum of the persistent LMXB Sco X-1 in the region around the Bowen complex (indicated by a green dashed line box). The transitions identified are indicated, with the strong He II emission at 4686 Å going off-scale (adapted from Steeghs & Casares, 2002).

λ (Å)	Laboratory intensity	J
C III ($3s\ 3^S - 3p\ ^3P^0$)		
4647.42	14	1-2
4650.25	13	1-1
4651.47	11	1-0
N III ($3p\ ^2P^0 - 3d\ ^2D$)		
4634.14	8	1/2-3/2
4640.64	10	3/2-5/2
4641.84	7	3/2-3/2
O II ($3s\ ^4P - 3p\ ^4D^0$)		
4638.86	6	1/2-3/2
4641.81	9	3/2-5/2
4649.13	10	5/2-7/2
4650.84	6	1/2-1/2
4661.63	9	3/2-3/2
4673.73	4	3/2-1/2
4676.24	8	5/2-5/2
4696.35	2	5/2-3/2

TABLE 1.1— The strongest optical emission lines of C III, N III, and O II contributing to the Bowen blend. Adapted from McClintock et al. (1975).

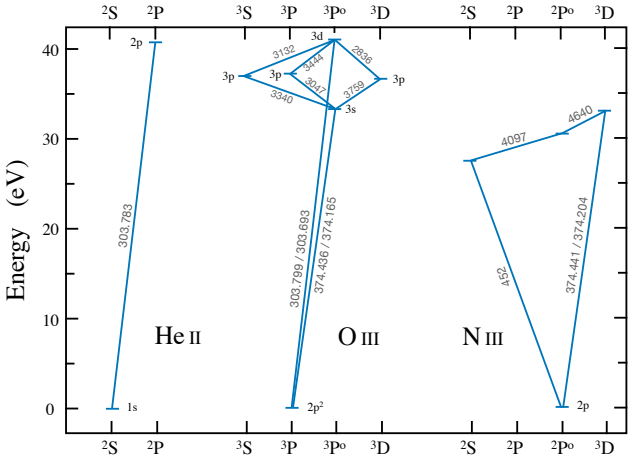

FIGURE 1.7— Grotrian diagrams of He II, O III, and N III. Only the transitions playing an important role in the Bowen fluorescence process are included. Wavelengths are given in Å and only the optical lines of O III, and N III that contribute significantly are given for each multiplet. Adapted from McClintock et al. (1975).

1.6.2 Quiescence

During quiescence, transient systems are typically a factor ≥ 100 fainter than in outburst. This attenuation is mostly due to a dimmer accretion disc (see Sec. 1.4.3). The optical spectrum reddens in comparison to outburst and, in most systems, the companion star is detectable in the optical/NIR spectrum. In these cases, the absorption lines produced in the photosphere of the secondary can be observed and the dynamical information, such as the radial velocity semi-amplitude of the companion star or the inclination of the system becomes accessible through spectroscopy of the companion or by analysing the ellipsoidal modulation of the light curve, respectively (see Sec. 1.7 and Fig. 1.8, bottom panel).

Nevertheless, even in quiescence the accretion disc's contribution cannot be neglected. In some cases, particularly in short-period binaries, the lobe-filling companion star is very faint and the accretion disc dominates, hampering the detection of absorption features and/or introducing stochastic variability (flickering) in the optical emission (e.g. Zurita et al., 2003). These effects can be mitigated by observing at NIR wavelengths, where the accretion disc is expected to be fainter (e.g. Gelino et al., 2001).

1.7 System parameters

1.7.1 Orbital period and inclination

The most important binary parameter is arguably $P_{\rm orb}$. Since the Roche lobe size depends on it (Paczyński, 1971), measuring $P_{\rm orb}$ allows us to learn about the scales of the system. A knowledge

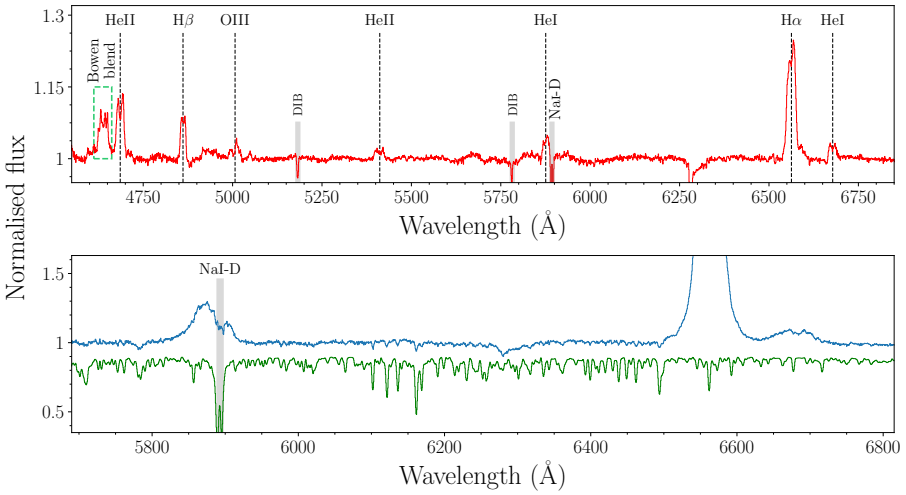

FIGURE 1.8— Optical spectrum of the BH transient MAXI 1820+070. Top panel: normalised outburst spectrum. The Bowen blend region is indicated by a dashed line box. Bottom panel: quiescence normalised spectrum (blue) compared with a K4V template spectrum (from Torres et al., 2019).

of $P_{\rm orb}$ can also shed some light on the properties of the companion star by estimating the mean density of a Roche-lobe-filling star ($\bar{\rho}$). That density value can be obtained from $P_{\rm orb}$ (Faulkner et al., 1972) as:

$$P_{\rm orb} = 3.83 \times 10^4 \sqrt{\bar{\rho}}$$

where $\bar{\rho}$ is given in g cm^{-3}, and $P_{\rm orb}$ in s. Comparing this value with tabulated values of stars (e.g. Cox, 2000), and assuming an evolutionary state of the companion, its spectral type can be inferred (see Ch. 2).

There are various approaches to measure $P_{\rm orb}$ based on different observables. In high-inclination systems the companion star crosses the line of sight to the compact star. Thus, in systems with $i \gtrsim 75°$, the transit of the donor occults (partially or totally) the accretion disc, producing X-ray eclipses. Likewise, in lower inclination systems ($60° \lesssim i \lesssim 75°$), the X-ray light curve shows dips that are interpreted as occultations of the central X-ray source by low ionised disc material (White & Mason, 1985). These effects occur once per orbital cycle, causing a modulation in the light curve from which $P_{\rm orb}$ can be determined (see Fig. 1.9). Curiously, Corral-Santana et al. (2013) found optical dips in the BH transient Swift J1357.2–0933 during outburst that are not modulated with $P_{\rm orb}$. In this thesis we present a spectroscopic study of this source proving that the optical dips are produced by a disc outflow that has an equatorial geometry (see Ch. 4).

In lower inclination systems $P_{\rm orb}$, i, and q can be measured from the modulation introduced in the light curve by the star filling its Roche lobe. As we showed in Sec. 1.2, the donor star loses its sphericity and the cross-sectional area seen by an observer will depend on the orbital

phase. As a result, the optical-NIR light curve shows a double-humped shape known as the ellipsoidal modulation (see Fig. 1.10). Because of the effect of gravity darkening (von Zeipel, 1924), the surface temperature of the companion star is maximum at the poles and minimum at L_1. Since less flux is emitted from regions having a lower effective temperature the symmetry between minima is broken, and thus the minima is deeper when L_1 is facing the observer (i.e. orbital phase 0.5). At high X-ray luminosity (e.g. near outburst) the X-ray irradiation heats the inner face of the companion star offsetting the gravity darkening effect and reversing the depths of the minima. The amplitude of this modulation is mainly determined by i, with a weaker dependence on q that becomes significant for $q \gtrsim 0.1$ (see e.g. Orosz et al., 1997; Shahbaz et al., 2003, for full details of the light curve modelling). Thus, $P_{\rm orb}$ can be determined by measuring the time between two adjacent minima, but also i and q can be obtained by modelling the light curve.

Note that this method can be applied only if the companion star dominates ($\gtrsim 50\%$ of the observed flux) the optical-NIR light; that is, in transient systems in quiescence. But even so, the accretion disc emission produces a superposed stochastic variability (flickering) that can sometimes contaminates the ellipsoidal modulation (e.g. Zurita et al., 2003). In these cases, Pavlenko et al. (1996) showed that the ellipsoidal modulation could still be discerned underlying the flickering in the light curve by modelling its lower envelope. In addition, other mechanisms for periodic variability observed at optical wavelengths can sometimes be exploited e.g. variation of the visibility of the hot spot (where the gas stream coming from the donor impacts the disc) or superhump modulation triggered by precessing accretion discs during outbursts (see e.g. table 5.3 in Charles & Coe, 2006).

Alternatively, an indirect method of estimating $P_{\rm orb}$ was developed by Shahbaz & Kuulkers (1998), who observed a correlation between $P_{\rm orb}$ and the V-band photometric amplitude from quiescence to outburst. This can be used as an estimator of $P_{\rm orb}$ in those transient systems that do not show a periodic orbital modulation.

1.7.2 Mass ratio

It is assumed that the companion star orbits in synchronous rotation (i.e. equal orbital and stellar angular velocity) since LMXBs have lived long enough ($\gtrsim 10^8 - 10^9$ yr) for such a short period systems ($\sim$ h) to become tidally locked. In that case, the projected linear velocities are related by:

$$\frac{V_{\rm rot} \sin i}{R_2} = \frac{K_2 + K_1}{a} = \frac{K_2 \, (1+q)}{a}$$

where $V_{\rm rot} \sin i$ is the rotational broadening of the donor star, while K_1 and K_2 are the radial velocity semi-amplitudes[1] of the compact object and the donor star, respectively. Using this in combination with Eq. 1.2, Wade & Horne (1988) obtained:

$$V_{\rm rot} \sin i = 0.46 K_2 q^{1/3} \, (1+q)^{2/3}$$

This expression establishes an empirical method to determine the mass ratio by measuring K_2 and the rotational broadening of the absorption lines from the companion star.

[1] Maximum orbital velocity projected along the line of sight.

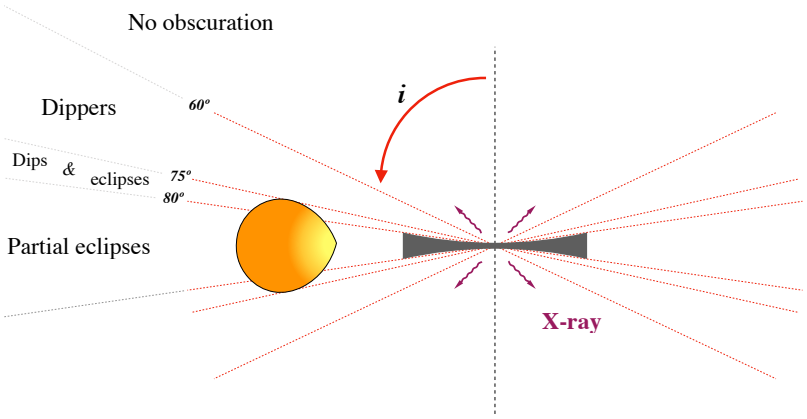

FIGURE 1.9— Schematic representation of the different dipping phenomenology observed depending on the orbital inclination (adapted from Frank et al., 1987).

1.7.3 Mass function

The mass of the compact object is a fundamental parameter of the binary. The nature of the accretor can be unambiguously determined in most cases if M_1 is known. To know the mass distribution of these stellar remnants it is also a key piece that sets observational constrains in the collapse of massive stars theories, the equation of state of the nuclear matter, or the accretion processes in strong-field gravity. The mass of the compact object can be obtained through the mass function, which in turn is derived from Kepler's third law:

$$f(M_1) = \frac{K_2^3 P_{\rm orb}}{2\pi G} = \frac{M_1 \sin^3 i}{(1+q)^2}; \quad q = \frac{M_2}{M_1} = \frac{K_1}{K_2}$$

Since q is always positive and, in the case of LMXBs, ranges between $0 < q \lesssim 1$, the mass function provides a strict lower limit to M_1.

The maximum mass of a NS is determined by its equation of state (which is still under debate, e.g. Lattimer & Prakash, 2007). However, it is thought to be $\sim 3M_\odot$ (Rhoades & Ruffini, 1974; Kalogera & Baym, 1996). Hence, it is considered that the compact object is a dynamically confirmed BH when its mass function is greater than $f(M_1) > 3M_\odot$. Nevertheless, obtaining the mass function is not always straightforward since its accuracy depends on a reliable measurement of both $P_{\rm orb}$ and K_2 (the latter being the determining factor because of its cubic dependence on the mass function equation).

1.7.4 Radial velocity semi-amplitude of the companion star

In order to measure K_2, the canonical approach uses phase-resolved spectra (i.e. sampling a full orbit) in order to obtain the orbital motion of the photospheric absorption lines from the

companion. Since in the non-irradiated case, these absorptions are produced all over the surface of the secondary star, the Doppler shift of these features traces the motion of roughly the centre of mass of the donor. Thus, the radial velocity of the secondary is obtained for each spectrum by measuring the Doppler shift of the absorption lines by cross-correlation of the observed spectrum with a template star of matching spectral type.

For a circular orbit, the radial velocity (V_2) as a function of the orbital phase (ϕ) at certain time (t), is given by:

$$V_2 = \gamma + K_2 \sin(2\pi\phi); \quad \phi = (\mathrm{t} - \mathrm{t}_0)/P_{\mathrm{orb}}$$

where γ is the systemic velocity (radial velocity of the binary centre of mass), and t_0 the time of inferior conjunction of the donor star[2].

By fitting the obtained radial velocity curve in phase-folded space, K_2 and γ can be measured (see Fig. 1.10). It is worth noting that the irradiation of the secondary star leads to a phase-dependent change in the strength of its absorption lines. This produces a deviation of the radial velocity from a sinusoidal fit, with the consequent incorrect determination of K_2 (Wade & Horne, 1988).

Nevertheless, it is not always possible to detect these absorption lines in the data. The accretion disc can dominate over the companion star emission, veiling its absorption features at almost all wavelengths (see Sec. 1.5.1), so this technique is successfully applied only in transient systems during quiescence in the optical-NIR regime, where the disc emission is lower. Even so, as we mentioned in Sec. 1.6.2, the accretion disc of some transient systems (particularly at short orbital periods) still dominates the optical-NIR light during quiescence and the donor star cannot be detected. For these cases, Casares (2015) presented a correlation between the FWHM of the Hα emission line and K_2 during quiescence that can be used to estimate the latter.

1.7.5 K-velocity of the emission lines

In persistent and transient systems in outburst the bright accretion disc veils any spectral feature from the companion, and the technique described above is therefore not applicable. One alternative was developed by Steeghs & Casares (2002) in order to determine the motion of the secondary in these systems. They studied the persistent LMXB Sco X-1 and demonstrated that part of the Bowen blend is produced on the irradiated face of the donor star as a result of X-ray reprocessing. The Bowen technique uses high-resolution spectroscopy to resolve narrow components within the Bowen complex (see Fig. 1.6). A radial velocity curve can then be obtained from the velocity drift of one or more of these Bowen narrow lines. Ideally, the velocities are measured from Gaussian fitting of the most prominent transitions (N III 4634.12 Å, 4640.64 Å, and C III 4647.4 Å, 4650.1 Å).

The resulting radial velocity curve traces the movement of the light centre of the irradiated face of the companion (see Fig. 1.12). The projected velocity of the illuminated area is therefore lower than that of the of the centre of mass of the donor. Thus, the derived semi-amplitude of the radial velocity is not K_2 but a lower limit to it, which is known as K_{em}. This technique has been successfully applied to several objects (e.g. X1822–371, EXO 0748–676, Casares et al., 2003; Muñoz-Darias et al., 2009, respectively) and demonstrated to be suitable not only for persistent but also transient systems in outburst.

[2]Note that ϕ is defined as $0 \leq \phi < 1$, and $\phi = 0$ when the donor star is between the observer and the compact object, i.e. its inferior conjunction.

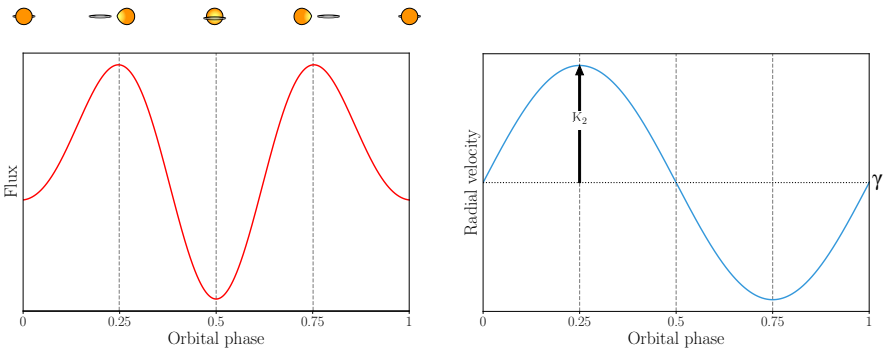

FIGURE 1.10— Sketch of a light curve (left) and a radial velocity curve of the companion star (right) for a complete orbit. The light curve shows the ellipsoidal modulation produced by the changing projected area of the companion in combination with the gravity darkening effect. Above this, a cartoon of a edge-on system representing the conventional orbital phase is displayed. We indicate K_2 and γ in the radial velocity curve (right).

1.7.6 Doppler tomography

In order to determine $K_{\rm em}$, measuring the radial velocity curve by fitting the sharp Bowen components is not always possible. In some cases, these emission lines may be affected (and even dominated) by contributions other than that from the donor star. Hence, Gaussian fitting is unreliable (see Ch. 3). In such cases, the technique known as Doppler tomography (Marsh & Horne, 1988) can be applied, provided that complete coverage of the orbital cycle is available. This is a robust analytical method that uses emission lines observed in phase-resolved spectra to reconstruct the emissivity map of the binary. This is achieved by decomposing an observed line profile into discrete emission sources which are characterised by their velocity. These velocities are measured in the inertial frame defined with its origin at the binary centre of mass and corotating with the system. The X-axis is defined in the direction of the line that joins the compact object with the companion, while Y runs perpendicular to it, in the direction of motion of the donor (see left panel in Fig. 1.11). The method is based on the following assumptions:

1. The intrinsic line width (e.g. thermal broadening) is negligible
2. Motion is parallel to the orbital plane
3. All the velocity vectors rotate with the system
4. The visibility of any point remains constant (there is no eclipses)
5. The flux from each element is constant in time

The method accuracy and reliability will be subject to the validity of the axioms listed above. However, Steeghs (2003) presented an extension of the technique that relaxes the fifth axiom permitting to deal with time-dependent emission sources.

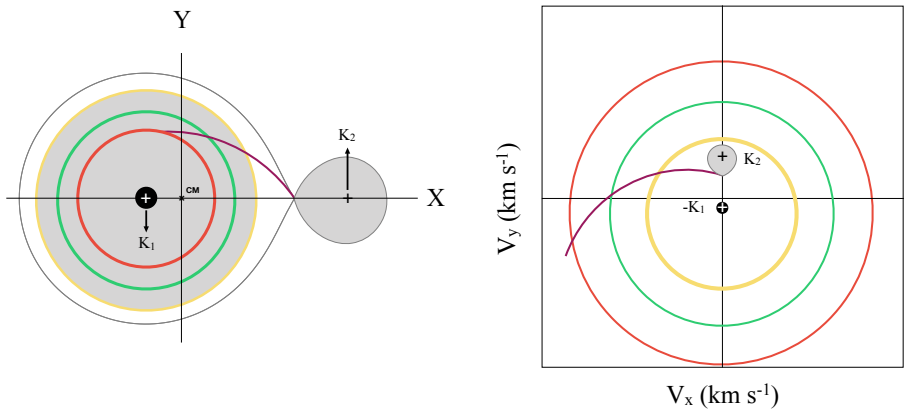

FIGURE 1.11— Diagram showing the correspondence between spatial coordinates (left) and velocity coordinates in a Doppler map (right). Some key components are schematically shown for both spaces following the same colour code. Yellow, green, and red indicate three disc annulus, while the purple line shows the gas-stream trajectory. In black is represented the compact object position and in grey the Roche lobe of the companion.

Doppler tomography makes use of all the spectra at once, and it is able to disentangle different emission sources in velocity space (i.e. Doppler coordinates). In Doppler coordinates, different emission components can be resolved (see right panel in Fig. 1.11). An emission line coming from the compact object will produce a spot located at ($V_x = 0$,$V_y = -K_1$), while that from the accretion disc appears as a ring-like pattern around this point. Note that in velocity space the disc is turned inside out, i.e. the inner disc appears at large velocities while the outer disc is represented as a ring at low velocity. The contribution from the donor is mapped as a compact spot located at ($V_x = 0$,$V_y = K_2$). It is important to take into account that the ephemeris and the corresponding γ of the system are needed as input to the Doppler map code (see Marsh, 2001, for a comprehensive review).

If the Doppler map is computed using the Bowen emission lines, the component formed in the donor's inner face will produce a spot located at ($V_x = 0$, $V_y = K_{em}$). Therefore, K_{em} can be accurately determined by measuring the centroid of this spot. In addition, Wang et al. (2017) showed that the significance of the result can be estimated by using bootstrapped maps.

1.7.7 The K-correction

In order to infer K_2 from the measured K_{em}, Muñoz-Darias et al. (2005) modelled the deviation between the reprocessed light-centre and the centre of mass of a Roche-lobe-filling star. They derived the so-called K-correction ($K_{corr} = K_{em}/K_2$) from numerical solutions and showed that it mainly depends on the accretion disc opening angle (α), on q, and also (but weakly) on i. This is so because the vertical extension of the accretion disc shields the innermost disc regions, where irradiation is produced, projecting a shadow over the companion star's surface. This affects the irradiation pattern, changing the centre of light, which is traced by K_{em} (see Fig. 1.12 and video

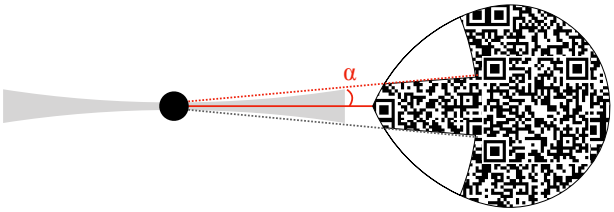

FIGURE 1.12— Scheme of the irradiated pattern over the inner face of the companion. The size of the illuminated area mainly depends on the opening angle of the accretion disc (α) and the mass ratio of the binary components (see attached video by scanning the 2-D barcode; credit: Gabriel Pérez – Servicio Multi-Media Instituto de Astrofísica de Canarias).

therein).

The Bowen technique, in combination with the K-correction, resulted in the first dynamical solution for a dozen of LMXBs (see e.g. Muñoz-Darias, 2009).

1.8 Accretion disc winds

X-ray winds have been established as a fundamental property of the soft state (see Sec. 1.5.2), both in NS and BH transients (e.g. Ponti et al., 2016, for a review). However, these hot accretion disc winds, probably impacting on the entire accretion process, are rarely observed during the hard state. Hence, they are mostly present when the radio jet is quenched, although there are some exceptions (e.g. King et al., 2015). Hot winds are revealed by X-ray spectroscopy, detected as blueshifted ($\sim$1000 km s^{-1}) absorptions, mainly of Fe XXV and Fe XXVI (Neilsen & Lee, 2009), and are observed to be equatorial (see Sec. 1.5.2).

The disappearance of the wind during the hard state is a matter of strong debate and it has been suggested to be related to different physical processes, such as the details of the wind-launching mechanism, photoionisation instabilities and over-ionisation of the ejecta (e.g. Chakravorty et al., 2013; Bianchi et al., 2017; Gatuzz et al., 2019). In addition, the presence of a continuous, state-independent wind has been proposed as a viable mechanism to explain the high efficiency of angular momentum removal inferred from fits to X-ray light curves (Tetarenko et al., 2018). On the other hand, low-ionisation disc winds have been detected via optical-IR observations in the form of P-Cygni profiles[3] and broad, non-Gaussian components in the emission-line wings. These features are standard accretion disc outflow signatures and were detected in H (Balmer) and He I transitions during the luminous outbursts of V404 Cyg (Casares et al., 1991; Muñoz-Darias et al., 2016; Mata Sánchez et al., 2018) and V4641 Sgr (Muñoz-Darias

[3]P-Cygni profiles are observed in massive stars and are associated with the presence of expanding outflows sustaining a large solid angle (e.g. stellar winds). The profile is the sum of a blue-shifted absorption produced by the material moving towards the observer and a red-shifted excess of flux caused by the receding gas. It was first observed in the star P-Cygni from which it has taken its name (Beals, 1929).

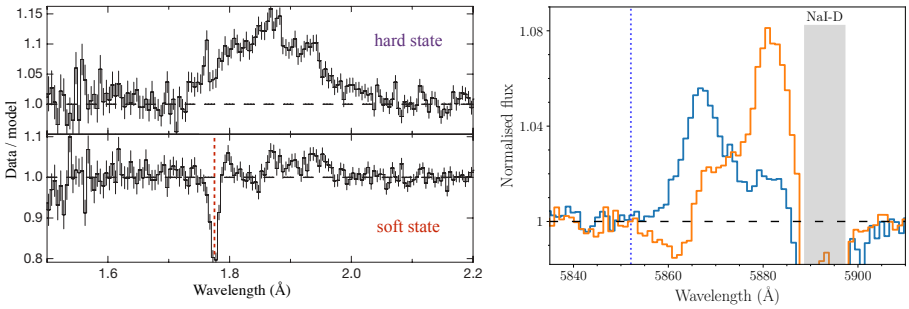

FIGURE 1.13— Left: X-ray spectra of GRS 1915+105. During the soft state (bottom panel) the strong blue-shifted Fe XXVI absorption at ~ 1.8 Å is observed (red, dashed line). The feature is absent during the hard state (top panel), when a broad Fe XXV emission line (~ 1.85 Å) is seen. Adapted from Neilsen & Lee (2009). Right: optical spectra of MAXI J1820+070 during outburst in the region around the He I-5876 Å line. The P-Cygni profile observed during the hard-state spectrum (orange) shows the presence of a wind with terminal velocity of ~ 1200 km s^{-1} (blue-dotted line), while no wind signature is observed in the soft-state spectrum (blue). The gray shading indicates the region contaminated by interstellar absorption. Adapted from Muñoz-Darias et al. (2019).

et al., 2018).

These winds are observed to be strong, with mass outflow rates that can significantly exceed the accretion rate ($\sim 4 \times 10^{-6} M_{\odot}$; Casares et al., 2019), being able to blow the inner parts of the disc away. In both cases (V404 Cyg and V4641 Sgr), such cold winds have been observed during the hard state. However, these sources undergo non-standard outbursts showing only the X-ray hard state accompanied by strong radio flaring.

In Muñoz-Darias et al. (2019) we presented an intensive optical spectroscopic follow-up of the transient MAXI J1820+070 obtained with a suite of the largest telescopes in the world. The system, a dynamically confirmed BH-LMXB (Torres et al., 2019), is among the brightest BH transients ever observed (Corral-Santana et al., 2016) reaching an optical magnitude of $g \sim 11.2$ mag at the peak of the outburst (Shidatsu et al., 2019). In contrast to V404 Cyg and V4641 Sgr, MAXI J1820+070 underwent a standard outburst, displaying both hard and soft states across the eight months spanned by the observations. We observed clear accretion disc wind features in the He I emission lines at 5876 and 6678 Å, as well as in Hα; namely P-Cygni profiles, broad emission-line wings, and strong line asymmetries. These optical winds are detected during the hard states of the outburst, while no wind signature was observed in the soft state. Some of the most conspicuous wind detections occur at the peak of the hard state, when both radio emission and strong jet activity are present. The winds showed two characteristic terminal velocities $v_{\rm t} \sim 1200$ and 1800 km s^{-1}.

In the same paper we used the equivalent width of Bowen + He II 4686 Å as a tracer of the ionisation state and found that the visibility of the winds during the soft state could be affected by the ionisation of the ejecta. Thus, winds could be present at all outburst phases but, during the soft state, the over-ionisation of the ejecta would prevent the winds from being detected at optical wavelengths. In addition, the $v_{\rm t}$ values measured in MAXI J1820+070 are similar to outflow velocities derived from (hard state) optical winds and (soft state) X-ray winds in other

systems (e.g. Muñoz-Darias et al., 2016; Ponti et al., 2016). This raises the question of whether or not hot and cold winds are intrinsically different or merely different observables of the same outflow at different stages of the outburst.

The detection of cold winds in MAXI J1820+070 has only been possible thanks to the brightness of the source and the exceptionally intensive and sensitive spectroscopic campaign carried out. This could imply that similar outflows are probably present in at least a significant fraction of BH X-ray binaries. Therefore, wind-like outflows would not be exclusive of bright, hot states but a common mass and angular momentum loss mechanism that operates through most of the accretion episode.

In this thesis we investigate the BH transient Swift J1357.2–0933, finding that the puzzling optical dips displayed by the system (Corral-Santana et al., 2013) are most likely due to the presence of a dense, clumpy wind with an equatorial geometry (see Ch. 4). The unique high orbital inclination of this BH transient reinforces the idea that optical winds are a common feature of these objects, and that winds in general can be found throughout the entire BH outburst.

1.9 Thesis outline

The main goal of this thesis is to investigate the properties of the X-ray heated accretion discs in LMXBs as their radial size and vertical extent, and the possible outflows (winds) associated. To this end, we exploit optical spectroscopy as the main technique, together with optical photometry and complementary X-ray data of three transient systems in outburst.

We study the newly discovered transient MAXI J1807+132, investigating the nature of the accretor by comparing the observed phenomenology with that of dynamically confirmed systems. We observe transitions between optical absorption and emission lines in the Balmer series, as well as several optical reflares in the light curve as the outburst decays. Based on the latter, we investigate the accretion disc size of the transient, which in turn we used to estimate its orbital period.

We also present the first empirical determination of the accretion disc vertical size in a LMXB in outburst. In doing this, we analyse a comprehensive observational campaign that comprised phase-resolved spectra from three consecutive outbursts of the NS transient Aquila X-1. We measure $K_{\rm em}$ by applying the Doppler tomography technique to the narrow N III emission lines resolved in our spectra. Using $K_{\rm em}$ together with K_2, q, and i (obtained during quiescence from NIR spectroscopy; Mata Sánchez et al., 2017), we determine the opening angle of the accretion disc by inverting the $K_{\rm corr}$ solutions. To this end, we take advantage of a Monte Carlo analysis that allows us to determine the error on the opening angle.

Finally, we also explore the nature of the optical dips observed in Swift J1357.2–0933. We obtained high time resolution spectroscopy with the 10.4-m Gran Telescopio Canarias throughout the dips during the 2017 outburst. We also carried out high time resolution photometry to explore the timing properties of these dips. The data set includes observing windows with up to 700 photometric points, so a Python-based photometry procedure was developed exclusively for their analysis (see Appendix A). This work reveals: i) the existence of a common phenomenon producing the dips during the outbursts of the system, and ii) that these dips are associated with a clumpy disc wind. This result has important implications since clumpy equatorial winds

might not be only characteristic of this system, but a common ingredient in the outflowing phenomenology observed in accreting BHs.

2

The complex evolution of the X-ray binary transient MAXI J1807+132 along the decay of its discovery outburst

Images of broken light
which dance before me like a million eyes
they call me on and on across the Universe

Across the universe, Lennon-McCartney

LMXBs can be distinguished from a regular star thanks to their strong X-ray radiation. Therefore, these objects are usually discovered when they go into outburst and become bright enough to be detected by the X-ray all-sky monitors such as the currently available INTEGRAL, MAXI, or Swift (Kuulkers et al., 2007; Matsuoka et al., 2009; Krimm et al., 2013, respectively). Nevertheless, many classes of objects exhibit transient X-ray emission (cataclysmic variables, HMXBs, gamma-ray bursts, and even active stars as O type and Wolf-Rayet), and the classification of a new X-ray transient is typically based on its optical spectrum and X-ray properties.

In this chapter we present optical and X-ray monitoring of the X-ray transient MAXI J1807+132 during the decay of its discovery outburst in 2017. Based on our observations and by analogy with other systems, we discuss a set of properties of MAXI J1807+132 such as the nature of the accretor, the spectral type of the companion, and the accretion disc size (i.e. the orbital period). This work was published in Monthly Notices of the Royal Astronomical Society, 2019, 484, 2078.

Monthly Notices of the ROYAL ASTRONOMICAL SOCIETY

MNRAS **484,** 2078–2088 (2019) doi:10.1093/mnras/sty3457
Advance Access publication 2018 December 20

The complex evolution of the X-ray binary transient MAXI J1807+132 along the decay of its discovery outburst

F. Jiménez-Ibarra [1,2]★ T. Muñoz-Darias [1,2] M. Armas Padilla [1,2] D. M. Russell [3] J. Casares [1,2] M. A. P. Torres,[1,2] D. Mata Sánchez [1,2,4,5] P. G. Jonker[4,6] and F. Lewis[7,8]

[1]*Instituto de Astrofísica de Canarias, Vía Láctea, La Laguna, E-38205 Santa Cruz de Tenerife, Spain*
[2]*Departamento de Astrofísica, Universidad de La Laguna, E-38206 Santa Cruz de Tenerife, Spain*
[3]*New York University Abu Dhabi, PO Box 129188, Abu Dhabi, United Arab Emirates*
[4]*SRON, Netherlands Institute for Space Research, Sorbonnelaan 2, NL-3584 CA Utrecht, the Netherlands*
[5]*Jodrell Bank Centre for Astrophysics, School of Physics and Astronomy, The University of Manchester, Manchester M13 9PL, UK*
[6]*Department of Astrophysics/IMAPP, Radboud University, PO Box 9010, NL-6500 GL Nijmegen, the Netherlands*
[7]*Faulkes Telescope Project, School of Physics and Astronomy, Cardiff University, The Parade, Cardiff CF24 3AA, UK*
[8]*Astrophysics Research Institute, Liverpool John Moores University, 146 Brownlow Hill, Liverpool L3 5RF, UK*

Accepted 2018 December 10. Received 2018 December 10; in original form 2018 October 1

ABSTRACT

MAXI J1807+132 is an X-ray transient discovered during the decay of an outburst in 2017. We present optical and X-ray monitoring of the source over more than 125 d, from outburst to quiescence. The outburst decay is characterized by the presence of several reflares with a quasi-periodic recurrence time of ∼6.5 d. We detect broad H and He emission lines during outburst, characteristic of transient low-mass X-ray binaries. These emission lines show strong variability from epoch to epoch and, in particular, during the early stages are found embedded into deep and very broad absorption features. The quiescent spectrum shows Hα in emission and no obvious signatures of the donor star. *XMM–Newton* and *Swift* spectra can be fitted with standard X-ray models for accreting black holes and neutron stars, although the obtained spectral parameters favour the latter scenario. Conversely, other observables such as the optical/X-ray flux ratio, the likely systemic velocity ($\gamma \sim -150\,\mathrm{km\,s^{-1}}$), and the reflares recurrence time suggest a black hole nature. We discuss all the above possibilities with emphasis on the strong similarities of MAXI J1807+132 with short orbital period systems.

Key words: accretion, accretion discs – black hole physics – stars: neutron – X-rays: binaries.

1 INTRODUCTION

About a million X-ray sources have been detected after more than 50 yr of X-ray astronomy. A fraction of these objects have been identified as low-mass X-ray binaries (LMXBs), binary systems harbouring a neutron star (NS) or a black hole (BH), which is accreting mass from a companion star typically less massive than the Sun. LMXBs provide a unique scenario to study extreme astrophysical phenomena such as accretion processes, the ejection of outflows, and the final stages of the stellar evolution (e.g. Casares & Jonker 2014; Fender & Muñoz-Darias 2016). The subclass known as transient LMXBs spend most part of their lives in a dormant, quiescent state, but show brightening episodes (outbursts) when they increase their luminosity by several orders of magnitude (e.g. Remillard & McClintock 2006). A significant fraction of the X-ray photons are absorbed in the accretion disc and then re-emitted at lower energies. As a result, the optical spectra of LMXBs are typically flat and blue with strong superimposed emission lines of H, He I, and He II (e.g. Charles & Coe 2006).

X-ray and optical observations provide complementary information in the study of LMXBs. On one hand, the nature of the compact object and its properties can be constrained based on the presence of thermonuclear burst (Galloway et al. 2008), pulsations and other timing features (van der Klis 2006; Motta 2016), and the spectral/timing X-ray evolution (Belloni, Motta & Muñoz-Darias 2011). On the other hand, dynamical solutions can be obtained from optical and near-infrared spectroscopy during quiescence (e.g. Casares, Charles & Naylor 1992). In addition, the inflow and outflow properties (e.g. winds) and some scale parameters are accessible when high-quality spectroscopy is achievable in the optical (e.g. Muñoz-Darias et al. 2016; Jiménez-Ibarra et al. 2018) or in X-rays (e.g. Díaz Trigo et al. 2006; Miller et al. 2006; Ponti et al. 2012).

★ E-mail: felipeji@iac.es

MAXI J1807+132 is a new X-ray transient discovered on 2017 March 13 by the nova-search system of the *Monitor of All-sky X-ray Image* (*MAXI*; Negoro et al. 2017). The source is located 15° above the Galactic plane at $\alpha, \delta = 18^{\rm h}08^{\rm m}07\overset{\rm s}{.}549, +13^{\circ}15'05\overset{''}{.}40$ (J2000; Kennea et al. 2017a,b). An optical counterpart consistent with the position of the transient was found in pre-outburst archival images of Panoramic Survey Telescope and Rapid Response System 1 (PanSTARRS-1) (Chambers et al. 2016). The object was identified in 31 multi-epoch images in five PanSTARRS-1 broad-band filters: *g*, *r*, *i*, *z*, and *y* (Denisenko 2017). The average magnitude is $g \sim 21$ but shows variability of up to 1 mag from epoch to epoch ($\sigma \sim 0.8$ over nine detections). Based on its high Galactic latitude, soft X-ray spectrum, ultraviolet (UV) brightness, and a tentative association with a previous flaring event, it was initially proposed as a candidate tidal disruption event (Kennea et al. 2017b; Negoro et al. 2017). However, the optical spectrum and other X-ray properties soon advocated for an X-ray binary association (Armas Padilla et al. 2017b; Munoz-Darias et al. 2017; Shidatsu et al. 2017b). Subsequently, Shidatsu et al. (2017a) favoured an NS accretor from analysis of *Swift* X-ray spectra in the range of 0.3–10 keV.

In this paper, we present a detailed optical and X-ray study of MAXI J1807+132 during the decay of its 2017 outburst. We carried out a photometric follow-up in three Sloan Digital Sky Survey (SDSS) bands (*g*, *r*, and *i*). Simultaneous optical spectroscopy was performed in six different epochs, both in outburst and quiescence. In addition, we analyse *XMM–Newton* archival observations taken soon after the *MAXI* alert.

2 OBSERVATIONS AND DATA REDUCTION

2.1 Optical data

The photometric observations were carried out from 2017 March 28 to July 12 over 35 different epochs. The data were obtained in the SDSS-*g*, -*r*, and -*i* bands using the 2-m Liverpool Telescope (LT) at the Observatorio del Roque de Los Muchachos (hereafter ORM) located in La Palma (Spain), and the 2- and 1-m class telescopes from Las Cumbres Observatory (LCO). In addition, a continuous light curve of 82 photometric points was taken (SDSS-*r*) using the 4.2-m William Herschel Telescope (WHT) at the ORM over a time-lapse of ∼160 min on July 22. The WHT data were reduced using ASTROPY-CCDPROC-based routines (Astropy Collaboration et al. 2013). Data from LCO were automatically processed through the BANZAI pipeline.[1] The LT data reduction was performed using the IO:O data reduction pipeline.[2] Flux calibration was carried out against nearby stars present in the PanSTARRs catalogue.

We also obtained intermediate resolution spectroscopy using the Optical System for Imaging and low-Intermediate Resolution Integrated Spectroscopy (OSIRIS; Cepa et al. 2000) attached to 10.4-m Gran Telescopio Canarias (GTC) at the ORM. We used the R1000B optical grism (2.12 Å pixel^{-1} at 5455 Å) covering the spectral range 3630–7500 Å. This, in combination with a slit width of 1 arcsec, provided a spectral resolution of 360 km s^{-1} [measured as the full width at half-maximum (FWHM) at ∼5577 Å]. A total of five spectra were obtained from March 28 to August 18. In addition, one spectrum was taken on 2018 July using the R1000R grism (2.62 Å pixel^{-1} at 7430 Å) covering the range 5100–10 000 Å.

[1] Beautiful Algorithms to Normalize Zillions of Astronomical Images. Code available at https://github.com/LCOGT/banzai
[2] http://telescope.livjm.ac.uk/TelInst/Pipelines/#ioo

Table 1. Spectroscopy of MAXI J1807+132.

Spectrum	Date	Exp. time (s)	SDSS-*g* (mag)
1	28-03-2017	600 (2 × 300)	18.36 ± 0.01
2	30-03-2017	900 (2 × 450)	19.16 ± 0.03
3	06-04-2017	3600 (2 × 1800)	19.08 ± 0.02
4	16-07-2017	3000 (2 × 1500)	21.60 ± 0.23
5	18-08-2017	1003	21.51 ± 0.08
6	13-07-2018	1800	21.36 ± 0.01[a]

[a] SDSS-*r*.

We reached a resolution of 381 km s^{-1} (FWHM at ∼5577 Å) using a slit width of 1 arcsec.

The spectroscopic data were debiased and flat-fielded using IRAF standard routines. We used regular arc lamp exposures taken on each observing night to carry out the pixel-to-wavelength calibration (HgAr+Ne lamps for the R1000B grism and HgAr+Ne + Xe for the R1000R). Cosmic rays were removed from the data using L.A.Cosmic (van Dokkum 2001) before extracting the spectra. We used the O I 5577.338 Å sky emission line and the MOLLY software to measure and then correct the subpixel velocity drifts (<100 km s^{-1}) introduced by instrumental flexure effects.

In addition, we used the acquisition images (SDSS-*g* and SDSS-*r*) to obtain photometric measurements contemporaneous with the spectroscopic observations (see Table 1). These were reduced in the same way as the WHT observations.

2.2 X-ray observations

2.2.1 Swift *data*

The *Neil Gehrels Swift Observatory* (Gehrels et al. 2004) pointed to MAXI J1807+132 on 29 occasions since it was reported as an active source. The on-board X-ray Telescope (XRT; Burrows et al. 2005) was operated in window timing (WT) mode for the first four pointings and in photon counting (PC) mode for the remaining observations. We used the HEASOFT v.6.20 package to reduce the data. We processed the raw XRT data running the XRTPIPELINE task selecting the standard event grades of 0-12 and 0-2 for the PC and WT mode observations, respectively. With XSELECT v2.4 we extracted the source events from a circular region of ∼40 arcsec radius. To compute the background, we used three circular regions of similar size and shape on an empty sky region (PC observations), and an annulus centred on the source with a 195 arcsec inner radius and 275 arcsec outer radius for the WT data.

The source is detected in 16 out of the 29 observations (i.e. with signal-to-noise ratio > 3σ), and only four of them have enough counts to carry out spectral analysis using χ^2 statistics (>50 counts; see Fig. 1, top panel). For these observations, we created exposure maps and ancillary response files following the standard *Swift* analysis threads,[3] and we acquired the last version of the response matrix files from the High Energy Astrophysics Science Archive Research Center (HEASARC) calibration database (CALDB). We grouped the spectra so as to attain a minimum of 10 photons bin^{-1} and, therefore, be able to use χ^2 statistics consistently.

[3] http://www.swift.ac.uk/analysis/xrt/

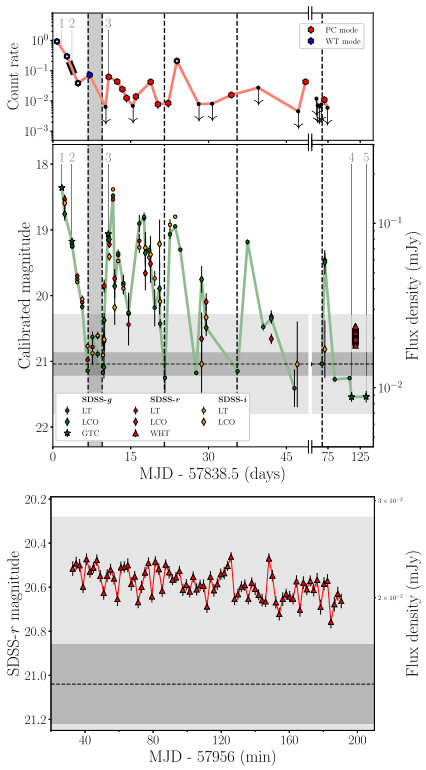

Figure 1. Top panel: X-ray light curve obtained with *Swift*/XRT. The thick black line indicates the *XMM–Newton* epochs. The observations employed in the spectral analysis are indicated as open symbols. Middle panel: photometric follow-up of MAXI J1807+132 in the SDSS-*g*, -*r*, and -*i* bands (green, red, and yellow markers, respectively). LT data are indicated by dots, while LCO data are marked as diamonds. At the end of the series, triangles show WHT points. GTC photometry from acquisition images is represented as stars and labelled in correspondence with spectra, except for the SDSS-*r* point and its corresponding spectrum taken on 2018 July; Table 1. The light green solid line joins the *g*-band points chronologically. The black dashed line shows the quiescence PanSTARRS *g*-band magnitude (after stacking) with its corresponding error displayed as dark grey area (21.04 ± 0.18; Denisenko 2017). The standard deviation of the nine pre-outburst epochs is indicated as a light grey area. The vertical dashed lines (and grey band) indicate epochs consistent with optical quiescence where the source is detected in X-rays. Bottom panel: zoom in of the WHT light curve spanning 160 min.

2.2.2 XMM–Newton *data*

Two observations were acquired with the *XMM–Newton* observatory (Jansen et al. 2001) on 2017 March 29 and 30 (gap between them of less than 7 h), with exposures of 19 and 29 ks, respectively. The configuration of the European Photon Imaging Camera (EPIC) was the same for both observations: MOS1 detector was operated in imaging small-window mode, and MOS2 and PN detectors in timing mode, all of them with the thin filter (Strüder et al. 2001; Turner et al. 2001). The source was not detected in the MOS2 camera. Because of strong episodes of background flaring, we proceeded to exclude data with count rates >0.4 counts s^{-1} at energies >10 keV and >0.5 counts s^{-1} at energies 10–20 keV for the MOS and PN cameras, respectively. For MOS1, we extracted source events from a circular region with a radius of 45 arcsec and a source-free circular region with a radius of 100 arcsec for the background. For PN, we extracted source and background events using the RAWX columns in [33:43] and in [10:18], respectively. Light curves and spectra, as well as associated response matrix files and ancillary response files, were generated following the standard analysis threads.[4] For MOS1, we rebinned the spectrum in order to include a minimum of 25 counts in every spectral channel, avoiding to oversample the FWHM of the energy resolution by a factor larger than 3. In the case of PN, we rebinned the spectrum in order to have a minimum signal-to-noise ratio of 6.

3 RESULTS

3.1 Outburst evolution

Our photometric follow-up is presented in the middle panel of Fig. 1 and Table A1. It mostly includes photometric points in the SDSS-*g* band complemented with measurements in SDSS-*r* and -*i*. The photometric monitoring started while the source was decaying from the outburst peak. Our first data point is almost 3 mag brighter than the quiescence magnitude reported by Denisenko (2017). Over the next 9 d the source gradually decayed from $g \sim 18.8$ to quiescence ($g \sim 21$). Subsequently, we observed an abrupt rise of $\sim$2.7 mag in 2 d. We identify up to seven rebrightening events superposed on a decay profile during the $\sim$70 d following the main outburst. This activity is detected in all the photometric bands studied. The secondary peaks have amplitudes of $\sim$2 mag above the quiescent level. A tentative periodic recurrence of $\sim$6 d is observed in the brightest four events (see Section 4.1).

During the photometric monitoring, six optical spectra were obtained (and labelled chronologically spectrum-1 to -6 hereafter). These are presented in Fig. 2. The first three spectra were taken when the source was brighter than $g \sim 19.5$, while the remaining found the source in quiescence at $g \sim 21$ (see Fig. 1 and Table 1). Hereafter, we refer to them as bright and faint spectra, respectively. The source showed pronounced spectral variability as it evolves through its complex outburst decay. We observed several emission lines in the bright spectra that are commonly seen in LMXBs in outburst. For example, spectrum-1 exhibits the Balmer series up to Hγ and He II 4686 Å. Less evident He I lines at $\sim$5875 and $\sim$6679 Å can be also identified. Fainter Balmer lines are present in the remaining bright spectra. Conversely, we cannot distinguish He transitions in spectrum-2 and -3. In addition, the Balmer emission lines appear embedded in broad absorptions that are stronger for the bluest lines. This pattern is particularly noticeable in spectrum-3, but it is still recognizable in spectrum-1 and -2. We note that spectrum-2 and -3 were obtained at comparable magnitudes (19.22 ± 0.02 and 19.06 ± 0.02 SDSS-*g* mag, respectively) but they show significant differences. Spectrum-2 is morphologically closer to spectrum-1.

[4] https://www.cosmos.esa.int/web/xmm-newton/sas-threads

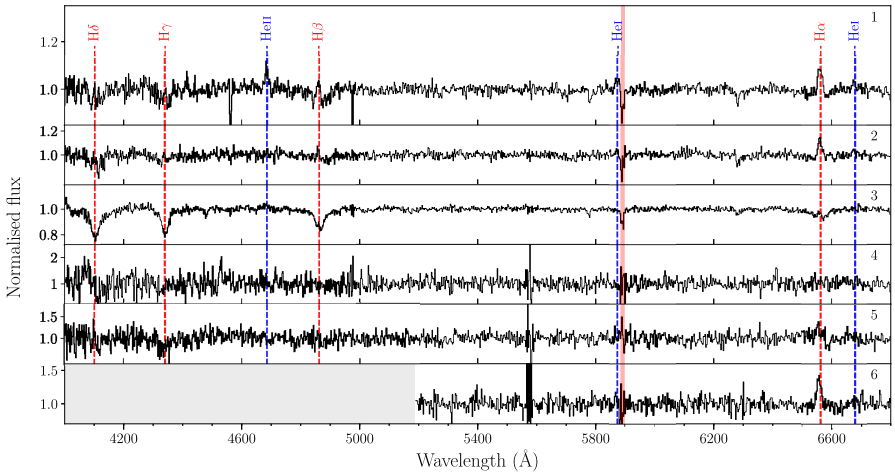

Figure 2. Multi-epoch spectroscopy of MAXI J1807+132 from GTC-OSIRIS (R1000B grism spectrum-1 to -5 and R1000R spectrum-6). Hydrogen (red) and He (blue) transitions are indicated by dashed lines. The NaI doublet is indicated as a red shadowed area at 5892 Å. Spectrum-4, -5, and -6 show strong residuals caused by sky subtraction at ∼5577 and ∼5890 Å.

However, for spectrum-3 the broad absorptions are remarkably deep and dominate over the emission lines.

We also observed morphological differences between faint spectra. Spectrum-4 and -5 are featureless, while spectrum-6 only exhibits Hα in emission. Absorption lines that could be associated with the companion star are not detected in any of the spectra.

3.2 Emission lines properties

We measured Doppler shifts in the emission lines observed in the spectrum-1, -2, -3, and -6 by fitting a multi-Gaussian model to previously normalized spectra. The lines considered and the model applied to each spectrum varies slightly from one to another following the morphological differences between them. For instance we modelled the Balmer lines and He II emission line in spectrum-1, while only Hα was fitted in spectrum-6. In order to obtain more reliable velocity measurements the separations between Gaussians were fixed. The broad absorptions underneath were taken into account when modelling the Balmer lines in spectrum-1, -2, and -3. To this end, we fitted broad Gaussian profiles keeping the relative separations between them fixed as in the case of the emission lines. We used a two-Gaussian model to account for the broad absorption components in the line profiles when present. The broadening effect on the emission lines due to the instrumental resolution was taken into account in the modelling. The results are shown in Fig. 3.

The derived emission line centroid velocities are presented in Table 2. In spectrum-3 the velocity obtained relies only on two emission lines strongly affected by the absorptions, and thus the uncertainty on the centroid velocity is a factor of ∼2 larger than that from spectrum-1. The derived velocities are consistent with each other within 1.5σ. We can tentatively associate these velocity shifts with the velocity of the centre of mass of the system, projected along

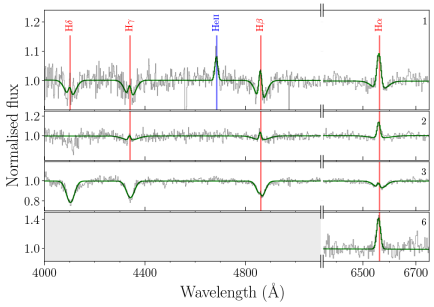

Figure 3. Trimmed spectra showing identified emission lines. The vertical lines represent the rest-frame position of the transition used on each model (red for the Balmer series and blue for He II 4686 Å). Green line shows the resulting model.

Table 2. Parameters from the observed emission lines. FWHM refers to the ensemble of all the emission lines.

Spectrum	FWHM ($km\,s^{-1}$)	Centroid velocity ($km\,s^{-1}$)	Hα FWHM ($km\,s^{-1}$)
1	796 ± 57	-106 ± 17	750 ± 63
2	557 ± 64	-147 ± 21	630 ± 74
3	468 ± 106	-169 ± 31	499 ± 142
6	–	-157 ± 35	698 ± 89

the line of sight, γ. We note that, on one hand, it seems unlikely that the three outburst spectra were taken at the same orbital phase and reflect the projected velocity of a particular structure of the accretion disc. On the other hand, it is highly unlikely that these velocities arise from some region (or regions) in the system showing the same radial velocity at different orbital phases. This argument is strongly favoured by the velocity measured from spectrum-6, taken more than a year later. We propose the average value $\gamma = -145 \pm 13\,\mathrm{km\,s^{-1}}$ as the systemic velocity of the binary, although a radial velocity curve is required to obtain a conclusive result.

The offset measured in the absorption components observed in spectrum-1, -2, and -3 is centred at $\sim$80 km s^{-1} showing uncertainties bigger than $\sim$190 km s^{-1}. Hence, we cannot constrain the velocity from these offsets.

We determined the FWHM of the emission lines from the multi-Gaussian fitting described above. In addition, we individually fitted the Hα emission line and its broad absorption profile with a double Gaussian model in spectrum-1, -2, and -3. Table 2 shows both the FWHM from all the emission lines considered and that from Hα for each spectra. The measured FWHMs of the broad components are 2851 ± 223, 4260 ± 531, and 2303 ± 45 km s^{-1} for spectrum-1, -2, and -3, respectively. Finally, the equivalent width (EW) of the Hα emission line in the spectra that are not contaminated by the absorption component are 1.96 ± 0.11 Å (spectrum-1), 2.89 ± 0.20 Å (spectrum-2), and 6.86 ± 0.70 Å (spectrum-6), whilst He II has EW 1.35 ± 0.17 Å in spectrum-1.

3.3 Extinction along the line of sight

The depth of interstellar absorption bands can be used to estimate the extinction along the line of sight. In particular, the colour excess $E(B-V)$ is correlated with the EW of the strongest component of the Na I doublet (NaD1, 5890 Å). This correlation is valid for EWs $\lesssim$0.5 Å (Munari & Zwitter 1997). In the bright spectra we observed the two components of the Na I doublet blended in a single absorption feature. No Na I components were detected in the faint spectra, which are contaminated by nearby sky emission lines (see Fig. 2). We averaged the three bright spectra and derived EW $=-1.10 \pm 0.08$ Å. This implies that the line is saturated and only a lower limit $E(B-V) \geq 0.3$ can be derived. This corresponds to $N_{\rm H} \gtrsim 2.4 \times 10^{21}$ cm^{-2} when applying the dust to gas relation ($N_{\rm H} = 2.87 \times 10^{21}$ cm^{-2} A_V; Foight et al. 2016) converting using the canonical relation $A_V = 3E(B-V)$. This value is still roughly consistent with the Galactic value, $N_{\rm H} \sim 1 \times 10^{21}$ cm^{-2} (Kalberla et al. 2005).

3.4 X-ray analysis

We used XSPEC (v.12.9.1; Arnaud 1996) to analyse the X-ray spectra. In order to account for interstellar absorption, we used the Tuebingen–Boulder interstellar medium absorption model (TBABS in XSPEC) with cross-sections of Verner et al. (1996) and abundances of Wilms, Allen & McCray (2000). We assumed a constant hydrogen equivalent column density of $N_{\rm H} = 1 \times 10^{21}$ cm^{-2} consistent with the low reddening expected for this direction (see previous section and Shidatsu et al. 2017a).

3.4.1 Swift

We used a simple power-law model to fit the four *Swift* spectra. We calculated the 2–10 keV unabsorbed flux in order to plot these points in the optical/X-ray correlation (see Section 3.5). We refer the reader to Shidatsu et al. (2017a) for more details on the *Swift* observations.

3.4.2 XMM–Newton

We simultaneously fit the 0.5–10 keV MOS1 and 0.7–10 keV PN spectra by using tied spectral parameters of both *XMM–Newton* observations. We included a constant factor (CONSTANT) fixed to 1 for PN spectra and free to vary for MOS1 spectra so to account for cross-calibration uncertainties between the instruments.

We used a simple two-component model to fit the spectra. We combined a soft component to account for either emission from an accretion disc or from a possible NS surface/boundary layer, and a hard component to model the inverse-Compton emission from the corona. Thus, we used a multicolour disc or single blackbody (BB) plus a thermally Comptonized continuum model (i.e. DISKBB + NTHCOMP and BBODYRAD + NTHCOMP in XSPEC; Mitsuda et al. 1984; Makishima et al. 1986; Zdziarski, Johnson & Magdziarz 1996; Życki, Done & Smith 1999). We assumed that the upscattered photons arise from the associated thermal component. Thus, we coupled $kT_{\rm seed}$ to either $kT_{\rm disc}$ or $kT_{\rm bb}$, respectively, and changed the seed photons shape parameter accordingly (*im-type* in NTHCOMP). The two spectral models return acceptable fits ($\chi^2 \sim$ 544–584 for 576 dof). The former yields a Comptonization asymptotic power-law photon index (Γ) of 1.8 ± 0.1 and a disc temperature of $kT_{\rm diskbb} = 0.33 \pm 0.01$ keV with a $N_{\rm in} = 15 \pm 2$. The latter translates to an unrealistic small internal disc radius ($R_{\rm in} \sim 5$ km applying the correction of Kubota et al. 1998; see also Armas Padilla et al. 2017a, and references therein) and compact object mass for a BH case (e.g. Tomsick et al. 2009). However, we note that it is not straightforward to obtain physically meaningful $R_{\rm in}$ values from this kind of modelling. We further discuss this in Section 4.2. The inferred 0.5–10 keV unabsorbed flux is $(6.7 \pm 0.1) \times 10^{-12}$ erg cm^{-2} s^{-1}, from which $\sim$36 per cent is produced by the thermal component. On the other hand, by using BBODYRAD + NTHCOMP we obtained $kT_{\rm bb} = 0.21 \pm 0.01$ keV and $N_{\rm bb} = 111 \pm 10$ while Γ is 2.1 ± 0.1. The inferred 0.5–10 keV unabsorbed flux is $(6.4 \pm 0.2) \times 10^{-12}$ erg cm^{-2} s^{-1}, from which $\sim$25 per cent is produced by the thermal component. It is important to bear in mind that due to the lack of data above 10 keV and the low statistics, we were not able to constrain the temperature of the electron corona ($kT_{\rm e}$) that was fixed to either 20 or 100 keV, typical values for NSs and BHs in the hard state (Burke, Gilfanov & Sunyaev 2017). This value does not have an impact on the obtained results (within errors). The best-fitting results are reported in Table 3 and Fig. 4 with uncertainties given at 90 per cent confidence level.

As described above, the two-component approach provides a good description of the data. However, we also tried other solutions. For instance, a simpler one-component model using a NTHCOMP was tested considering both scenarios: seed photons arising from a blackbody or from a disc blackbody. As expected, this forced the photon index to adopt higher values ($\Gamma = 2.48 \pm 0.03$) leaving significant residuals at high energies (χ^2 of 652 and 665 for 577 dof, respectively). This is reflected in the *F*-test, which yields a probability lower than 10^{-15} of improving the fit by chance when including a thermal component. In addition, more complex X-ray fitting, such as that provided by the three-component model proposed for NSs (e.g. Lin, Remillard & Homan 2007; Armas Padilla et al. 2017a) was also considered. However, even if this also reproduces the data, it does not produce a significant improvement

Table 3. Results from the X-ray spectral fits.

Instrument/ obs ID	$kT_{\rm bb/in}$ (keV)	$N_{\rm bb/in}$	Γ	$F_{\rm X,\,unabs}$ (10^{-12} erg cm^{-2} s^{-1})	$T_{\rm fr}$ (%)	χ^2_ν (dof)
Swift/XRT			TBABS∗(POWERLAW)			
00010037001	–	–	2.01 ± 0.06	19.1 ± 1.5	–	1.37 (145)
00010037002	–	–	2.1 ± 0.1	5.6 ± 1.0	–	0.89 (59)
00010037004	–	–	2.6 ± 0.8	0.33 ± 0.1	–	0.62 (25)
00010037017	–	–	1.8 ± 0.2	5.7 ± 1.4	–	1.06 (22)
XMM/EPIC			TBABS∗(BBODYRAD + NTHCOMP(BB))			
	0.21 ± 0.01	111 ± 10	2.1 ± 0.1	6.42 ± 0.1	25	1.01 (576)
			TBABS∗(DISKBB + NTHCOMP(DISK))			
	0.33 ± 0.01	15 ± 2	1.8 ± 0.1	6.7 ± 0.1	36	0.96 (576)

Note. Quoted errors represent 90% confidence levels. $F_{\rm X,\,unabs}$ represents the unabsorbed fluxes in the 2–10 and 0.5–10 keV bands for *Swift* and *XMM–Newton* observations, respectively. $T_{\rm fr}$ reflects the fractional contribution of the thermal component to the total unabsorbed 0.5–10 keV flux. When using NTHCOMP we coupled $kT_{\rm seed}$ to the temperature of the thermal component (i.e. $kT_{\rm disc}$ or $kT_{\rm bb}$; see Section 3.4.2).

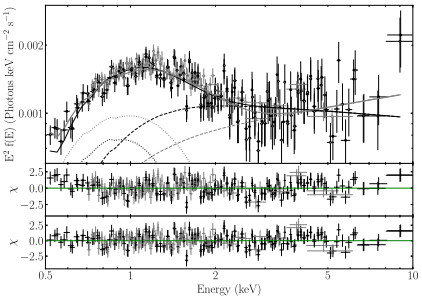

Figure 4. Top panel: unfolded MOS1 (black) and PN (grey) spectra of the March 29 (filled symbol) and 30 (open symbol) *XMM–Newton* observations. The solid black line represents the best fit for the BBODYRAD + NTHCOMP model, the thermal component is shown as a dotted line and the Comptonized component as a dashed line. In grey is represented the same for the DISKBB + NTHCOMP model. Middle panel: residuals in units of σ when using BBODYRAD + NTHCOMP model. Bottom panel: residuals in units of σ when using DISKBB + NTHCOMP model.

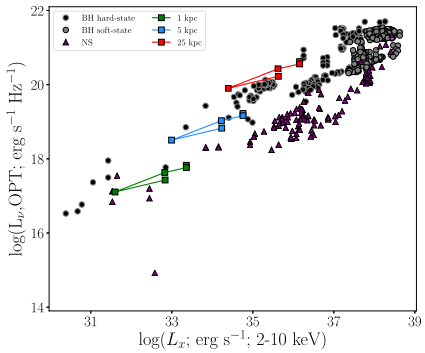

Figure 5. Optical-X-ray luminosity diagram (data from Russell et al. 2006, 2007). BHs in the hard and soft states are indicated as black and grey circles, respectively; NSs are plotted as violet triangles. Our data for MAXI J1807+132 are overplotted assuming three distances: 1 kpc (green square), 5 kpc (blue square), and 25 kpc (red square).

and its use is not justified given the limited quality of the data and the relatively narrow spectral coverage of *XMM–Newton*.

3.5 Optical/X-ray correlation

Based on quasi-simultaneous optical/near-infrared and X-ray observations of a large number of BHs and NSs, Russell et al. (2006) presented an empirical correlation between the nature of the compact object and its optical to X-ray luminosity ratio.

Fig. 5 shows the optical–X-ray luminosity diagram plotted using data from Russell et al. (2006) and Russell, Fender & Jonker (2007). We investigate the location of MAXI J1807+132 on this diagram in order to constrain the nature of the compact object. To this end, we use five luminosity ratios, obtained from a quasi-simultaneous optical and X-ray data. To compute the luminosities, we consider three possible distances: 1, 5, and 25 kpc. The optical/X-ray luminosity ratio suggests a BH nature for distances $\gtrsim 5$ kpc. For closer distances the source sits on a transitional and poorly sampled region in between the BH and NS populations. A NS accretor is favoured if the distance is $\sim$1 kpc or lower.

3.6 Quiescence photometry

The bottom panel of Fig. 1 shows the SDSS-*r* light curve of MAXI J1807+132 obtained on 2017 July 22 using the WHT. The source showed a mean brightness of 20.584 ± 0.003 mag, i.e. $\sim$0.6 mag above the quiescence level reporter by Denisenko (2017). The light curve shows a complex behaviour dominated by flickering with an amplitude of up to $\sim$0.3 mag and a variance of 0.06 mag with respect to the mean (this correspond to 0.0013 mJy over a mean of 0.021 mJy). We explored the WHT data set seeking for periodic oscillations using standard Lomb–Scargle techniques, but no modulations were found within the $\sim$2.5 h observed.

4 DISCUSSION

We presented a detailed optical and X-ray follow-up of MAXI J1807+132 during its 2017 outburst decay. This includes op-

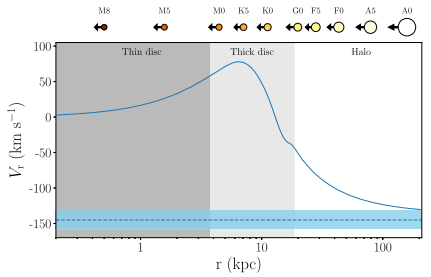

Figure 6. Radial velocity in the direction of MAXI J1807+132 as a function of r from the rotation curve of the Galaxy of Clemens (1985, blue solid line). Shadowed areas indicate the extension of the thin disc ($0 \leq z < 1$ kpc), the thick disc ($1 \leq z \leq 5$ kpc), and the halo ($h > 5$ kpc) projected on r (Gilmore & Reid 1983). The systemic velocity proposed and its corresponding error ($\gamma = -145 \pm 13$ km s^{-1}) are indicated as a blue dashed line. Top axis shows the spectral type of a main-sequence star of $g \sim 21$ placed at a distance r.

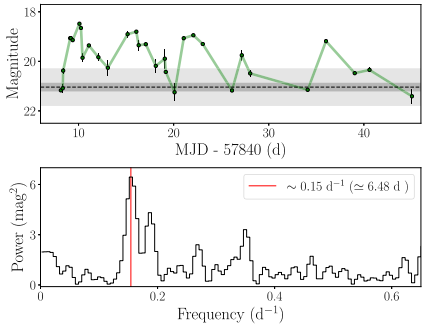

Figure 7. Top panel: segment of the SDSS-g light curve used for the Lomb–Scargle analysis. Bottom panel: resulted Lomb–Scargle periodogram from the data in the top panel. The red line indicates the position of the strongest peak that corresponds to ~ 0.15 d^{-1} ($\simeq 6.56$ d).

tical spectroscopy using GTC-10.4-m, which reveals emission lines typically observed in LMXB spectra. The Balmer series appears in emission superposed to broad absorption features that are deeper towards the blue. Similar line profiles were observed before in other LMXBs (e.g. Nova Velorum 1993, GRO J0422+32, XTE J1118+480, XTE J1859+226; Bailyn & Orosz 1995; Casares et al. 1995; Dubus et al. 2001; Zurita et al. 2002, respectively). This can be interpreted as the result of emission lines being originated from photoionization in an optically thin region above the disc, combined with absorption lines arising from inner optically thick regions. The absorption throats were discussed in detail by Dubus et al. (2001). They found that the formation of these features is favoured by (hard X-ray) irradiation, since hard X-ray photons can access deeper disc. In addition, these features are not expected in high inclination systems, since the absorptions tend to disappear as the inclination increases, affected by the limb darkening in the two-dimensional disc picture. If this interpretation is correct, it would suggest an intermediate to low orbital inclination for the system. However, we note that both GRO J0422+32 and XTE J1118+480 have intermediate to high inclinations ($45^\circ \pm 2^\circ$ and 68°–79°; Gelino & Harrison 2003; Khargharia et al. 2012), respectively.

We have measured a systematic velocity offset in the emission lines observed both in outburst and quiescence that we interpret as the binary systemic velocity ($\gamma = -145 \pm 13$ km s^{-1}). We now consider a simple kinematic model for the Milky Way to compare the observed γ with the radial velocity expected for a given distance in the direction of the source [i.e. $V_r(r, l, b)$, where r is the heliocentric distance]. We use the rotation curve from Clemens (1985), which is defined both in the inner and outer Galaxy, and assumes that the Milky Way follows a pure circular motion. Fig. 6 shows the radial velocity in the direction $(l, b) = (40.^\circ12, 15.^\circ50)$ as a function of r. The kinetic model predicts negative radial velocities beyond $r \sim 10$ kpc, while velocities consistent with the measured γ are only expected for $r > 100$ kpc. Clearly the observed systemic velocity cannot be explained by the rotation curve of the Galaxy, not even if the object is located in the very outskirts of the Galaxy. We also use b to determine the vertical distance above the Galactic plane (z) as a function of r. Shadowed areas on Fig. 6 indicate the extension of the thin disc ($0 \leq z < 1$ kpc), the thick disc ($1 \leq z \leq 5$ kpc), and the halo ($z > 5$ kpc) projected on r (Gilmore & Reid 1983). We observe that the Galactic rotation could account for the measured radial velocity only if the source is located in the outer halo. For lower elevations the source requires a significant peculiar velocity, whether it belongs to the thin disc or to the thick disc. Such high peculiar velocities have been observed in LMXBs and are typically interpreted as natal kicks resulted from asymmetries in the supernova explosion. Finally, assuming that the quiescent light is dominated by the companion star, it is possible to estimate its spectral classification based on the quiescent magnitude (Denisenko 2017). However, the high variability observed suggests that the disc emission is significant even in quiescence. We therefore infer an upper limit to the expected spectral type of the donor for the case of a main-sequence star at a given distance (assuming $g \sim 21$). The results are schematically presented in the top axis of the Fig. 6.

4.1 Reflares during the decay

We detected up to seven brightening episodes during the outburst decay. A quasi-periodic recurrence can be noticed by visual inspection (Fig. 7). We computed a Lomb–Scargle periodogram of the SDSS-g points between MJD 57848 and MJD 57885, when the brightening episodes are observed and resolved (i.e. sampling better than one point every 3 d). The light curve analysed and the resulting periodogram are shown in Fig. 7. The periodogram was produced using the LombScargle-python class (VanderPlas 2018). We find the highest power at ~ 0.15 d^{-1} that yields a period of 6.5 d. The origin of these periodic brightening episodes is uncertain, but it has been proposed they might be related to a cyclical mechanism involving the accretion rate (Augusteijn, Kuulkers & Shaham 1993; Chen, Livio & Gehrels 1993; Mineshige 1994). In the context of the model proposed by Augusteijn et al. (1993) the brightening episodes or reflares are 'echoes' of the main outburst. X-ray illumination of the companion star triggers enhanced mass transfer and subsequent minioutbursts. Within this picture, the recurrence time of each rebrightening is the time that a perturbation takes to travel across the accretion disc radius ($R_{\rm out}$). The heating front propagates at $v \approx \alpha v_{\rm s}$, where α is the viscosity parameter and $v_{\rm s}$ the sound speed (Lasota 2001). Under the assumption of a hot accretion disc ($\alpha = 0.1$ and

$v_s = 15\,\mathrm{km\,s^{-1}}$; Menou, Hameury & Stehle 1999), we obtain $R_{out} \sim 8.4 \times 10^{10}$ cm. Using this R_{out} we estimate the binary period (P) using $R_{out} \simeq 1.2 \times 10^{11} M^{1/3} P^{2/3}$ cm, where M is the mass of the compact object expressed in $M_\odot$ (King, Kolb & Burderi 1996). We adopt the two canonical masses for compact stars, $1.4\,M_\odot$ for an NS and $8\,M_\odot$ for a BH. We obtained P(NS) ∼12 h and P(BH) ∼5 h, respectively.

Using the above orbital periods, we can calculate the mean density of the companion star that fills its Roche lobe (Faulkner, Flannery & Warner 1972), and compare it with that of typical main-sequence stars (Cox 2000). We find that, for the case of a BH, the donor would be an M0–M2 main sequence while for the case of an NS it would be a F0–F5 main sequence. The distance to the system can be inferred in both cases, if we combine the lower limit to the quiescent magnitude and the spectral types above. The source is expected to be at $\gtrsim 4$ and $\gtrsim 35$ kpc for a BH and NS system, respectively (see Fig. 6). We note that only the BH case is consistent with the constraints devised by the optical/X-ray luminosity diagram. All in all, these broad observational properties seem to support the case of a BH binary instead of an NS.

For simplicity, we have considered in the above a main-sequence companion star. However, we note that a somewhat evolved donor cannot be ruled out. Indeed, subgiant companions are thought to be present in some LMXBs with orbital periods $\gtrapprox$2 d (e.g. V404 Cygni, GX 339−4, and XTE J1550−564; King 1993; Muñoz-Darias, Casares & Martínez-Pais 2008). For instance, in the case of GX 339−4, the 'stripped-giant' model predicts magnitudes in the range of $r \sim$ 21–24 for a distance within ∼6–15 kpc. This magnitude range is compatible to that observed in MAXI J1807+132 during quiescence (PanSTARRS-1 broad-band filters r =21.19 ± 0.09; Denisenko 2017). We also explored the possibility of a giant (luminosity class III) companion star. We assumed the observed quiescent magnitude to be the magnitude of the donor, and compared it with that expected for a field giant at given distance. Using the absolute magnitudes tabulated in Cox (2000) we obtained a distance in the range of ∼100–180 kpc, which effectively discards a giant companion.

4.2 On the nature of the compact object

The definitive determination of the nature of the compact object in an LMXB requires of either the detection of unequivocal NS features (i.e. pulsations or thermonuclear burst) or, alternatively, a dynamical measurement of the mass of the compact object. When none of the above is available, the likely nature of the accretor can be studied based on other observables.

(i) *X-ray spectral properties*. Albeit both NS and BH transients share a common phenomenology during outburst (e.g. Muñoz-Darias, Motta & Belloni 2011; Muñoz-Darias et al. 2014), the X-ray spectral modelling usually requires of an extra component to account for the emission from the NS surface (or its surroundings; e.g. Lin et al. 2007; Armas Padilla et al. 2017a, 2018). Using this argument Shidatsu et al. (2017a) favoured an NS nature based on spectral fitting of the *Swift* data. Here, we have also included deeper *XMM–Newton* observations in the X-ray spectral analysis. Although we are able to fit our data with both BH- and NS-like spectral models, some of the spectral parameters are more similar to those typically obtained for NS systems at low accretion regimes. In particular, the low disc normalization (N_{in} = 15) and the ∼30 per cent thermal contribution to the total flux (0.5–10 keV) challenge the BH scenario. BH systems at low luminosities reveal cold disc components, but these tend to have much larger normalization values (a proxy for the inner disc radius) and provide in most of the cases lower contributions to the observed flux (e.g. Reis, Fabian & Miller 2010; Armas Padilla et al. 2014a; Shidatsu et al. 2014; Plant et al. 2015). On the other hand, several NS LMXBs accreting at low luminosities show thermal fractions consistent with those reported in this work. These have been observed in both persistent (e.g. Armas Padilla, Wijnands & Degenaar 2013; Degenaar et al. 2017; Armas Padilla et al. 2018) and transient systems (e.g. Degenaar, Wijnands & Miller 2013; Campana et al. 2014; Arnason et al. 2015). In addition, we can compare the $\Gamma = 2.48 \pm 0.03$ obtained when solely using the Comptonization component with the photon index/X-ray luminosity diagram presented in Wijnands et al. (2015), which shows a distinctive evolution for BHs and NSs at $L_X < 10^{36}$ erg s^{-1}. Even if the distance to MAXI J1807+132 (and therefore the luminosity) is not constrained, we find that an NS accretor is qualitatively favoured. All in all, our X-ray fitting agrees to some extent with Shidatsu et al. (2017a) and favours an NS nature. However, it is important to bear in mind that a BH-like spectral modelling provides an equally good fit to the data, with the exception of the low normalization value of the disc component. Nevertheless, we note that we are using data with limited signal-to-noise ratio and simple (Newtonian) disc models. Thus, we conclude that only from the X-ray fitting point of view we are not able to definitely constrain the nature of the compact object.

(ii) *The optical/X-ray luminosity diagram*. This tool was initially presented by Russell et al. (2006) and has been subsequently applied to several objects (e.g. Armas Padilla et al. 2011; Hernández Santisteban et al. 2018). This test produces a 'qualitative' classification, and strongly relies on the distance to the source. In Fig. 5, we show that a BH nature is clearly favoured for $d \gtrsim 5$ kpc, while lower distances would also allow for an NS accretor. This latter case is significantly favoured for very low distances ($d \lesssim 1$ kpc).

(iii) *We have estimated the systemic velocity from the optical spectra (Section 3.2)*. We find that it is likely large and negative ($\gamma \sim -150\,\mathrm{km\,s^{-1}}$). Comparing this value with the rotation curve of the Galaxy (Fig. 6) it is clear that a natal kick would be needed to explain γ, unless the system is located unrealistically far away. In addition, distances between ∼5 and 10 kpc would require very high proper motions in excess of $\sim$200 km s^{-1}. In any case, for $d \gtrsim 5$ kpc (i.e. BH scenario according to the optical/X-ray ratio) the system would be located in the thick disc, which itself favours a natal kick to explain such a large height above the Galactic plane (Repetto, Davies & Sigurdsson 2012). We note that a population of transient BH-LMXBs is known to be present at these high latitudes (see e.g. Kuulkers et al. 2013; Mata Sánchez et al. 2015, and references therein). Interestingly, several of these BH systems have relatively short orbital periods (see table 2 in Shahbaz et al. 2013). On the other hand, at very close distances, systemic velocities within the range observed in NS-LMXBs would be required (Ramachandran & Bhattacharya 1997; Mata Sánchez et al. 2015). Both, a large height above the Galactic plane and a close distance agree with the low extinction along the line of sight detected in X-rays (Section 3.3).

(iv) *Orbital period estimates from reflares*. The presence of several optical reflares is one of the most relevant characteristics of the outburst decay of MAXI J1807+132. This kind of phenomena has been observed previously not only in cataclysmic variables (e.g. Patterson et al. 1998) but also in several BH transients such as XTE J1118+480, XTE J1859+226, GRO J0422 + 32 (see Zurita et al. 2006, and references therein), and NSs systems (e.g. Torres et al. 2008; Patruno et al. 2016). These binaries have orbital periods of 4.1, 6.6, and 5.1 h, respectively (Corral-Santana et al. 2016).

For the case of GRO J0422+32 the reflare recurrence time can be estimated and it is about 7–8 d (see e.g. fig. 2 in Zurita et al. 2006). This is remarkably similar to the one we have measured in MAXI J1807+132 (6.5 d) and from which we have inferred an orbital period of ∼5 h should the compact object be a BH (Section 4.1). Therefore, it seems that the proposed scenario (irradiation induced changes in mass transfer) might work for GRO J0422+32 and for extension for MAXI J1807+132. If this is the case, the NS scenario is clearly disfavoured, as it would imply an orbital period of ∼12 h, which would place the source at $\gtrsim$35 kpc (see above). At this large distance the optical luminosity diagram strongly suggests a BH nature.

(v) *X-ray detections near optical quiescence*. Finally, it is worth mentioning that MAXI J1807+132 is detected in X-rays at optical magnitudes consistent with optical quiescence (e.g. grey band in Fig. 1). This naively suggests that (i) the system might be also close to X-ray quiescence and (ii) it might be relatively nearby as truly quiescent LMXBs can be only detected within a few kpc and using deep *XMM*/*Chandra* observations (e.g. Armas Padilla et al. 2014b, and references therein). By stacking several *Swift* observations around day 75 (see Fig. 1) and assuming a power-law spectrum with a photon index of 2 with $N_{\rm H} = 1 \times 10^{-21}$ cm^{-2}, we obtain an unabsorbed flux of 2.8×10^{-13} erg s^{-1}. The combined count rate is slightly lower than our faintest detection, so this stacking is effectively our dimmest detection of the source. By imposing the lowest X-ray quiescence luminosities observed in LMXBs, i.e. 0.5×10^{31} (BH) and 5×10^{31} (NS) erg s^{-1} (fig. 3 in Armas Padilla et al. 2014b), we place lower limits to the distance of 0.5 and 1.5 kpc for a BH and an NS, respectively. These values would imply very late spectral type donors, even within the brown dwarf regime (Fig. 6). However, it seems more likely that the source is not in X-ray quiescence between reflares as it usually takes several months to reach this state. In addition, the 'optical quiescence' detected by PanSTARRs and in this work could be far from true optical quiescence. This is supported by the apparent lack of companion star features in the faintest spectra and by the flickering observed in the WHT light curve (Fig. 1). We note that even if our faintest detection (see above) corresponds to luminosities as low as 1×10^{33} erg s^{-1} (the quiescent luminosity shown by several BH and NS) a distance of >6.5 kpc is obtained. This, combined with the optical/X-ray luminosity diagram, disfavours the NS case.

5 CONCLUSIONS

We have presented an extensive observational study of the newly discovered X-ray transient MAXI J1807+132 during its 2017 outburst decay. All the observables are consistent with those typically observed in transient LMXBs during outburst. The system displays striking properties such as dramatic changes in the optical spectrum and several reflares with a periodicity of 6.5 d. We have explored the possible nature of the compact object, and both an NS and a BH accretor are consistent with the observations. Although the NS scenario is favoured by the X-ray fitting (see also Shidatsu et al. 2017a), it also requires fine-tuning of other parameters and some of the suggested explanations for the observed phenomenology to be wrong (e.g. reflares). All considered, we think that MAXI J1807+132 might be very similar to the BH transient GRO J0422+32. Both objects have shown the same transitions between optical absorption and emission lines, as well as reflares with very similar recurrence times. GRO J0422+32 has an orbital period of 5.1 h and an M4 donor (Casares et al. 1995; Webb et al. 2000; Gelino & Harrison 2003), a solution very close to that we have found for MAXI J1807+132 if the reflares are induced by irradiation of the companion star. Both objects have the same quiescent magnitude ($r \sim 21$) but GRO J0422+32 shows donor spectral features in the spectrum, which suggest that its distance of 2.5 kpc could be a lower limit to that of MAXI J1807+132. However, we stress that, in any case, an NS accretor cannot be ruled out and is even favoured by the X-ray modelling. For this to be the case a distance in the range of ∼1.5–5 kpc would be required. Future observations of the source, either during new outbursts or quiescence, should provide insights on the nature of the compact object and other properties of the source.

ACKNOWLEDGEMENTS

We are grateful to the anonymous referee for useful comments and suggestions that have improved the paper. We acknowledge support by the Spanish MINECO under grant AYA2017-83216-P. This study is based on observations made with the Gran Telescopio Canarias (GTC), installed on the Spanish Observatorio del Roque de los Muchachos of the Instituto de Astrofísica de Canarias in the island of La Palma. The authors are thankful to the GTC team that carried out the Target of Opportunity (ToO) observations. We are thankful to Phil Charles, Nathalie Degenaar, Rudy Wijnands, and Tom Maccarone for useful discussion on the nature of the system. The WHT is operated on the island of La Palma by the Isaac Newton Group of Telescopes in the Spanish Observatorio del Roque de los Muchachos of the Instituto de Astrofísica de Canarias. This study is also based on observations made with the Liverpool Telescope operated on the island of La Palma by Liverpool John Moores University in the Spanish Observatorio del Roque de los Muchachos of the Instituto de Astrofísica de Canarias with financial support from the UK Science and Technology Facilities Council. TM-D is supported by RYC-2015-18148. MAP's research is funded under the Juan de la Cierva Fellowship Programme (IJCI-2016-30867) from MINECO. MAPT acknowledges support via a Ramón y Cajal Fellowship (RYC-2015-17854). DMS acknowledges support from the ERC under the European Union's Horizon 2020 research and innovation programme (grant agreement no. 715051; Spiders). MOLLY software developed by T. R. Marsh is gratefully acknowledged. The Faulkes Telescope Project is an education partner of LCO. The Faulkes Telescopes are maintained and operated by LCO.

REFERENCES

Armas Padilla M., Degenaar N., Patruno A., Russell D. M., Linares M., Maccarone T. J., Homan J., Wijnands R., 2011, MNRAS, 417, 659
Armas Padilla M., Wijnands R., Degenaar N., 2013, MNRAS, 436, L89
Armas Padilla M., Wijnands R., Altamirano D., Méndez M., Miller J. M., Degenaar N., 2014a, MNRAS, 439, 3908
Armas Padilla M., Wijnands R., Degenaar N., Muñoz-Darias T., Casares J., Fender R. P., 2014b, MNRAS, 444, 902
Armas Padilla M., Ueda Y., Hori T., Shidatsu M., Muñoz-Darias T., 2017a, MNRAS, 467, 290
Armas Padilla M., Wijnands R., Degenaar N., Munoz-Darias T., Jimenez-Ibarra F., Mata Sanchez D., Casares J., Charles P. A., 2017b, Astron. Telegram, 10224
Armas Padilla M., Ponti G., De Marco B., Muñoz-Darias T., Haberl F., 2018, MNRAS, 473, 3789
Arnason R. M., Sivakoff G. R., Heinke C. O., Cohn H. N., Lugger P. M., 2015, ApJ, 807, 52
Arnaud K. A., 1996, in Jacoby G. H., Barnes J., eds, ASP Conf. Ser. Vol. 101, Astronomical Data Analysis Software and Systems V. Astron. Soc. Pac., San Francisco, p. 17

Astropy Collaboration et al., 2013, A&A, 558, A33
Augusteijn T., Kuulkers E., Shaham J., 1993, A&A, 279, L13
Bailyn C. D., Orosz J. A., 1995, ApJ, 440, L73
Belloni T. M., Motta S. E., Muñoz-Darias T., 2011, Bull. Astron. Soc. India, 39, 409
Burke M. J., Gilfanov M., Sunyaev R., 2017, MNRAS, 466, 194
Burrows D. N. et al., 2005, Space Sci. Rev., 120, 165
Campana S., Brivio F., Degenaar N., Mereghetti S., Wijnands R., D'Avanzo P., Israel G. L., Stella L., 2014, MNRAS, 441, 1984
Casares J., Jonker P. G., 2014, Space Sci. Rev., 183, 223
Casares J., Charles P. A., Naylor T., 1992, Nature, 355, 614
Casares J., Marsh T. R., Charles P. A., Martin A. C., Martin E. L., Harlaftis E. T., Pavlenko E. P., Wagner R. M., 1995, MNRAS, 274, 565
Cepa J. et al., 2000, in Iye M., Moorwood A. F., eds, Proc. SPIE Vol. 4008, Optical and IR Telescope Instrumentation and Detectors. SPIE, Bellingham, p. 623
Chambers K. C. et al., 2016 preprint (arXiv:1612.05560)
Charles P. A., Coe M. J., 2006, in Lewin W., van der Klis M., eds, Compact Stellar X-Ray Sources. Cambridge Univ. Press, Cambridge, p. 215
Chen W., Livio M., Gehrels N., 1993, ApJ, 408, L5
Clemens D. P., 1985, ApJ, 295, 422
Corral-Santana J. M., Casares J., Muñoz-Darias T., Bauer F. E., Martínez-Pais I. G., Russell D. M., 2016, A&A, 587, A61
Cox A. N., 2000, Allen's Astrophysical Quantities. AIP Press, New York
Degenaar N., Wijnands R., Miller J. M., 2013, ApJ, 767, L31
Degenaar N., Pinto C., Miller J. M., Wijnands R., Altamirano D., Paerels F., Fabian A. C., Chakrabarty D., 2017, MNRAS, 464, 398
Denisenko D., 2017, Astron. Telegram, 10217
Díaz Trigo M., Parmar A. N., Boirin L., Méndez M., Kaastra J. S., 2006, A&A, 445, 179
Dubus G., Kim R. S. J., Menou K., Szkody P., Bowen D. V., 2001, ApJ, 553, 307
Faulkner J., Flannery B. P., Warner B., 1972, ApJ, 175, L79
Fender R., Muñoz-Darias T., 2016, in Haardt F., Gorini V., Moschella U., Treves A., Colpi M., eds, Lecture Notes in Physics, Vol. 905, Astrophysical Black Holes. Springer International Publishing, Switzerland, p. 65
Foight D. R., Güver T., Özel F., Slane P. O., 2016, ApJ, 826, 66
Galloway D. K., Muno M. P., Hartman J. M., Psaltis D., Chakrabarty D., 2008, ApJS, 179, 360
Gehrels N. et al., 2004, ApJ, 611, 1005
Gelino D. M., Harrison T. E., 2003, ApJ, 599, 1254
Gilmore G., Reid N., 1983, MNRAS, 202, 1025
Hernández Santisteban J. V., Knigge C., Pretorius M. L., Sullivan M., Warner B., 2018, MNRAS, 473, 3241
Jansen F. et al., 2001, A&A, 365, L1
Jiménez-Ibarra F., Muñoz-Darias T., Wang L., Casares J., Sánchez D. M., Steeghs D., Padilla M. A., Charles P. A., 2018, MNRAS, 474, 4717
Kalberla P. M. W., Burton W. B., Hartmann D., Arnal E. M., Bajaja E., Morras R., Pöppel W. G. L., 2005, A&A, 440, 775
Kennea J. A., Evans P. A., Beardmore A. P., Krimm H. A., Romano P., Yamaoka K., Serino M., Negoro H., 2017a, Astron. Telegram, 10215
Kennea J. A. et al., 2017b, Astron. Telegram, 10216
Khargharia J., Froning C. S., Robinson E. L., Gelino D. M., 2012, AJ, 145, 21
King A. R., 1993, MNRAS, 260, L5
King A. R., Kolb U., Burderi L., 1996, ApJ, 464, L127
Kubota A., Tanaka Y., Makishima K., Ueda Y., Dotani T., Inoue H., Yamaoka K., 1998, PASJ, 50, 667
Kuulkers E. et al., 2013, A&A, 552, A32
Lasota J.-P., 2001, New Astron. Rev., 45, 449
Lin D., Remillard R. A., Homan J., 2007, ApJ, 667, 1073
Makishima K., Maejima Y., Mitsuda K., Bradt H. V., Remillard R. A., Tuohy I. R., Hoshi R., Nakagawa M., 1986, ApJ, 308, 635
Mata Sánchez D., Muñoz-Darias T., Casares J., Corral-Santana J. M., Shahbaz T., 2015, MNRAS, 454, 2199
Menou K., Hameury J.-M., Stehle R., 1999, MNRAS, 305, 79
Miller J. M., Raymond J., Fabian A., Steeghs D., Homan J., Reynolds C., van der Klis M., Wijnands R., 2006, Nature, 441, 953
Mineshige S., 1994, ApJ, 431, L99
Mitsuda K. et al., 1984, PASJ, 36, 741
Motta S. E., 2016, Astron. Nachr., 337, 398
Munari U., Zwitter T., 1997, A&A, 318, 269
Muñoz-Darias T., Casares J., Martínez-Pais I. G., 2008, MNRAS, 385, 2205
Muñoz-Darias T., Motta S., Belloni T. M., 2011, MNRAS, 410, 679
Muñoz-Darias T., Fender R. P., Motta S. E., Belloni T. M., 2014, MNRAS, 443, 3270
Muñoz-Darias T. et al., 2016, Nature, 534, 75
Munoz-Darias T., Jimenez-Ibarra F., Mata Sanchez D., Armas Padilla M., Casares J., Charles P. A., 2017, Astron. Telegram, 10221
Negoro H. et al., 2017, Astron. Telegram, 10208
Patruno A., Maitra D., Curran P. A., D'Angelo C., Fridriksson J. K., Russell D. M., Middleton M., Wijnands R., 2016, ApJ, 817, 100
Patterson J. et al., 1998, PASP, 110, 1290
Plant D. S., Fender R. P., Ponti G., Muñoz-Darias T., Coriat M., 2015, A&A, 573, A120
Ponti G., Fender R. P., Begelman M. C., Dunn R. J. H., Neilsen J., Coriat M., 2012, MNRAS, 422, L11
Ramachandran R., Bhattacharya D., 1997, MNRAS, 288, 565
Reis R. C., Fabian A. C., Miller J. M., 2010, MNRAS, 402, 836
Remillard R. A., McClintock J. E., 2006, ARA&A, 44, 49
Repetto S., Davies M. B., Sigurdsson S., 2012, MNRAS, 425, 2799
Russell D. M., Fender R. P., Hynes R. I., Brocksopp C., Homan J., Jonker P. G., Buxton M. M., 2006, MNRAS, 371, 1334
Russell D. M., Fender R. P., Jonker P. G., 2007, MNRAS, 379, 1108
Shahbaz T., Russell D. M., Zurita C., Casares J., Corral-Santana J. M., Dhillon V. S., Marsh T. R., 2013, MNRAS, 434, 2696
Shidatsu M. et al., 2014, ApJ, 789, 100
Shidatsu M. et al., 2017a ApJ, 850, 155
Shidatsu M. et al., 2017b, Astron. Telegram, 10222
Strüder L. et al., 2001, A&A, 365, L18
Tomsick J. A., Yamaoka K., Corbel S., Kaaret P., Kalemci E., Migliari S., 2009, ApJ, 707, L87
Torres M. A. P. et al., 2008, ApJ, 672, 1079
Turner M. J. L. et al., 2001, A&A, 365, L27
van der Klis M., 2006, in Lewin W., van der Klis M., eds, Compact Stellar X-Ray Sources. Cambridge Univ. Press, Cambridge, p. 39
VanderPlas J. T., 2018, ApJS, 236, 16
van Dokkum P. G., 2001, PASP, 113, 1420
Verner D. A., Ferland G. J., Korista K. T., Yakovlev D. G., 1996, ApJ, 465, 487
Webb N. A., Naylor T., Ioannou Z., Charles P. A., Shahbaz T., 2000, MNRAS, 317, 528
Wijnands R., Degenaar N., Armas Padilla M., Altamirano D., Cavecchi Y., Linares M., Bahramian A., Heinke C. O., 2015, MNRAS, 454, 1371
Wilms J., Allen A., McCray R., 2000, ApJ, 542, 914
Zdziarski A. A., Johnson W. N., Magdziarz P., 1996, MNRAS, 283, 193
Zurita C. et al., 2002, MNRAS, 334, 999
Zurita C. et al., 2006, ApJ, 644, 432
Życki P. T., Done C., Smith D. A., 1999, MNRAS, 309, 561

APPENDIX A: OPTICAL PHOTOMETRY OF MAXI J1807+132 IN THE 2017 OUTBURST

The photometric data presented in this work are listed in Table A1. They correspond to the SDSS-*g*, -*r*, and -*i* bands. The telescope used in each case is indicated.

Table A1. SDSS-*g*, -*r*, and -*i* photometry of MAXI J1807+132 (LT, LCO, and GTC).

	SDSS-*g* (mag)			SDSS-*r* (mag)		SDSS-*i* (mag)	
Date	LT	LCO	GTC	LT	LCO	LT	LCO
28-03-2017	–	18.76 ± 0.10	18.36 ± 0.01	–	18.54 ± 0.07	–	18.59 ± 0.10
30-03-2017	19.24 ± 0.02	–	19.22 ± 0.02	19.24 ± 0.02	–	19.26 ± 0.02	–
31-03-2017	19.75 ± 0.03	–	–	19.70 ± 0.04	–	19.79 ± 0.04	–
01-04-2017	20.17 ± 0.04	–	–	20.10 ± 0.04	–	20.05 ± 0.06	–
02-04-2017	21.14 ± 0.04	–	–	20.98 ± 0.04	–	20.77 ± 0.04	–
03-04-2017	20.63 ± 0.09	–	–	20.78 ± 0.11	–	20.88 ± 0.17	–
04-04-2017	20.89 ± 0.06	–	–	20.62 ± 0.04	–	20.61 ± 0.06	–
05-04-2017	21.17 ± 0.03	21.09 ± 0.17	–	21.08 ± 0.03	20.69 ± 0.14	20.90 ± 0.04	20.67 ± 0.17
06-04-2017	19.06 ± 0.02	19.14 ± 0.04	19.06 ± 0.02	19.09 ± 0.02	19.22 ± 0.04	19.15 ± 0.01	19.41 ± 0.06
07-04-2017	18.48 ± 0.04	19.86 ± 0.18	18.65 ± 0.05	18.54 ± 0.03	19.74 ± 0.15	18.38 ± 0.02	20.18 ± 0.26
08-04-2017	19.36 ± 0.06	–	–	19.38 ± 0.03	–	19.47 ± 0.03	–
09-04-2017	19.83 ± 0.15	–	–	19.81 ± 0.10	–	19.89 ± 0.08	–
10-04-2017	20.26 ± 0.31	–	–	20.44 ± 0.32	–	20.28 ± 0.24	–
12-04-2017	18.90 ± 0.13	–	–	19.17 ± 0.10	–	19.27 ± 0.08	–
13-04-2017	18.80 ± 0.07	19.35 ± 0.21	–	–	19.66 ± 0.26	18.82 ± 0.04	19.27 ± 0.24
14-04-2017	19.31 ± 0.08	–	–	–	19.52 ± 0.29	19.42 ± 0.07	19.37 ± 0.28
15-04-2017	20.18 ± 0.28	–	–	–	–	19.74 ± 0.12	–
16-04-2017	20.43 ± 0.07	19.89 ± 0.39	–	–	20.41 ± 0.69	20.09 ± 0.08	19.21 ± 0.37
17-04-2017	21.25 ± 0.35	–	–	–	–	–	–
18-04-2017	19.07 ± 0.07	–	–	–	–	18.92 ± 0.08	–
19-04-2017	18.95 ± 0.02	–	–	–	–	18.80 ± 0.02	–
20-04-2017	19.30 ± 0.02	–	–	–	–	–	–
23-04-2017	21.18 ± 0.03	–	–	–	–	–	–
24-04-2017	–	19.75 ± 0.20	–	–	20.70 ± 0.40	–	21.04 ± 0.75
25-04-2017	–	20.49 ± 0.13	–	–	20.10 ± 0.13	–	20.33 ± 0.17
01-05-2017	21.15 ± 0.03	–	–	–	–	–	–
03-05-2017	19.18 ± 0.04	–	–	–	–	–	–
06-05-2017	20.48 ± 0.05	–	–	–	–	–	–
07-05-2017	–	20.35 ± 0.08	–	–	20.66 ± 0.08	–	20.32 ± 0.10
12-05-2017	21.41 ± 0.29	–	–	–	–	–	21.05 ± 0.65
16-05-2017	–	–	–	–	19.10 ± 0.65	–	–
31-05-2017	21.03 ± 0.03	–	–	–	–	–	–
04-06-2017	–	19.49 ± 0.19	–	–	19.46 ± 0.11	–	20.82 ± 0.44
19-06-2017	21.27 ± 0.03	–	–	–	–	–	–
12-07-2017	21.25 ± 0.03	–	–	–	–	–	–
16-07-2017	–	–	21.54 ± 0.08	–	–	–	–
18-08-2017	–	–	21.47 ± 0.04	–	–	–	–

This paper has been typeset from a TEX/LATEX file prepared by the author.

3

Bowen emission from Aquila X-1: evidence for multiple components and constraint on the accretion disc vertical structure

Dear Prudence, open up your eyes
dear Prudence, see the sunny skies

Dear Prudence, Lennon-McCartney

Since its discovery in 1973, Aquila X-1 (Kunte et al., 1973) has been detected in outburst every approximately two years. This made it one of the most studied LMXBs and a prototypical transient system. Aquila X-1 is known to harbour a NS since it has exhibited both coherent X-ray pulsations (Casella et al., 2008) and thermonuclear bursts (e.g. Galloway et al., 2008). A dynamical solution was achieved by Mata Sánchez et al. (2017) who, using NIR spectroscopy during quiescence, observed the absorption lines of the companion star.

In this chapter we present an optical spectroscopy campaign of three consecutive outbursts of Aquila X-1. We observed the narrow components of the Bowen blend in our phase-resolved spectra, which allowed us to measure $K_{\rm em}$ using the Doppler tomography technique. On the basis of the definition of $K_{\rm corr}$ (see Sec 1.7.7), we used the obtained $K_{\rm em}$ in combination with the K_2, q, and i values derived by our group in Mata Sánchez et al. (2017) to empirically determine the opening angle of the accretion disc providing a robust estimation of its associated error for the very first time.

This work was published in Monthly Notices of the Royal Astronomical Society, 2018, 474, 4717.

Monthly Notices of the ROYAL ASTRONOMICAL SOCIETY
MNRAS **474,** 4717–4722 (2018) doi:10.1093/mnras/stx2926
Advance Access publication 2017 November 14

Bowen emission from Aquila X-1: evidence for multiple components and constraint on the accretion disc vertical structure

F. Jiménez-Ibarra,[1,2]★ T. Muñoz-Darias,[1,2] L. Wang,[3] J. Casares,[1,2,4] D. Mata Sánchez,[1,2] D. Steeghs,[3] M. Armas Padilla[1,2] and P. A. Charles[4,5]

[1]*Instituto de Astrofísica de Canarias, Vía Láctea, La Laguna, E-38205, Santa Cruz de Tenerife, Spain*
[2]*Departamento de Astrofísica, Universidad de La Laguna, E-38206, Santa Cruz de Tenerife, Spain*
[3]*Department of Physics, University of Warwick, Gibbet Hill Road, Coventry CV4 7AL, UK*
[4]*Department of Physics, Astrophysics, University of Oxford, Denys Wilkinson Building, Keble Road, Oxford OX1 3RH, UK*
[5]*Department of Physics and Astronomy, University of Southampton, Southampton SO17 1BJ, UK*

Accepted 2017 November 6. Received 2017 November 3; in original form 2017 September 22

ABSTRACT

We present a detailed spectroscopic study of the optical counterpart of the neutron star X-ray transient Aquila X-1 during its 2011, 2013 and 2016 outbursts. We use 65 intermediate resolution GTC-10.4 m spectra with the aim of detecting irradiation-induced Bowen blend emission from the donor star. While Gaussian fitting does not yield conclusive results, our full phase coverage allows us to exploit Doppler mapping techniques to independently constrain the donor star radial velocity. By using the component N III 4640.64/4641.84 Å, we measure $K_{\rm em} = 102 \pm 6\,{\rm km\,s^{-1}}$. This highly significant detection ($\gtrsim 13\sigma$) is fully compatible with the true companion star radial velocity obtained from near-infrared spectroscopy during quiescence. Combining these two velocities we determine, for the first time, the accretion disc opening angle and its associated error from direct spectroscopic measurements and detailed modelling, obtaining $\alpha = 15.5\,^{+2.5}_{-5}$ deg. This value is consistent with theoretical work if significant X-ray irradiation is taken into account and is important in the light of recent observations of GX339-4, where discrepant results were obtained between the donor's intrinsic radial velocity and the Bowen-inferred value. We also discuss the limitations of the Bowen technique when complete phase coverage is not available.

Key words: accretion, accretion discs – stars: neutron – X-rays: binaries.

1 INTRODUCTION

Low-mass X-ray binaries (LMXBs) are stellar systems comprising a low-mass star ($\lesssim 1\,{\rm M}_\odot$) which transfers matter on to a compact object (either a neutron star or a black hole) via an accretion disc. Depending on their long-term behaviour, we can distinguish between persistent systems, those constantly accreting material at high rates, and transient systems, which spend the majority of their lives in a dormant, quiescent state. The latter show sporadic outbursts lasting weeks to years, when their X-ray luminosity increases typically to ≥ 10 per cent of the Eddington luminosity, becoming at least as bright as persistent sources (see e.g. van der Klis 2006; Belloni, Motta & Muñoz-Darias 2011; Fender & Muñoz-Darias 2016 for reviews).

Classical dynamical studies of LMXBs rely on the spectroscopic detection of the companion star at optical and/or near-infrared wavelengths (e.g. Charles & Coe 2006; Casares & Jonker 2014). However, the optical counterparts of most transient LMXBs are faint in quiescence ($V > 22$–23) and to obtain phase-resolved spectra during this epoch is not always an easy task. In addition, even if optical spectroscopy is feasible, the companion star features might be veiled by the disc emission (e.g. Mata Sánchez et al. 2015b). The situation is even more complex during outburst, when the radiation coming from the outer accretion disc generally dominates even in the near-infrared (Mata Sánchez et al. 2015a).

The so-called Bowen technique was developed to measure the orbital motion of the donor star using narrow fluorescence lines within the Bowen blend region, a typical spectral feature of LMXBs in outburst. In a few key systems, it has been shown that these narrow components originate as a result of the X-ray reprocessing on the irradiated side of the donor. Thus, a lower limit to the radial velocity of the companion (K_2) can be established by measuring Doppler shifts from these emission components (i.e $K_{\rm em}$; Steeghs & Casares 2002, see also Muñoz-Darias et al. 2007 for Bowen blend time-lags consistent with the donor star). Narrow emission lines in the Bowen region have been observed in a dozen or so objects (Cornelisse et al. 2008; Muñoz-Darias 2009), which led to the first

★ E-mail: felipeji@iac.es

estimate of the system parameters in three transient systems in outburst (e.g. Wang et al. 2017) and several persistent sources (e.g. Casares et al. 2006).

Aquila X-1 (Aql X-1) is a neutron star transient LMXB that has shown recurrent outbursts since its discovery by Friedman, Byram & Chubb (1967). It has a short outburst recurrence time of ∼2 yr, being one of the most prolific and widely studied X-ray transients (e.g. Miller-Jones et al. 2010; Coti Zelati et al. 2014; Muñoz-Darias et al. 2014). During the 2004 outburst, Cornelisse et al. (2007) constrained K_2 by using the Bowen technique, and obtained $K_{em} = 247 \pm 8\,km\,s^{-1}$. This result is no longer compatible with the dynamical solution derived from near-infrared spectroscopy taken during quiescence Mata Sánchez et al. (2017, hereafter MS2017). The discrepancy could result from spurious emission coming from localized regions of the disc that contribute to the Bowen blend (Hynes et al. 2004). Similarly, a recent spectroscopic study of the black hole transient GX 339-4 (Heida et al. 2017) during one of its short quiescence epochs ruled out a companion star origin for the K_{em} reported by Hynes et al. (2003). Both the Aql X-1 and GX 339-4 outburst studies have in common a limited phase coverage.

In this paper, we present phase-resolved optical spectroscopy of Aql X-1 taken during the 2011, 2013 and 2016 outbursts. We take advantage of a complete phase coverage to exploit the Doppler mapping technique in order to accurately determine K_{em}, deriving a value which is now fully compatible with the near-infrared measurement. Subsequently, we use K_2 from MS2017 and the ratio between K_{em} and K_2 (K_c; as defined in Muñoz-Darias, Casares & Martínez-Pais 2005, hereafter MD2005) to determine the opening angle of the accretion disc, therefore constraining its vertical extent during outburst.

2 OBSERVATIONS AND DATA REDUCTION

We obtained phase-resolved spectroscopy of Aql X-1 with the Optical System for Imaging and low-Intermediate Resolution Integrated Spectroscopy (OSIRIS) located in the Nasmyth-B focus of the 10.4 m Gran Telescopio Canarias (GTC) at the Observatorio del Roque de los Muchachos (La Palma, Spain). We used the optical grism R2500V (0.8 Å pix^{-1}) centred at 5185 Å with spectral coverage between 4500 and 6000 Å and two different slit widths (0.8 and 1 arcsec), which yielded a velocity resolution of 132.3 ± 0.2 and 172.9 ± 0.2 $km\,s^{-1}$, respectively [full-width at half-maximun (FWHM)] at 4624.27 Å.

A total of 65 spectra were acquired during three different outburst episodes, in 2011, 2013 and 2016, as detailed in Table 1. Note that in one case we have averaged four spectra of 300s in two bins (600 s) to increase the signal-to-noise ratio, but the effective integration time is still short compared to the binary orbital period (<0.02 in phase). The spectra were taken over 19 different epochs [see Fig. 1 (bottom)] with seeing in the range 0.75–1.45 arcsec.

The data were de-biased and flat-fielded using IRAF[1] standard routines. The pixel-to-wavelength calibration was made using a regular HgAr+Ne+Xe arc lamp exposure taken on each observing block. Before extracting the spectra, cosmic rays were removed from the 2-D spectra using LACOSMIC (van Dokkum 2001). Velocity drifts due to instrumental flexure effects were corrected (<40 $km\,s^{-1}$) using the MOLLY software and the O I 5577.338 Å line from the sky spectra.

[1] IRAF is distributed by National Optical Astronomy Observatories, operated by the Association of Universities for Research in Astronomy, Inc., under contract with the National Science Foundation.

Table 1. Journal of observations GTC/OSIRIS spectroscopy of Aql X-1.

Date	UT interval	No.	Exp. time	Orb. phase interval[a]
26/10/2011	20:53–21:25	4	600 s	0.58–0.61
29/11/2011	19:50–20:01	2	600 s	0.58–0.60
25/06/2013	03:18–03:54	4	671 s	0.74-0.77
05/07/2013	03:28–04:03	4	671 s	0.42–0.45
09/07/2013	01:24–01:59	4	671 s	0.38–0.41
11/07/2013	01:44–03:08	8	671 s	0.93–0.00
14/07/2013	02:07–02:43	4	671 s	0.75–0.78
03/08/2016	01:04–02:04	6	700 s	0.23–0.28
05/08/2016	00:47–02:00	8	600 s	0.75–0.81
05/08/2016	23:47–23:57	2	600 s	0.96–0.97
07/08/2016	00:04–00:15	2	600 s	0.24–0.25
07/08/2016	23:39–23:54	2	600 s	0.48–0.50
11/08/2016	23:03–23:14	2	600 s	0.52–0.53
13/08/2016	22:59–23:10	2	600 s	0.05–0.06
18/08/2016	21:28–21:44	2	600 s (2 × 300 s)	0.30–0.32
21/08/2016	22:34–22:44	2	600 s	0.16–0.17
24/08/2016	22:24–22:34	2	600 s	0.95–0.96
27/08/2016	21:52–22:03	2	600 s	0.72–0.73
29/08/2016	21:19–21:43	3	685 s	0.23–0.25

Note. [a]For orbital ephemeris see text Section 3.1.

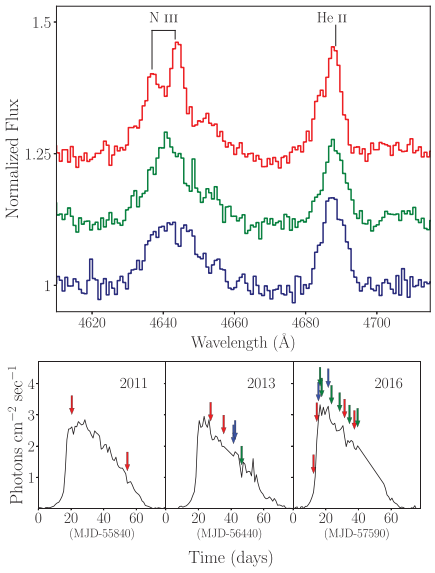

Figure 1. Top: examples of normalized spectra of Aql X-1 in the Bowen blend region for each of the three groups defined in the text (Section 3): spectra with securely identified N III narrow emission lines (red line; positive offset applied), spectra showing unidentified narrow components (green line; positive offset applied) and spectra with no narrow components within the Bowen blend (blue line). Bottom: X-ray light curves of Aql X-1 during the 2011, 2013 and 2016 outbursts obtained with the Monitor of All-sky X-ray Image (MAXI). Arrows indicate the time of our GTC observing blocks using the same colour code as that of the top panel.

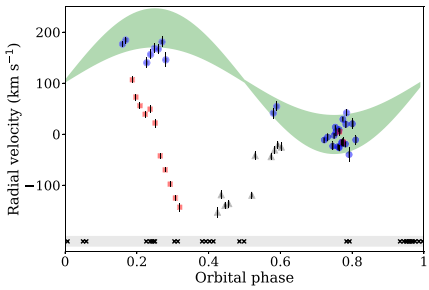

Figure 2. Radial velocity as a function of orbital phase derived from Gaussian fits of the Bowen blend narrow components. The light green area represents the region where the radial velocity is consistent with that arising from the inner side of the companion star. Blue dots indicate velocities compatible (within 3σ) with the expected radial velocity of the donor, while grey triangles correspond to those that are not consistent. Crosses show the phases of those spectra in which N III lines could not be identified. The velocities obtained from the VLT data (Cornelisse et al. 2007) are shown as red squares.

3 RESULTS

The Bowen blend complex is detected in all 65 GTC spectra. However, its relative strength and shape show strong variability. We can distinguish three groups: (i) 38 spectra show narrow lines that we could unambiguously identify as N III 4634.13 and N III 4640.64/4641.84 Å, (ii) 19 spectra show narrow features, but do not enable a clear identification of the N III components, and (iii) 8 spectra do not show narrow components at all (see Fig. 1 top).

3.1 Gaussian fitting

Previous studies of several objects have shown that narrow components within the Bowen blend arise from the irradiated side of the companion star. Thus, $K_{\rm em} < K_2$ can in principle be obtained by directly measuring their radial velocity curve over a full orbital period (e.g. Steeghs & Casares 2002). To this end, we carried out Gaussian fits to the Bowen narrow components on each of the 38 spectra in which we clearly identify N III narrow lines. All the spectra were initially normalized, to then fit the Bowen profile using a 3-Gaussian model. Two narrow components were used to fit the N III 4634.13 Å and N III 4640.64/4641.84 Å emission lines. A broad component was added in order to model the underlying broad Bowen blend profile. The position and height of each Gaussian were set as free parameters, but the relative separation between both narrow components was imposed to be constant in order to obtain a single and more stable velocity solution. The FWHM of the Gaussians were fixed to 200 and 1150 km s^{-1} for the narrow and broad components, respectively. Thus, five parameters were optimized through least-squares fitting, yielding a velocity offset and its associated error for every spectrum. In order to compute the orbital binary phases, we used the ephemeris from MS2017: $T_0 = 2455810.387 \pm 0.005$ d and $P_{\rm orb} = 0.7895126 \pm 0.000\,0010$ d. The velocity offset as a function of the orbital phase is shown in Fig. 2. We cannot clearly identify orbital motion of the companion; instead, a more complex distribution is observed (dots and triangles in Fig. 2).

Taken into account the system parameters given in MS2017, we used K_c for the case of low orbital inclination to compute limiting cases for the expected $K_{\rm em}$ in Aql X-1. Even though a clear radial velocity curve was not observed, 28 points are consistent with the expected radial velocity, i.e. less than 3σ from the region defined by the $K_{\rm em}$ limit cases. The same analysis was applied to the Very Large Telescope (VLT) data presented in Cornelisse et al. (2007). The phase-dependent velocity offsets derived from these data are consistent with those originally reported (we consider now the MS2017 ephemeris), but are not compatible with those expected for the companion star. Thus, our Gaussian fitting suggests that the Bowen blend is tracing more than one emission region.

3.2 Doppler mapping

Doppler tomography (Marsh & Horne 1988) inverts phase-resolved data to obtain a brightness distribution in velocity space (i.e. Doppler coordinates). This technique is suitable to search for emission features from the companion star in faint systems or those for which the spectra are contaminated by other components. The Doppler coordinate frame corotates with the system, with the origin placed on its centre of mass. The V_x-axis is defined by the line that joins the compact object with the companion star, while the V_y-axis is set in the direction of the velocity of the companion. Thus, when the correct systemic velocity (γ) is used as the input to the Doppler code, the centre of mass of the system is placed at the origin on the Doppler map [i.e. (V_x, V_y) = (0,0)]. The emission from the donor should appear as a compact spot along the V_y-axis and $K_{\rm em}$ can be determined from the position of the centroid of this spot if spectra are folded on the correct ephemeris. Doppler tomography makes use of spectra that ideally sample the orbital period in full. It uses all at once, being able to separate out the different emission sources.

Following Wang et al. (2017), we used all our 65 spectra to compute Doppler maps. These were constructed by using the second generation (PYTHON/C++ based), maximum entropy Doppler tomography code[2] developed by T. Marsh. We computed the Doppler tomogram for the strongest Bowen narrow component, N III 4640.64/4641.84 Å using the ephemeris from MS2017 and also their systemic velocity ($\gamma = 104 \pm 3$ km s^{-1}). We present the resulting Doppler map in Fig. 3, where a compact spot along the positive V_y is clearly detected. We computed the position of this spot via 2D-Gaussian fitting and found $V_x \sim -39$ km s^{-1}, $V_y \sim 94$ km s^{-1}. This corresponds to a phase shift of $\Delta\phi \sim -0.06$, which is compatible with the irradiated donor star (see Fig. 3; the angular size of the donor is $\sim$0.1 in phase, while the absolute error in the orbital phase is only $\sim$0.01). We also detected a bright extended region, which is consistent with the gas-stream trajectory and/or the region where the infalling material impacts the outer edge of the disc (i.e. the hotspot).

In a second step, we used bootstrap techniques to compute confidence intervals for the above results. To this end, we model a data set of 2000 bootstrapped maps from the original data (see Wang et al. 2017). We computed the peak height and $K_{\rm em}$ via a 2-D Gaussian fit to each bootstraped map. Subsequently, histograms of both parameters were constructed. Since these bootstrap distributions were roughly Gaussian, we estimated the mean and the 1σ error for each parameter via Gaussian fitting (Fig. 4). We found $K_{\rm em} = 102 \pm 6$ km s^{-1}. Additionally, we estimated the significance of the spot to be $\gtrsim 13\sigma$.

[2] This code is available at https://github.com/trmrsh/trm-doppler, see DOCS/FEATURES.RST for its notable features.

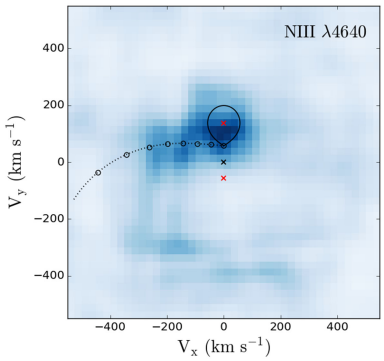

Figure 3. The Doppler tomogram of N III 4640.64/4641.84 Å computed using the updated binary period, ephemeris and $\gamma = 104\,\mathrm{km\,s^{-1}}$ from MS2017. The origin (denoted by a black cross) corresponds to the centre of mass of the system. We overplot the gas-stream trajectory and the Roche lobe of the companion assuming $K_2 = 136\,\mathrm{km\ s^{-1}}$ and a mass ratio of 0.41. The true orbital velocities of the companion (0, $K_2 = 136\,\mathrm{km\ s^{-1}}$) and the neutron star (0, $-\mathrm{K_1} = -56\,\mathrm{km\ s^{-1}}$) are denoted by red crosses.

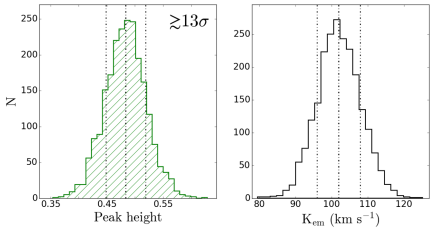

Figure 4. Distributions of the relative peak height (left) and K_{em} (right) determined from 2000 bootstrapped maps iterated to reach the same image entropy ($S = -0.04$) as that of the original image (Fig. 3). Dashed lines indicate the mean and the $\pm 1\sigma$ confidence intervals. The emission feature is significant at the $\gtrsim 13\sigma$ level, providing a radial velocity semi-amplitude of $K_{em} = 102 \pm 6\,\mathrm{km\ s^{-1}}$.

3.3 Opening angle of the accretion disc

The K_{em} and K_2 projected radial velocities can be related using K_c ($=K_{em}/K_2$) from MD2005. This correction mainly depends on the mass ratio (q) and the opening angle of the accretion disc (α), which partially shadows the companion star, preventing the closest regions to the inner Lagrangian point from being irradiated. Given that K_{em}, K_2 and q are constrained, we carried out a Monte Carlo analysis to determine the range of accretion disc opening angles compatible with the observables. We proceeded as follows:

(i) We sampled K_{em} and K_2 by using Gaussian distributions from the values reported in Table 2. We created a synthetic distribution of $K_c = K_{em}/K_2$, that is, we obtained a K_c value for each combination of the two observables.

Table 2. Observed values.

Parameter	Value
K_{em}	$102 \pm 6\,\mathrm{km\,s^{-1}}$
K_2	$136 \pm 4\,\mathrm{km\,s^{-1}}$ *
q	0.41 ± 0.08*
i	36°–47° *

Note. *Mata Sánchez et al. (2017).

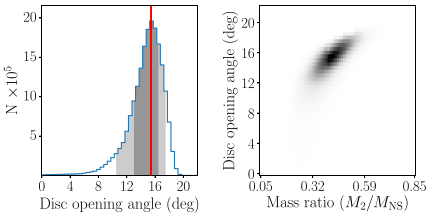

Figure 5. Probability density functions obtained from the Monte Carlo analysis method with 8×10^7 trials. The red line indicates the position of the 50th percentile. The 90 per cent and 68 per cent confidence regions are shown as dark and light shaded areas respectively.

(ii) We produced synthetic K_c values from MD2005. These can be approximated by fourth-order polynomials on q using the form:

$$K_c \simeq N_0 + N_1 q + N_2 q^2 + N_3 q^3 + N_4 q^4, \quad (1)$$

where $N_0 ... N_4$ are tabulated as a function of α for high and low inclination systems (90 and 40 deg, respectively). Based on MS2017, we considered the low inclination case.

(iii) Using the value reported in Table 2, we adopted a Gaussian distribution for q. This distribution was sampled from 0.05 to 0.85 in steps of 0.01; likewise, α was sampled from 0 to 22 deg in steps of 0.5 deg. For those α values not tabulated in MD2005, we performed a second-order polynomial interpolation using the K_c corresponding to the three nearest tabulated values, keeping the correction accurate to $\lesssim$2 per cent.

(iv) We produced the probability density function of α by comparing each K_c Monte Carlo trial with the synthetic values for a given q and within the α boundaries given by the Paczyński approximation [i.e. $0 < \alpha < \alpha_M$; where $\sin \alpha_M \cong 0.462(q/1+q)^{1/3}$ Paczyński (1971)]. The projected 1D probability density function of the disc opening angle was obtained using 8×10^7 Monte Carlo trials and then marginalized over q (Fig. 5). Considering 90 per cent confidence levels, we obtained $\alpha = 15.5\,^{+2.5}_{-5}$ deg.

4 DISCUSSION

We have presented results from a detailed optical spectroscopic campaign of the neutron star transient Aql X-1 obtained during three different outbursts. The analysis is focused on the Bowen blend spectral region and, in particular, we present a Doppler map of the N III 4640.64/4641.84 Å emission line, which shows a highly significant spot at the expected Doppler coordinates of the donor star. The K_{em} derived from this map is fully compatible with the true K_2 velocity reported in MS2017. The Gaussian-fitting technique, on the other hand, yields very complex results, which are in many cases inconsistent with a companion star origin. We interpret this as being the result of additional components that we are not able

to fully resolve and appear blended with the emission arising from the irradiated side of the donor. In addition, the largely differing Bowen blend profiles observed over the observing campaign (Fig. 1 top) shows that the relative contribution of the different emission regions contributing to the Bowen blend change with time.

The K_{em} proposed in Cornelisse et al. (2007) using the Bowen technique is ruled out by the K_2 velocity reported in MS2017. The spectral resolution of the former work is $\sim$100 km s^{-1} (i.e. significantly better than 130–170 km s^{-1} used in this work), but the data covered only a limited orbital phase range ($\sim$0–0.3) with all the spectra taken over three consecutive nights. Indeed, our re-analysis of the VLT data (which includes the new ephemeris; Fig 2) shows that none of the velocity measurement from this data set were compatible with a donor star origin. Therefore, at least for the particular epoch and orbital phases covered by the VLT 2004 observations, the Bowen blend narrow emission was not dominated by the companion star contribution. These results together with the recently reported study of the black hole transient GX 339-4 (Heida et al. 2017) demonstrate that complete phase coverage is a mandatory requirement in order to be able to confidently apply the Bowen technique. A complete phase coverage also allows the application of more robust analysis techniques, such as Doppler tomography, which enables us to be able to disentangle the different emission regions and single out the companion star contribution. In this particular case, different emission regions are resolved in velocity space, including a very significant companion star contribution ($\gtrsim 13\sigma$). Misidentification effects were minimized due to the amount and time distribution of the data, as we used 65 spectra taken over 3 different outbursts at different orbital phases. We obtained $K_{em} = 102 \pm 6$ km s^{-1}, which implies $K_c \sim 0.75$. This result is in the expected range, as computed by MD2005. Using the constraints to the orbital inclination and the mass ratio provided in MS2017, we ran Monte Carlo simulations to determine the opening angle of the accretion disc, $\alpha = 15.5^{+2.5}_{-5}$ deg, where errors are given at 90 per cent significance level. We note that this value is, in principle, independent of any assumed disc geometry, as it just represents the angle subtended by the largest vertical structure of the accretion disc. It can be easily interpreted as the angle subtended by the outer disc rim but also as that related to a more complex structure (e.g. a inner disk torus; Corral-Santana et al. 2013).

Several works have attempted to constrain the accretion disc opening angle by modelling optical fluxes and light curves (from photometric data). Considering a simple geometric model for X-ray reprocessing on LMXBs and comparing the absolute visual magnitude with the amplitude of the outburst light curve, de Jong, van Paradijs & Augusteijn (1996) proposed an average value of $\alpha \sim 12$ deg. Likewise, Gerend & Boynton (1976) obtained $\alpha \sim 10$ deg for Hercules X-1 whilst Motch et al. (1987) estimated $\alpha \sim 9$–13 deg for XB 1254-690. On purely theoretical grounds, Meyer & Meyer-Hofmeister (1982) studied the role of X-ray heating on the vertical structure of the accretion disc and showed that X-ray radiation is expected to thicken the accretion disc significantly. They obtained $\alpha \sim 6$ deg using models with no X-ray heating, while a thicker disc with $\alpha \sim$18–22 deg was determined when X-ray irradiation was taken in account. However, the latter value is probably overestimated as the disc is assumed to absorb every X-ray photon (see also de Jong et al. 1996).

In this paper, we have presented the first solid determination of the accretion disc opening angle through a (relatively direct) spectroscopic method. It directly compares day-side and centre of mass velocities to infer the size of the accretion structure that shadows the donor. Even though we have carried out an accurate study (including detailed error analysis), the reader must bear in mind that the value presented here depends on the *K*-correction modelling (i.e. MD2005) and therefore is likely subject to systematic effects. Nevertheless, our results are clearly consistent with an irradiation-driven thick accretion disc, providing strong support for the aforementioned theoretical works. Values lower than $\sim$10 deg seem very difficult to reconcile with our results, while the upper limit is roughly consistent with the maximum disc opening angle for the donor to be irradiated at all (whose value depends on q); see Section 3.3. Indeed, opening angles close to this limit might explain the complex and very variable evolution of the Aql X-1 Bowen blend narrow components. On one hand, emission from the donor would be weak in this case and, on the other hand, variable X-ray irradiation could produce small changes in the vertical structure of the disc, which might, in some cases, go beyond the previous limit, preventing the donor from being irradiated. In light of this, we searched for trends relating the strength/presence of narrow emission lines with the X-ray flux measured by the *MAXI* monitor (Fig. 1) and found no conclusive evidence.

Finally, we remark that our results are valid for the outburst state, as thinner accretion discs are expected in quiescence (see above). To test this scenario, we carried out the Monte Carlo analysis presented here using literature data from the neutron star transient Centaurus X-4. We considered $K_{em} = 122.8 \pm 11.8$ km s^{-1} (obtained from a Doppler map of the He I 5876 Å emission line while the source was in quiescence; D'Avanzo et al. 2005), $K_2 = 144.6 \pm 0.3$ km s^{-1} and $q = 0.20 \pm 0.03$ (from Casares et al. 2007). We obtained $\alpha = 12.5^{+2.5}_{-6.5}$ deg (errors are given at 90 per cent), which is consistent with 7 deg $\leq \alpha \leq$ 14 deg determined by D'Avanzo et al. (2006) by directly using the 1σ limits to the radial velocity curves and mass ratio (we note that our 68 per cent constraint is $\alpha = 12.5^{+1.5}_{-3}$) deg. Therefore, even if this measurement allows for smaller accretion disc opening angles, it is not significantly different from the outburst value presented here.

5 CONCLUSIONS

We have presented time-resolved spectroscopy of Aql X-1 in outburst with an unprecedented orbital phase coverage. We resolved Bowen blend narrow components and proved that the Bowen technique is able to trace the orbital motion of the companion star when ample phase coverage is available. We used new generation Doppler mapping to determine K_{em} from N III 4640.64/4641.84 Å emission line. This, together with K_2 and q values from near-infrared spectroscopy, allowed us to directly measure the elusive accretion disc opening angle in outburst ($\alpha = 15.5^{+2.5}_{-5}$ deg), the large value of which is in agreement with accretion disc models that take into account X-ray irradiation.

ACKNOWLEDGEMENTS

We are thankful to the anonymous referee for providing useful comments that improved the manuscript. Based on data from the GTC Public Archive at CAB (INTA-CSIC), developed in the framework of the Spanish Virtual Observatory project supported by the Spanish MINECO through grants AYA 2011-24052 and AYA2014-55216. The system is maintained by the Data Archive Unit of the CAB (INTA-CSIC). DMS acknowledges Fundación La Caixa for the financial support received in the form of a PhD contract. TMD is supported by RYC-2015-18148. MOLLY software developed by T. R. Marsh is gratefully acknowledged.

REFERENCES

Belloni T. M., Motta S. E., Muñoz-Darias T., 2011, Bull. Astron. Soc. India, 39, 409
Casares J., Jonker P. G., 2014, Space Sci. Rev., 183, 223
Casares J., Cornelisse R., Steeghs D., Charles P. A., Hynes R. I., O'Brien K., Strohmayer T. E., 2006, MNRAS, 373, 1235
Casares J., Bonifacio P., González Hernández J. I., Molaro P., Zoccali M., 2007, A&A, 470, 1033
Charles P. A., Coe M. J., 2006, in Lewin W. H. G., van der Klis M., eds, Cambridge Astrophysics Series No. 39, Compact Stellar X-ray Sources. Cambridge Univ. Press, Cambridge, p. 215
Cornelisse R., Casares J., Steeghs D., Barnes A. D., Charles P. A., Hynes R. I., O'Brien K., 2007, MNRAS, 375, 1463
Cornelisse R., Casares J., Muñoz-Darias T., Steeghs D., Charles P., Hynes R., O'Brien K., Barnes A., 2008, in Bandyopadhyay R. M., Wachter S., Gelino D., Gelino C. R., eds, AIP Conf. Ser. Vol. 1010, A Population Explosion: The Nature & Evolution of X-ray Binaries in Diverse Environments. Am. Inst. Phys., New York, p. 148
Corral-Santana J. M., Casares J., Muñoz-Darias T., Rodríguez-Gil P., Shahbaz T., Torres M. A. P., Zurita C., Tyndall A. A., 2013, Science, 339, 1048
Coti Zelati F., Campana S., D'Avanzo P., Melandri A., 2014, MNRAS, 438, 2634
D'Avanzo P., Campana S., Casares J., Israel G. L., Covino S., Charles P. A., Stella L., 2005, A&A, 444, 905
D'Avanzo P., Muñoz-Darias T., Casares J., Martínez-Pais I. G., Campana S., 2006, A&A, 460, 257
de Jong J. A., van Paradijs J., Augusteijn T., 1996, A&A, 314, 484
Fender R., Muñoz-Darias T., 2016, in Haardt F., Gorini V., Moschella U., Treves A., Colpi M., eds, Lecture Notes in Physics, Vol. 905, Astrophysical Black Holes, Springer-Verlag, Berlin, p. 65
Friedman H., Byram E. T., Chubb T. A., 1967, Science, 156, 374
Gerend D., Boynton P. E., 1976, ApJ, 209, 562
Heida M., Jonker P. G., Torres M. A. P., Chiavassa A., 2017, ApJ, 846, 132
Hynes R. I., Steeghs D., Casares J., Charles P. A., O'Brien K., 2003, ApJ, 583, L95
Hynes R. I., Charles P. A., van Zyl L., Barnes A., Steeghs D., O'Brien K., Casares J., 2004, MNRAS, 348, 100
Marsh T. R., Horne K., 1988, MNRAS, 235, 269
Mata Sánchez D., Muñoz-Darias T., Casares J., Steeghs D., Ramos Almeida C., Acosta Pulido J. A., 2015a, MNRAS, 449, L1
Mata Sánchez D., Muñoz-Darias T., Casares J., Corral-Santana J. M., Shahbaz T., 2015b, MNRAS, 454, 2199
Mata Sánchez D., Muñoz-Darias T., Casares J., Jiménez-Ibarra F., 2017, MNRAS, 464, L41 (MS2017)
Meyer F., Meyer-Hofmeister E., 1982, A&A, 106, 34
Miller-Jones J. C. A. et al., 2010, ApJ, 716, L109
Motch C., Pedersen H., Courvoisier T. J.-L., Beuermann K., Pakull M. W., 1987, ApJ, 313, 792
Muñoz-Darias T., 2009, PASP, 121, 935
Muñoz-Darias T., Casares J., Martínez-Pais I. G., 2005, ApJ, 635, 502
Muñoz-Darias T., Martínez-Pais I. G., Casares J., Dhillon V. S., Marsh T. R., Cornelisse R., Steeghs D., Charles P. A., 2007, MNRAS, 379, 1637
Muñoz-Darias T., Fender R. P., Motta S. E., Belloni T. M., 2014, MNRAS, 443, 3270
Paczyński B., 1971, ARA&A, 9, 183
Steeghs D., Casares J., 2002, ApJ, 568, 273
van der Klis M., 2006, Adv. Space Res., 38, 2675
van Dokkum P. G., 2001, PASP, 113, 1420
Wang L., Steeghs D., Casares J., Charles P. A., Muñoz-Darias T., Marsh T. R., Hynes R. I., O'Brien K., 2017, MNRAS, 466, 2261

This paper has been typeset from a TEX/LATEX file prepared by the author.

4

An equatorial outflow in the black hole optical dipper Swift J1357.2–0933

Golden slumbers fill your eyes
smiles await you when you rise

Golden slumbers, Lennon-McCartney

Swift J1357.2–0933 is a transient LMXB with one of the most massive BHs ($M_1 > 9.3\,M_\odot$; Mata Sánchez et al., 2015). Discovered during an outburst in 2011 (Krimm et al., 2011), it is one of the shortest orbital period systems known to date (about 2.8 hours) and exhibits the broadest Hα emission profile amongst all the BH transients (Corral-Santana et al., 2013). However, what drawn the most attention was the discovery of quasi-periodic optical dips during the decay of the outburst. The dips recurrence period (of the order of minutes) was observed to be much shorter than the binary period, and it was shown to increase as the outburst declined (Corral-Santana et al., 2013). The same authors explained the dip properties as produced by obscuring material moving outward in the inner disc, seen at very high inclination. Such quasi-periodic dips had never been seen before in any other system. These features were observed again in the following two outbursts of Swift J1357.2–0933 in 2017 and 2019 (e.g. Paice et al., 2019; Jimenez-Ibarra et al., 2019, respectively).

In this chapter (published as a paper in Monthly Notices of the Royal Astronomical Society, 2019, 489, 3420), we describe an optical photometry and spectroscopy observing campaign on Swift J1357.2–0933 during its 2017 outburst. We achieved high time resolution (in the range of 22–37 s) spectroscopy using the 10.4-m Gran Telescopio Canarias. Thus, we time-resolved the optical dips and demonstrated the outflowing nature of the material producing these features.

Monthly Notices of the ROYAL ASTRONOMICAL SOCIETY
MNRAS **489,** 3420–3426 (2019) doi:10.1093/mnras/stz2393
Advance Access publication 2019 August 29

An equatorial outflow in the black hole optical dipper *Swift* J1357.2−0933

F. Jiménez-Ibarra [1,2]★ T. Muñoz-Darias [1,2] J. Casares [1,2] M. Armas Padilla [1,2] and J. M. Corral-Santana [3]

[1] *Instituto de Astrofísica de Canarias, Vía Láctea, La Laguna, E-38205 Santa Cruz de Tenerife, Spain*
[2] *Departamento de Astrofísica, Universidad de La Laguna, E-38206 Santa Cruz de Tenerife, Spain*
[3] *European Southern Observatory (ESO), Alonso de Córdova 3107, Vitacura, Casilla 19001, Santiago, Chile*

Accepted 2019 August 26. Received 2019 August 16; in original form 2019 June 6

ABSTRACT

We present high time resolution optical spectroscopy and imaging of the black hole transient *Swift* J1357.2−0933 during its 2017 outburst. The light curves show recurrent dips resembling those discovered during the 2011 outburst. The dip properties (e.g. duration and depth) as well as the evolution of their recurrence time are similar to those seen in 2011. Spectra obtained during the dips are characterized by broad and blueshifted absorptions in Balmer and He II. The absorptions show core velocities of ∼−800 km s^{-1} and terminal velocities approaching ∼3000 km s^{-1} i.e. in the upper end of wind velocities measured in other black hole transients (both at optical and X-ray wavelengths). Our observations suggest that the dips are formed in a dense and clumpy outflow, produced near the disc equatorial plane and seen at high inclination. We also study the colour evolution and observe that, as it has been previously reported, the source turns bluer during dips. We show that this is due to a gradual change in the slope of the optical continuum and discuss possible implications of this behaviour.

Key words: accretion, accretion discs – stars: black holes – X-rays: binaries.

1 INTRODUCTION

Accretion is the governing mechanism in a large number of astrophysical contexts from planetary formation to active galactic nuclei. In the case of black hole X-ray binaries (i.e. interacting binaries where a companion star transfer matter on to a black hole) accretion results in the most efficient mechanism of converting matter into energy. In these systems accretion proceeds via an accretion disc. The high temperature reached in this disc (∼10^7 K) makes them luminous X-ray sources, that also radiate at lower energies, mainly due to thermal reprocessing of the X-ray photons in different binary regions. Accretion in X-ray binaries exhibit timing properties accessible to human time-scales, showing variability ranging from sub-seconds to months (see Remillard & McClintock 2006; van der Klis 2006; Belloni, Motta & Muñoz-Darias 2011, for reviews).

Among black hole X-ray binaries, transient systems (BHTs), alternate long periods of faint quiescence with bright and short (weeks to months) outbursts. These episodes are triggered by a sudden increase of mass accretion on to the black hole and reach luminosities typically above ∼10 per cent of the Eddington limit. A wide variety of outflowing phenomenology is also common to BHTs. This consists of collimated radio jets and both, low and highly ionized winds. In general, the properties of the outflows have been found to be strongly coupled to those of the accretion flow (see e.g. Corbel et al. 2003; Gallo, Fender & Pooley 2003; Fender & Muñoz-Darias 2016; Ponti et al. 2016; Muñoz-Darias et al. 2019).

Swift J1357.2−0933 is a BHT discovered during an outburst episode in 2011 (Krimm et al. 2011; Armas Padilla et al. 2013). Its orbital period is among the shortest of its class (∼2.8 h) and it exhibits the broadest disc emission lines among BHTs, a strong indication for a high binary inclination (Corral-Santana et al. 2013, hereafter CS13). A black hole mass > 9.3 M$_\odot$ has been inferred by applying empirical scaling relations to the full width at half-maximum (FWHM) of the Hα line (Mata Sánchez et al. 2015, hereafter MS15; Casares 2016).

During the decay of its 2011 outburst CS13 observed regular dips in the optical light curve. The dips were profound (up to ∼0.8 mag depth, with characteristic durations of ∼2 min) and recurred with increasing quasi-periodicity as the outburst declined. These features were interpreted as caused by obscuration of inner disc regions by a vertical structure that moved outwards as the outburst proceeded (CS13, MS15). The nature of the obscuring structure remains unclear and has been the subject of much debate (Armas Padilla et al. 2014; Torres et al. 2015; Beri et al. 2019).

In 2017, the system went into another outburst (Drake et al. 2017) and new optical dips, evolving in a similar way as those reported in 2011, were observed again (Paice et al. 2019). In order to investigate the puzzling nature of the dips we used the 10.4 m Gran Telescopio Canarias (GTC) and obtained high time resolution spectroscopy through the dips for the first time.

★ E-mail: felipeji@iac.es

2 OBSERVATIONS AND DATA REDUCTION

2.1 Optical spectroscopy

We carried out optical spectroscopy of *Swift* J1357.2−0933 over 3 nights during the 2017 outburst, using the Optical System for Imaging and low-Intermediate Resolution Integrated Spectroscopy (OSIRIS; Cepa et al. 2000) mounted on the 10.4 m GTC at the Observatorio del Roque de los Muchachos (ORM; La Palma, Spain). On 2017 May 4, we obtained two exposures of 400 s each using the R1000B optical grism in the spectral range 3630–7500 Å. Combined with a slit width of 1 arcsec this yields a velocity resolution of ∼350 km s^{-1}, as measured from the FWHM of the O I airglow line at ∼5577 Å. In addition, we obtained fast timing spectroscopy with the R300B grism on the nights of 2017 June 12 and 16 in order to resolve the optical dips. For this purpose, we used individual exposure times of ∼13 s which, together with overheads, resulted in time resolutions in the range of 22–37 s. We collected a total of 304 spectra (165 on June 12 and 139 on June 16), covering the spectral range 3600–7200 Å. We employed two slit widths of 1 and 0.6 arcsec for the nights of June 12 and 16. This set-up provided spectral resolutions ranging from 590 to 970 km s^{-1} (determined using sky lines). We note that the seeing was in the range of ∼1–1.5 arcsec and ∼0.7–1.3 arcsec during the first and second epoch, respectively, and therefore the spectral resolution was always limited by the slit width. We applied bias and flat-fielding corrections using IRAF standard routines, while cosmic rays were removed with L.A.COSMIC (van Dokkum 2001). The pixel-to-wavelength calibration was handled using arc lamp exposures taken on each observing night (HgAr + Ne lamps for the R1000B grism and HgAr + Ne + Xe for the R300B). All the spectra were corrected for velocity drifts introduced by instrumental flexure (<110 km s^{-1}) using MOLLY software and the O I ∼5577 Å sky emission line.

The slit was oriented to include a nearby star, which was used to monitor and correct for possible slit losses caused by variable seeing conditions. This was done through scaling the spectrum of *Swift* J1357.2−0933 to that of the on-slit star in each spectrum. In order to obtain absolute flux, we calibrated the best on-slit star spectrum of the series (i.e. the one obtained under the best conditions) against the flux standard GD 153 (Bohlin, Colina & Finley 1995), which was observed the same night but using a wider slit (2.52 arcsec). To account for the different slit width between the on-slit star and GD 153, we refine the flux calibration of the former by using Sloan *g*-band photometry obtained from the acquisition image. This was achieved through synthetic photometry obtained by convolving the spectrum of the on-slit star with the Sloan *g*-filter bandpass. Finally, the calibrated spectrum of the on-slit star was used to extend the absolute flux calibration to every scaled spectra of *Swift* J1357.2−0933. We note that even if the absolute fluxes values might be affected by a small systematic offset, the relative fluxes between the different spectra should be highly accurate.

2.2 Optical photometry

We also used the Rapid Imager for Surveys of Exoplanets (RISE) fast-readout camera attached to the 2 m Liverpool Telescope (LT, at the ORM) to obtain high time resolution photometry of *Swift* J1357.2−0933. Observations were performed on seven different nights between 2017 May 15 and July 14, using the OG515 and KG3 filters (∼V + R band). The light curve on the night of 2017 June 12 is strictly simultaneous with the GTC spectroscopy. The fast readout time of RISE (∼0.04 s) minimized the overhead between exposures, resulting in time resolutions near the exposure time (∼5 s). The data reduction was completed using the data reduction pipeline for the optical imaging component of the infrared-optical suite.[1] Flux calibration was performed against field stars catalogued in PanSTARRS and using ASTROPY-PHOTUTILS based routines (Bradley et al. 2019) in the PanSTARRS-1 broad-band filter *r*.

3 ANALYSIS

3.1 Optical dips

Fig. 1 (top left panels) presents the seven LT light curves. We observe numerous dip events lasting typically ∼2 min, similar to those witnessed in the 2011 outburst by CS13. The dips are up to ∼0.5 mag deep. In addition, we produced two light curves (one per epoch) from the continuum of the high time resolution GTC spectra. To this end, we integrated the flux density within two apertures defined in featureless spectral regions (see Fig. 2, top panel). The GTC continuum light curves are shown in the middle panel of Fig. 2.

In order to explore the timing properties of the dips we produced Lomb–Scargle periodograms of the nine light curves using the LOMB–SCARGLE PYTHON class (VanderPlas 2018). The periodograms of the seven LT epochs are shown in the right-hand panel of Fig. 1. The highest peak reveals a dip recurrence period (DRP) that increases from 2.09 to 5.41 min over 59 d (see Table 1). Note that the DRP concurrently measured from the LT and GTC light curves on 2017 June 12 are consistent within errors.

The evolution of the frequency (from DRP) as a function of time, together with the best parabolic fit, are shown in red in Fig. 1 (bottom panel). In the same panel, green points represent the data and best fit from CS13 (2011 outburst). In order to compare the evolution of the two frequency tracks, a time shift was applied to the 2011 data. This was obtained by matching the frequency of the first 2011 point to the interpolation of the 2017 frequency curve. A visual comparison reveals a remarkable analogy in both evolutions. The similarity in both dip properties and DRP evolution strongly suggests that the phenomenon producing the dips in 2017 is the same as in 2011.

3.2 Spectral analysis

In Fig. 2 (top panel) we present the averaged spectrum of *Swift* J1357.2−0933 obtained on 2017 May 4 with the R1000B grism. We identify broad emission lines corresponding to the Balmer series (up to Hγ), He I-5876 Å, and He II (4686 and 5411 Å). All the lines display double-peaked profiles, with the exception of He I-5876 Å, where the red edge is affected by the Na I-doublet interstellar absorption at 5890–5896 Å. The emission lines are all remarkably broad (Hα FWHM ∼ 3000 km s^{-1}), similarly to what was seen during the 2011 outburst (Hα FWHM ∼ 3300 km s^{-1}, CS13). We determined the centroid velocity of the Hα line by fitting a two-Gaussian model (to account for the double-peaked profile) over the R1000B normalised spectrum. We obtained -130 ± 17 km s^{-1}, which is consistent with the systemic velocity (γ) measured in the previous outburst ($\gamma \sim -150$ km s^{-1}, CS13). On the other hand, we obtain different velocities from the R300B spectra, ∼−300 km s^{-1} on June 12 and 0 km s^{-1} on June 16. Variations in the centroid velocity of the Hα line have been observed before and interpreted as signatures of a precessing accretion disc (MS15).

[1] http://telescope.livjm.ac.uk/TelInst/Pipelines/#ioo

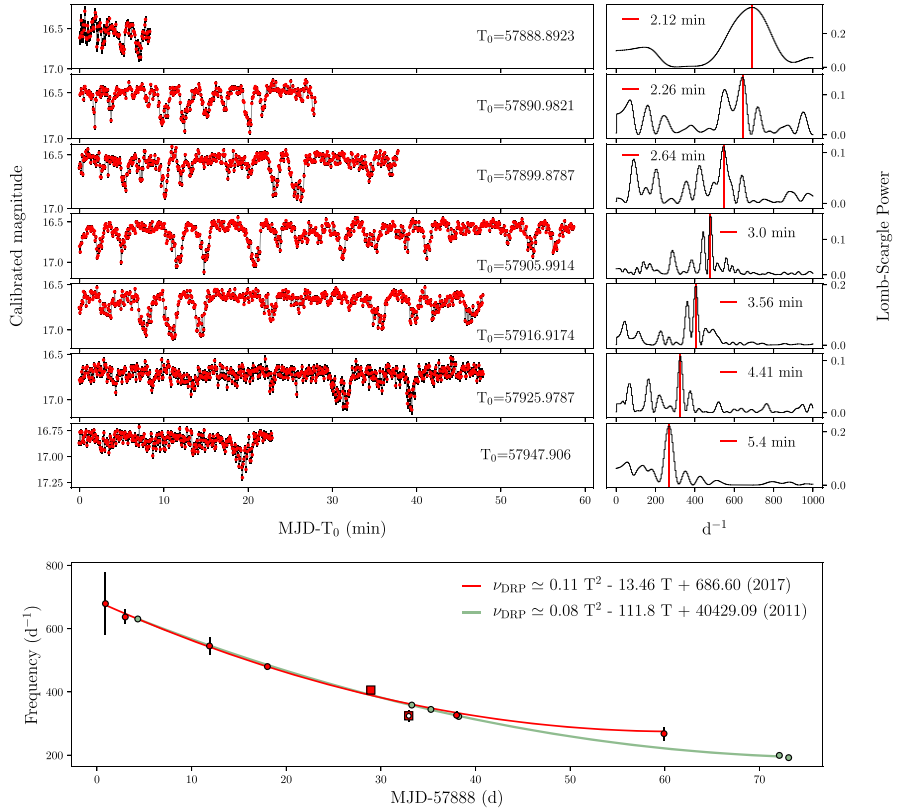

Figure 1. Top panels: optical light curves of *Swift* J1357.2−0933 (left) and their corresponding power density spectra obtained from the Lomb–Scargle analysis (right). The frequency of the highest peak is indicated by a red vertical line. Bottom panel: time evolution of the DRP frequency. The solid lines indicate the best parabolic fits to the data points. Our data are indicated in red, while data from CS13 are shown in green. The 2011 curve has been shifted in time by matching the first point of the series to the interpolation of the 2017 parabolic fit. Red squares indicate the frequencies obtained from the GTC continuum light curves. The empty square indicates the frequency concurrently measured from the LT data and the GTC continuum light curve.

Based on the continuum light curve (see Section 3.1), we define two groups of spectra that we call *dip* and *non-dip* spectra hereafter. In order to select them we have computed the mean and the standard deviation (σ) of the continuum light curve using a sigma clipping algorithm (ASTROPY.STATS; Astropy Collaboration 2013). Points above the mean are considered non-dip spectra, while points below the mean level are labelled as dip spectra. We have also divided dip spectra into three further groups separated by the 3σ and the 6σ levels (see Fig. 2, middle panel). We subsequently combined the selected spectra to produce four averaged spectra per night (three dip and one non-dip). The resulting spectra are shown in Fig. 2 (bottom panel).

The non-dip averaged spectra show double-peaked Hα profiles. Conversely, the Hβ and He transitions are less evident, appearing as single-peaked lines, likely because of the lower signal to noise. We note that the Hα line weakens by a factor $\sim$2 as the outburst evolves, from EW $\sim$4 to $\sim$2 Å between May 4 and June 16, respectively (see Table 2).

The dip averaged spectra reveal the presence of broad absorption components in Balmer and He II that strengthen as the flux drops. Interestingly, no absorption is detected in He I-5876 Å that keeps the same emission profile in both the dip and non-dip spectra. The Balmer and He II absorption minima reach 10 per cent below the continuum level (see Fig 2) and are all blueshifted.

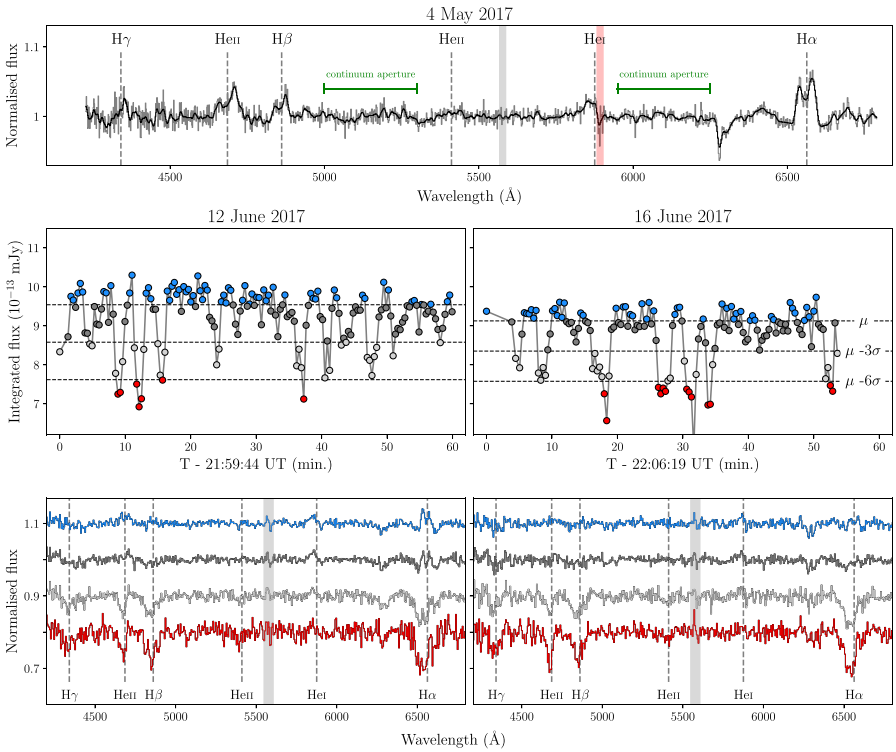

Figure 2. Top panel: continuum normalised spectrum of *Swift* J1357.2−0933 obtained on 2017 May 4. A Gaussian smoothed version is overplotted in black. The identified emission lines are indicated by dashed lines. The red shaded line indicates the Na I-doublet at 5890–5896 Å. The continuum regions defined for the light curve extraction are indicated by green segments. Middle panel: continuum light curves extracted from the high time resolution spectra. Coloured dots indicate non-dip spectra (blue) and three levels of dip spectra (dark grey, light grey, and red). The horizontal dashed lines mark the limits defining each group as described in the text. Bottom panels: normalised dip, and non-dip spectra following the light curve colour code defined above. A vertical offsets of 0.1 has been added to the normalised spectra for clarity. The ∼5577 Å sky emission line region is indicated in all the spectra as a grey thick line.

Table 1. Time evolution of the DRP.

Date	MJD (d)	DRP (cycle d^{-1})	DRP (min)
2017-05-15	57888.8952156	679 ± 99	2.12 ± 0.31
2017-05-17	57890.9918298	637 ± 22	2.26 ± 0.08
2017-05-26	57899.8918105	545 ± 27	2.64 ± 0.13
2017-06-02	57906.0117608	480 ± 8	3.00 ± 0.05
2017-06-12	57916.9340031[a]	404 ± 11	3.56 ± 0.10
2017-06-12	57916.9376235	406 ± 9	3.55 ± 0.08
2017-06-16	57920.9410283[a]	324 ± 18	4.44 ± 0.25
2017-06-21	57925.9953267	326 ± 11	4.41 ± 0.15
2017-07-13	57947.913911	268 ± 21	5.4 ± 0.4

[a]Obtained from the GTC continuum light curve.

In order to measure the centroid of the profiles we fitted a multi-Gaussian model to the H α, H β, and He II absorption components in the deepest (continuum normalised) dip spectrum of each night. The height, the FWHM, and the velocity offset of each Gaussian were set as free parameters. Instrumental broadening was taken into account in the fitting process. We note that the H α absorption is affected by a narrow emission component (red wing) that was masked. The fits results are presented in Table 2. The FWHM of a given absorption also remains roughly consistent between the two epochs. The terminal velocities of the absorption profiles range from 1579 ± 180 to 4178 ± 222 km s^{-1} (velocity of the blue edge at 10 per cent of the depth of the fitted Gaussian) for He II-4686 Å and H β, respectively. On the other hand, the offset velocities obtained for the three lines are consistent with each other within 1.5σ. Thus, in a second step we tied the core velocities of the three Gaussians

Table 2. Properties of emission and absorption lines.

	FWHM (km s^{-1})	EW (Å)	Centroid velocity (km s^{-1})
Emission			
May 4, June 12 and 16			
Hα	2824 ± 92	3.95 ± 0.08	−131 ± 16
	3059 ± 142	3.53 ± 0.13	−313 ± 32
	3084 ± 281	2.17 ± 0.16	−12 ± 63
Absorption			
June 12 and 16			
Hα	4031 ± 399	−11.0 ± 0.6	−908 ± 227
	3310 ± 299	−10.0 ± 0.4	−982 ± 120
Hβ	4380 ± 444	−5.8 ± 0.4	−690 ± 177
	4585 ± 344	−4.4 ± 0.4	−739 ± 138
He II-4686 Å	1790 ± 446	−2.3 ± 0.4	−841 ± 158
	1733 ± 198	−3.3 ± 0.3	−725 ± 75

and performed a new fit. We derive velocity offsets of -840 ± 101 and -766 ± 59 km s^{-1} for the first and second epoch, respectively.

Finally, we have averaged the dip and the non-dip spectra of the two GTC nights and produced four final spectra, one for each defined class. The result is shown in Fig. 3 (top panel). The three average dip spectra were also divided by the average non-dip spectrum to produce three ratio spectra that are plotted in green in the same figure. These reflect the evolution of the dip spectra relative to the non-dip spectrum, further enhancing spectral features caused by the dip while quenching those that remain unchanged. For example, the He I-5876 Å line vanishes in the ratio spectra, while the blueshifted absorptions become clearer in Balmer and He II (see Fig. 3, middle panel). We also note a clear variation in the continuum slope of the ratio spectra. This reveals a progressive change in the colour of the spectrum through the dip, indicating that the spectrum becomes more absorbed at red than at blue wavelengths.

To further examine this property, we have produced light curves from red and blue windows of the original spectra. We used MOLLY software to integrate the flux density over two featureless spectral regions of width 200 Å: the blue region is centred at 5125 Å while the red one at 7075 Å (see Fig. 3, top panel). The blue and red light curves are presented in the bottom panels of Fig. 3 for the two nights. In order to compare them, the light curves have been normalised to the non-dip level. We find that the dips obtained from the red part of the spectrum are ∼10 per cent deeper than those obtained from the blue part in both nights. In other words, the dips make the source bluer, contrary to what would be expected for the case of absorption by dust, which would redden the spectrum. This is entirely consistent with the results of Paice et al. (2019) based on multiband high time resolution photometry.

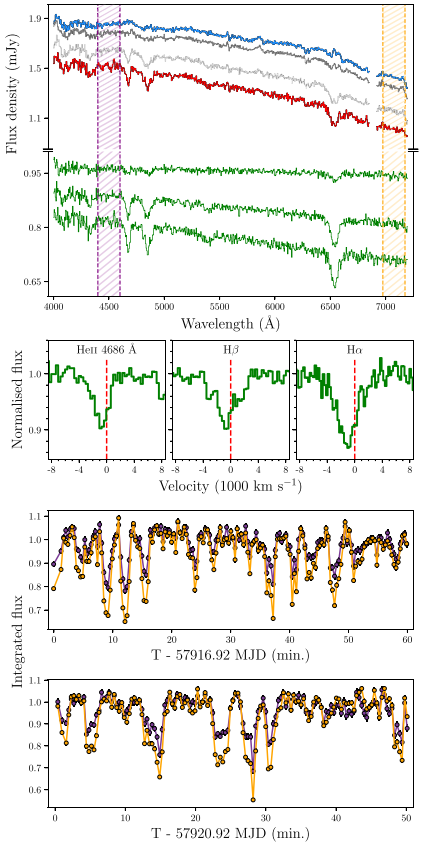

Figure 3. Top panel: dip (red) and non-dip (blue) averaged spectra of the two GTC nights. The green spectra show the result of dividing the three dip spectra by the non-dip spectrum. Middle panel: Hα, Hβ, and He II-4686 Å absorptions in the deepest (normalised) ratio spectrum and represented in their corresponding line rest frames. Bottom panels: June 12 (top) and June 16 (bottom) light curves obtained from red and blue continuum windows in the spectra (orange and purple points, respectively), normalised to the non-dip level. The regions defining these two spectral windows are indicated as shaded areas in the top panel, following the same colour code as above.

4 DISCUSSION

We have presented fast optical photometry and spectroscopy of *Swift* J1357.2−0933 during its 2017 outburst. Our data show evidence for optical dips in the nine light curves obtained. The dips are analogous to the ones discovered during the 2011 outburst, they are quasi-periodic and repeat with a recurrence period that migrates to lower frequencies as the outburst declines. In CS13 these dips are interpreted as due to obscuration by a vertical disc structure (seen at high inclination) that propagates outward as the outburst evolves. The similarities between the 2011 and 2017 dips are not only in shape but also in time evolution (see Section 3.1). The DRP follows the same cadence in both outbursts showing a similar frequency decay, which is remarkable for two phenomena occurring six years apart (see Fig. 1, bottom panel). This was also reported in Paice et al. (2019).

We have resolved the dips using high time resolution optical spectroscopy in two epochs. The dip spectra show broad absorptions in the Balmer and the He II lines while no absorption is observed in

He I-5876 Å (Fig. 2, lower panel). The absorptions become stronger as the flux drops within the dip and are conspicuous in spectra with a continuum level $\sim 3\sigma$ below the mean.

The absorption lines are blueshifted, with centroid velocities of ~ -800 km s^{-1}. Similar broad absorptions (sometimes with embedded emission) have been observed in other BHTs during outburst, e.g. GRO J0422+32, XTE J1118+480, and recently MAXI J1807+132 (Casares et al. 1995; Dubus et al. 2001; Jiménez-Ibarra et al. 2019, respectively) but evolving at longer time-scales (e.g. Jiménez-Ibarra et al. 2019, detected them in a 3600 s exposure spectrum). In these systems, the absorptions are strongest at blue wavelengths, and show velocities consistent with the rest frame of the system, in contrast with what we see in *Swift* J1357.2−0933.

In the last decade, accretion disc winds have been established as a common feature in BHTs. In X-rays, Ponti et al. (2012) used a sample of high inclination BHTs to measure blueshifted centroid velocities of ~ -1000 km s^{-1} in absorption features of highly ionized Fe among other species (see e.g. Miller et al. 2006; Neilsen & Lee 2009; Díaz Trigo & Boirin 2016, for similar studies). This is interpreted as the signature of hot equatorial winds. In the optical, P-Cygni profiles have been reported in V404 Cygni, V4641 Sgr, and MAXI J1820+070, demonstrating the presence of low-ionization winds with terminal velocities in the range of 1000–3000 km s^{-1} (Muñoz-Darias et al. 2016; Mata Sánchez et al. 2018; Muñoz-Darias, Torres & Garcia 2018; Muñoz-Darias et al. 2019). Thus, the terminal velocity that we measure in *Swift* J1357.2−0933 is consistent with the upper end of wind-type outflows observed in other BHTs.

While the observation of blueshifted Balmer absorptions in *Swift* J1357.2–0933 can be also interpreted as an equatorial wind, the simultaneous presence of He II absorptions possess a challenge. Hoare (1994) studied the He II transitions in non-magnetic cataclysmic variables and found that some components of He II-4686 Å originate in winds rather than in the disc. Furthermore, Drew (1990) demonstrated that clumpy winds in O stars can enhance the strength of the recombination lines. In particular, Sundqvist et al. (2011) showed that Hα reacts similarly to He II-4686 Å to clumping. Our observations might fit into this scenario. On one hand, the He II-4686 Å and H absorptions evolve quite similarly during the dip, reaching comparable depths within the same time-scale. They also share dynamical properties such as equal (1.5σ) core velocities. Altogether, this might suggest a common origin for the absorptions. However, the absorption is narrower in He II-4686 Å than in Balmer (see Table 2). This might be explained if they arise from slightly different regions of the ejecta, while the He I-5876 Å emission would be formed in a different disc region since it is not affected by the dips. On the other hand, clumping would also explain the observed complex structure of the optical light curve. Deep but short-lived dips with a sharp transition time-scale could be produced by dense inhomogeneities subtending a small angle over the line of sight. Within this context, the absorptions could be produced by optically thick and clumpy outflows.

If the winds are equatorial (as seen in Ponti et al. 2012), the outflowing direction is close to the line of sight which is in agreement with the high (projected) velocities measured. In addition, this perspective favours the observation of wind inhomogeneities (clumps) which would be optically thick since we are looking across large columns of gas.

Assuming that the mean terminal velocity observed ($\sim$3000 km s^{-1}) corresponds to the escape velocity at the launching radius we infer $R_{\rm l} \sim 0.17$ R$_\odot$. This assumption is expected to be roughly satisfied by some of the most popular wind launching mechanism (e.g. thermal winds, Begelman, McKee & Shields 1983). On the other hand, assuming that the DRP corresponds to the Keplerian frequency of a given disc annulus, the values measured on June 12 and 16 would correspond to Keplerian radii at $R_{\rm P} \sim 0.16$–0.18 R$_\odot$. The remarkable agreement reached from very different observables suggest that winds and dips are produced at the same radius. We propose two explanations for the dipping phenomenology in *Swift* J1357.2−0933, within the equatorial wind scheme. (i) The disc is warped by some mechanism that generates a vertical structure (CS13). Viewed at high inclination, this structure hides the inner disc, producing the dips. The gas in the vertical extend is exposed to irradiation and is expelled radially along the equatorial plane. (ii) Winds are triggered by some mechanism at a given radius, where the upper disc layers are expelled. The action of the winds therefore shapes the disc at a particular radius, producing dips in a high inclination perspective.

Our study reveals a colour-dependence behaviour of the dips. The red wavelengths are more obscured during the dip than the blue ones. This is at odds with expectations from standard dust scattering, since there is no standard dust extinction law that can explain this behaviour. In the extreme case, grey extinction (i.e. optically thick material at all the observed wavelengths) will produce a flat continuum with no change in the slope of the ratio spectra. The colour evolution of the dips is also evident after comparing synthetic light curves obtained from two continuum apertures in the red and blue part of the spectra (see Section 3.2). During the dip, the red light curve always reaches levels $\sim$10 per cent lower than the blue light curve. Qualitatively, the deeper the dip, the larger the contrast with its blue counterpart. Paice et al. (2019) put forward a scenario to explain the observed bluing of the source during the dip. The occultation of the lower (and brighter) part of the jet by the dipping structure would prevent the red component from contributing to the total spectral energy distribution, producing bluer spectra. In this framework, if we assume that only the red component is absorbed, the subtraction of the dip from the non-dip spectrum would yield the absorbed component, multiplied by a function of the extinction law. By doing this, we obtained four residual spectra adopting four common Milky Way dust extinction models. We used the functions contained in the package ASTROPY-DUST EXTINCTION (CCM89, O94, F99, and F04 from Cardelli, Clayton & Mathis 1989; O'Donnell 1994; Fitzpatrick 1999, 2004, respectively). We used the standard value $R_{\rm V} = 3.1$ and considered $A_{\rm V} = 0.3$ mag (average magnitude drop during dips; see Fig. 1). The continuum of the residual spectra are well described by a power law ($F_\nu \propto \nu^\alpha$) with $-1.6 < \alpha < -1.4$. All considered, this result is not far from predictions for jet emission in the optically thin regime ($-1 < \alpha < -0.4$; Blandford & Königl 1979), and is consistent with the spectral index measured in this system during quiescence by Shahbaz et al. (2013), using near-IR-optical data ($\alpha = -1.4 \pm 0.1$).

However, it is important to bear in mind that the above scenario assumes that the optical dips observed in the continuum are created by dust scattering, while we also observe absorption lines indicating the presence of outflowing, ionized gas. To start with, it is not clear how dust can be present in the hot environment surrounding BHTs.[2] Furthermore, our observations show that the behaviour of the continuum is clearly correlated with that of the absorption lines. A simpler alternative scenario would be that the continuum is absorbed by the same ionized gas producing the absorption lines via bound-free interactions, similar to those present in stellar atmospheres at

[2]However, we note that dust has been recently found in a quintuplet of Wolf–Rayet stars (Najarro et al. 2017).

temperatures low enough to allow the formation of recombination lines of hydrogen and helium. Interestingly, the effective cross-section of this interaction (for hydrogen) in the optical range increases with wavelength (e.g. Gray 2005), which could naturally explain the blue colour observed during the dips. Nevertheless, we note that a more detailed radiative modelling beyond the scope of this work would be necessary to support this latter scenario.

It is worth mentioning that, besides other examples of variability observed in the optical spectra of BHT – of which *Swift* J1357.2−0933 displays one of the most dramatic cases – growing evidence for a qualitatively similar phenomenology is being found in supermassive black holes (including the so-called *changing look quasars*). For instance, Vivek, Srianand & Dawson (2018) observed broad transient absorptions in optical spectra of the quasar SDSS J133356.02+001229, varying on time-scales from a few days to years. This was interpreted as being produced by clouds crossing the line of sight in a corotating clumpy wind. Despite the fact that analogies between observables in stellar mass and supermassive black holes need to be taken with caution, these observations might suggest that similar clumpy winds are common across a wide range of black hole masses.

Finally, during the review process of this work a paper presenting consistent phenomenology with that reported here was published by Charles et al. (2019).

5 CONCLUSIONS

We have presented photometric and spectroscopic observations of *Swift* J1357.2−0933 during the decay of its 2017 outburst. In agreement with previous studies, we detect the presence of optical dips with a recurrence time that gradually increases throughout the outburst. The dips have a blue colour and its evolution resembles that observed in the 2011 event (CS13, Paice et al. 2019). Our dip-resolved spectroscopic study indicates the existence of an outflow associated with the appearance of optical dips during the 2017 outburst of the black hole transient *Swift* J1357.2−0933. We interpret the optical dips as produced by a clumpy and dense equatorial wind. Within this scenario, the detection of dips is strongly dependent on orbital inclination. Therefore, this clumpy equatorial wind might not be a peculiar characteristic of this system but a common phenomenon of accreting stellar mass black holes in outburst.

ACKNOWLEDGEMENTS

We acknowledge support by the Spanish MINECO under grant AYA2017-83216-P. TMD acknowledge support via Ramón y Cajal Fellowships RYC-2015-18148. Based on observations made with the GTC telescope, in the Spanish Observatorio del Roque de los Muchachos of the Instituto de Astrofísica de Canarias, under Director's Discretionary Time. We are thankful to Miriam Garcia for useful discussion.

REFERENCES

Armas Padilla M., Degenaar N., Russell D. M., Wijnands R., 2013, MNRAS, 428, 3083
Armas Padilla M., Wijnands R., Altamirano D., Méndez M., Miller J. M., Degenaar N., 2014, MNRAS, 439, 3908
Astropy Collaboration, 2013, A&A, 558, A33
Begelman M. C., McKee C. F., Shields G. A., 1983, ApJ, 271, 70
Belloni T. M., Motta S. E., Muñoz-Darias T., 2011, Bull. Astron. Soc. India, 39, 409
Beri A. et al., 2019, MNRAS, 485, 3064
Blandford R. D., Königl A., 1979, ApJ, 232, 34
Bohlin R. C., Colina L., Finley D. S., 1995, AJ, 110, 1316
Bradley L. et al., 2019, astropy/photutils: v0.6
Cardelli J. A., Clayton G. C., Mathis J. S., 1989, ApJ, 345, 245
Casares J., 2016, ApJ, 822, 99
Casares J., Marsh T. R., Charles P. A., Martin A. C., Martin E. L., Harlaftis E. T., Pavlenko E. P., Wagner R. M., 1995, MNRAS, 274, 565
Cepa J. et al., 2000, in Iye M., Moorwood A. F., eds, Proc. SPIE Conf. Ser. Vol. 4008, Optical and IR Telescope Instrumentation and Detectors. SPIE, Bellingham, p. 623
Charles P., Matthews J. H., Buckley D. A. H., Gandhi P., Kotze E., Paice J., 2019, MNRAS, 489, L47
Corbel S., Nowak M. A., Fender R. P., Tzioumis A. K., Markoff S., 2003, A&A, 400, 1007
Corral-Santana J. M., Casares J., Muñoz-Darias T., Rodríguez-Gil P., Shahbaz T., Torres M. A. P., Zurita C., Tyndall A. A., 2013, Science, 339, 1048 (CS13)
Díaz Trigo M., Boirin L., 2016, Astron. Nachr., 337, 368
Drake A. J., Djorgovski S. G., Mahabal A. A., Graham M. J., Stern D., Catelan M., Christensen E., Larson S. M., 2017, Astron. Telegram, 10297, 1
Drew J. E., 1990, ApJ, 357, 573
Dubus G., Kim R. S. J., Menou K., Szkody P., Bowen D. V., 2001, ApJ, 553, 307
Fender R., Muñoz-Darias T., 2016, in Haardt F., Gorini V., Moschella U., Treves A., Colpi M., eds, Astrophysical Black Holes, Lecture Notes in Physics, Vol. 905, Springer International Publishing, Switzerland, p. 65
Fitzpatrick E. L., 1999, PASP, 111, 63
Fitzpatrick E. L., 2004, in Witt A. N., Clayton G. C., Draine B. T., eds, ASP Conf. Ser. Vol. 309, Astrophysics of Dust. Astron. Soc. Pac., San Francisco, p. 33
Gallo E., Fender R. P., Pooley G. G., 2003, MNRAS, 344, 60
Gray D. F., ed., 2005, The Observation and Analysis of Stellar Photospheres. Cambridge Univ. Press, Cambridge
Hoare M. G., 1994, MNRAS, 267, 153
Jiménez-Ibarra F. et al., 2019, MNRAS, 484, 2078
Krimm H. A. et al., 2011, Astron. Telegram, 3138, 1
Mata Sánchez D., Muñoz-Darias T., Casares J., Corral-Santana J. M., Shahbaz T., 2015, MNRAS, 454, 2199 (MS15)
Mata Sánchez D. et al., 2018, MNRAS, 481, 2646
Miller J. M., Raymond J., Fabian A., Steeghs D., Homan J., Reynolds C., van der Klis M., Wijnands R., 2006, Nature, 441, 953
Muñoz-Darias T. et al., 2016, Nature, 534, 75
Muñoz-Darias T., Torres M. A. P., Garcia M. R., 2018, MNRAS, 479, 3987
Muñoz-Darias T. et al., 2019, ApJ, 879, L4
Najarro F., Geballe T. R., Figer D. F., de la Fuente D., 2017, ApJ, 845, 127
Neilsen J., Lee J. C., 2009, Nature, 458, 481
O'Donnell J. E., 1994, ApJ, 422, 158
Paice J. A. et al., 2019, MNRAS, 488, 512
Ponti G., Fender R. P., Begelman M. C., Dunn R. J. H., Neilsen J., Coriat M., 2012, MNRAS, 422, L11
Ponti G., Bianchi S., Muñoz-Darias T., De K., Fender R., Merloni A., 2016, Astron. Nachr., 337, 512
Remillard R. A., McClintock J. E., 2006, ARA&A, 44, 49
Shahbaz T., Russell D. M., Zurita C., Casares J., Corral-Santana J. M., Dhillon V. S., Marsh T. R., 2013, MNRAS, 434, 2696
Sundqvist J. O., Puls J., Feldmeier A., Owocki S. P., 2011, A&A, 528, A64
Torres M. A. P., Jonker P. G., Miller-Jones J. C. A., Steeghs D., Repetto S., Wu J., 2015, MNRAS, 450, 4292
van Dokkum P. G., 2001, PASP, 113, 1420
VanderPlas J. T., 2018, ApJS, 236, 16
van der Klis M., 2006, in Lewin W., van der Klis M., eds, Rapid X-ray Variability. Cambridge Univ. Press, Cambridge, p. 39
Vivek M., Srianand R., Dawson K. S., 2018, MNRAS, 481, 5570

This paper has been typeset from a TEX/LATEX file prepared by the author.

5

Conclusions

And in the end the love you take
is equal to the love you make
The end, Lennon-McCartney

In this thesis, we presented an observational study of three transient LMXBs during outburst. On the basis of optical photometry and spectroscopy, we investigated different aspects of the accretion discs in these objects. On the one hand, we estimated some scale parameters, such as the size and the vertical structure of the accretion disc. To this end, we studied the optical and X-ray spectra of the newly discovered system MAXI J1807+132. We combined this information with its optical light curve aiming to constrain some fundamental parameters by comparison with the phenomenology observed in dynamically-solved systems. We found that this transient displays the typical properties of LMXBs in outburst, resembling those seen in systems with short orbital period (i.e. small accretion disc). In addition, we used an extensive spectroscopic campaign of the prototypical NS transient Aquila X-1 to study the Bowen complex and, based on that, determine the accretion disc opening angle. This is a very elusive parameter to measure, and our result supports the standard theoretical models proposed to explain highly-irradiated accretion discs.

On the other hand, we have also studied the occurrence of accretion disc winds and their relation with the accretion processes. We observed the BH optical dipper Swift J1357.2–0933, with unprecedented high time resolution (in the range of 22–37 s) spectroscopy, and we presented conclusive evidence of the wind-like nature of the material producing the dips. Our study reinforces the idea that optical winds are a common feature in BH accretion discs, and that winds in general can be found throughout the entire outburst.

The main conclusions extracted from these works are summarised below:

MAXI J1807+132

- We have carried out an optical and X-ray monitoring campaign of MAXI J1807+132 during the decay of its discovery outburst. We observed broad emission lines characteristic of LMXBs, both in outburst and quiescent optical spectra.

- The optical/X-ray flux ratio, the re-flaring recurrence time (∼6.5 d), and the systemic velocity ($\gamma \sim -150$ km s^{-1}), are consistent with a BH accretor, but the X-ray modelling favours a NS.

- We find similarities between the observed properties of MAXI J1807+132 and those of the short orbital period (5.09 h; Gelino & Harrison, 2003) BH transient GRO J0422+32. Both systems show transitions between optical absorption and emission lines as well as reflares with similar recurrence times.

- MAXI J1807+132 and GRO J0422+32 also have similar optical magnitudes in quiescence ($r \sim 21$), but the latter shows donor spectral features in its spectrum. Thus, the distance to GRO J0422+32 could be taken as a lower limit to that of MAXI J1807+132, placing the latter at >2.5 kpc.

Aquila X-1

- We used the 10.4-m Gran Telescopio Canarias to obtain intermediate resolution spectroscopy of the optical counterpart of the NS transient Aquila X-1 during its 2011, 2013 and 2016 outbursts. We detected the irradiation-induced Bowen complex in all the 65 phase-resolved spectra.

- While Gaussian fitting did not yield conclusive results, our full-orbit coverage allowed us to exploit Doppler mapping techniques to constrain the $K_{\rm em}$ velocity. Based on the N III 4640.64/4641.84 Å components we measured $K_{\rm em} = 102 \pm 6$ km s^{-1} with high significance (13σ). As expected, this value is smaller than the K_2 obtained from NIR spectroscopy during quiescence ($K_2 = 136 \pm 4$ km s^{-1}; Mata Sánchez et al., 2017), since these Bowen components trace the centre of light of the irradiated face of the donor star.

- We performed a Monte Carlo analysis using our $K_{\rm em}$ determination in combination with the K_2 value to determine the accretion disc opening angle and its associated error. We obtain $\alpha = 15.5 \pm 2.5$ deg with a 90 per cent significance level. This is the first time that the opening angle of an accretion disc in outburst is derived from direct spectroscopic measurements.

- Our result favours the irradiation-driven thick disc model (Meyer & Meyer-Hofmeister, 1982) where a fraction of the X-ray emission is absorbed by the outer accretion disc.

Swift J1357.2–0933

- We present high-time resolution optical spectroscopy and imaging of the BH transient Swift J1357.2–0933 during its 2017 outburst. We used the 10.4-m Gran Telescopio Canarias to obtain dip-resolved spectroscopy for the first time.

- We observed recurrent dips resembling those discovered in 2011 (Corral-Santana et al., 2013). The dip properties (i.e. duration and depth) as well as the evolution of the recurrence time are similar in both outbursts. This strongly suggests that the dips are produced by the same phenomenon in both 2011 and 2017.

- During the dips, the spectra are characterised by broad and blue-shifted absorptions in the Balmer and He II lines. These features show core velocities of ∼ –800 km s^{-1} and terminal

velocities approaching ∼3000 km s^{-1}, that is, in the upper-end of wind velocities measured in other BH transients both at optical and X-ray wavelengths. This is a clear indication of the existence of an outflow associated with the appearance of the optical dips.

- Our observations suggest that dips are formed in a dense and clumpy outflow produced near the disc equatorial plane and seen at high inclination. If this is the case, the observation of dips is limited to high inclination systems, which implies that selection effects prevent their detection in most of the BH transients known so far. Thus, the observed optical winds might be a common phenomenon of stellar-mass accreting BHs in outburst and not only a peculiarity of Swift J1357.2–0933.

- We have shown that the observed bluing of the source during a dip is due to a gradual change in the slope of the optical continuum. The obscured continuum might be intrinsically red, perhaps the base of a jet, or due to the fact that the cross-section of the absorbing material increases with wavelength.

Bibliography

Ackermann, M., et al. 2014, Science, 343, 42

Armas Padilla, M., Ueda, Y., Hori, T., Shidatsu, M., & Muñoz-Darias, T. 2017, MNRAS, 467, 290

Astropy Collaboration et al. 2013, A&A, 558, A33

Balbus, S. A., & Hawley, J. F. 1991, ApJ, 376, 214

Beals, C. S. 1929, Monthly Notices of the Royal Astronomical Society, 90, 202

Begelman, M. C., McKee, C. F., & Shields, G. A. 1983, ApJ, 271, 70

Belloni, T., Homan, J., Casella, P., van der Klis, M., Nespoli, E., Lewin, W. H. G., Miller, J. M., & Méndez, M. 2005, A&A, 440, 207

Belloni, T. M., Motta, S. E., & Muñoz-Darias, T. 2011, Bulletin of the Astronomical Society of India, 39, 409

Bianchi, S., Ponti, G., Muñoz-Darias, T., & Petrucci, P.-O. 2017, MNRAS, 472, 2454

Blandford, R. D., & Königl, A. 1979, ApJ, 232, 34

Casares, J. 2015, ApJ, 808, 80

Casares, J., Charles, P. A., Jones, D. H. P., Rutten, R. G. M., & Callanan, P. J. 1991, MNRAS, 250, 712

Casares, J., & Jonker, P. G. 2014, SSRv, 183, 223

Casares, J., Muñoz-Darias, T., Sánchez, D. M., Charles, P. A., Torres, M. A. P., Padilla, M. A., Fender, R. P., & García-Rojas, J. 2019, MNRAS

Casares, J., Steeghs, D., Hynes, R. I., Charles, P. A., & O'Brien, K. 2003, ApJ, 590, 1041

Casella, P., Altamirano, D., Patruno, A., Wijnands, R., & van der Klis, M. 2008, ApJL, 674, L41

Chakravorty, S., Lee, J. C., & Neilsen, J. 2013, MNRAS, 436, 560

Charles, P. A., & Coe, M. J. 2006, Optical, ultraviolet and infrared observations of X-ray binaries, ed. W. H. G. Lewin & M. van der Klis, 215–265

Chaty, S., Charles, P. A., Martí, J., Mirabel, I. F., Rodríguez, L. F., & Shahbaz, T. 2003a, MNRAS, 343, 169

Chaty, S., Haswell, C., Malzac, J., Hynes, R., Shrader, C., & Cui, W. 2003b, Monthly Notices of the Royal Astronomical Society, 346, 689

Coleiro, A., & Chaty, S. 2013, ApJ, 764, 185

Corbel, S., & Fender, R. P. 2002, ApJL, 573, L35

Coriat, M., Fender, R. P., & Dubus, G. 2012, MNRAS, 424, 1991

Corral-Santana, J. M., Casares, J., Muñoz-Darias, T., Bauer, F. E., Martínez-Pais, I. G., & Russell, D. M. 2016, Astronomy & Astrophysics, 587, A61

Corral-Santana, J. M., Casares, J., Muñoz-Darias, T., Rodríguez-Gil, P., Shahbaz, T., Torres, M. A. P., Zurita, C., & Tyndall, A. A. 2013, Science, 339, 1048

Cox, A. 2000, Allen's astrophysical quantities, S&T, 100, 72

Fabian, A. C., Rees, M. J., Stella, L., & White, N. E. 1989, MNRAS, 238, 729

Falcke, H., & Biermann, P. L. 1995, A&A, 293, 665

Faulkner, J., Flannery, B. P., & Warner, B. 1972, ApJL, 175, L79

Fender, R., & Belloni, T. 2012, Science, 337, 540

Fender, R., & Muñoz-Darias, T. 2016, in Lecture Notes in Physics, Berlin Springer Verlag, Vol. 905, Lecture Notes in Physics, Berlin Springer Verlag, ed. F. Haardt, V. Gorini, U. Moschella, A. Treves, & M. Colpi, 65

Fender, R. P. 2001, X-ray Astronomy: Stellar Endpoints, AGN, and the Diffuse X-ray Background, 599, 101

Fender, R. P., Garrington, S. T., McKay, D. J., Muxlow, T. W. B., Pooley, G. G., Spencer, R. E., Stirling, A. M., & Waltman, E. B. 1999, MNRAS, 304, 865

Frank, J., King, A., & Raine, D. 1992, Accretion power in astrophysics.

Frank, J., King, A. R., & Lasota, J.-P. 1987, A&A, 178, 137

Fuchs, Y., et al. 2003, A&A, 409, L35

Gallo, E., Corbel, S., Fender, R. P., Maccarone, T. J., & Tzioumis, A. K. 2004, MNRAS, 347, L52

Gallo, E., Fender, R. P., & Pooley, G. G. 2003, MNRAS, 344, 60

Gallo, E., Migliari, S., Markoff, S., Tomsick, J. A., Bailyn, C. D., Berta, S., Fender, R., & Miller-Jones, J. C. A. 2007, The Astrophysical Journal, 670, 600

Galloway, D. K., Muno, M. P., Hartman, J. M., Psaltis, D., & Chakrabarty, D. 2008, ApJS, 179, 360

Gandhi, P., et al. 2017, Nature Astronomy, 1, 859

Gatuzz, E., Díaz Trigo, M., Miller-Jones, J. C. A., & Migliari, S. 2019, MNRAS, 482, 2597

Gelino, D. M., & Harrison, T. E. 2003, ApJ, 599, 1254

Gelino, D. M., Harrison, T. E., & McNamara, B. J. 2001, AJ, 122, 971

Giacconi, R., Gursky, H., Paolini, F. R., & Rossi, B. B. 1962, Physical Review Letters, 9, 439

Gilfanov, M., & Revnivtsev, M. 2005, Astronomische Nachrichten, 326, 812

Grimm, H.-J., Gilfanov, M., & Sunyaev, R. 2002, A&A, 391, 923

Heil, L. M., Vaughan, S., & Uttley, P. 2012, Monthly Notices of the Royal Astronomical Society, 422, 2620

Homan, J., Wijnands, R., van der Klis, M., Belloni, T., van Paradijs, J., Klein-Wolt, M., Fender, R., & Méndez, M. 2001, ApJS, 132, 377

Horne, K., & Marsh, T. R. 1986, MNRAS, 218, 761

Hynes, R. I., et al. 2003, MNRAS, 345, 292

Jimenez-Ibarra, F., Munoz-Darias, T., Casares, J., Armas Padilla, M., & Corral-Santana, J. M. 2019, The Astronomer's Telegram, 12867

Jonker, P. G., & van der Klis, M. 2001, ApJL, 553, L43

Justham, S., Rappaport, S., & Podsiadlowski, P. 2006, MNRAS, 366, 1415

Kalogera, V., & Baym, G. 1996, ApJL, 470, L61

Kalogera, V., & Webbink, R. F. 1996, ApJ, 458, 301

King, A. L., Miller, J. M., Raymond, J., Reynolds, M. T., & Morningstar, W. 2015, ApJL, 813, L37

King, A. R., Kolb, U., & Burderi, L. 1996, ApJL, 464, L127

King, A. R., & Ritter, H. 1999, MNRAS, 309, 253

Krimm, H. A., et al. 2011, The Astronomer's Telegram, 3138

—. 2013, ApJS, 209, 14

Krzemiński, W. 1965, ApJ, 142, 1051

Kunte, P. K., Durgaprasad, N., Gokhale, G. S., Iyengar, V. S., Manchanda, R. K., & Sreekantan, B. V. 1973, Nature Physical Science, 245, 37

Kuulkers, E., et al. 2007, A&A, 466, 595

Lasota, J.-P. 2001, New Astronomy Reviews, 45, 449

Lattimer, J. M., & Prakash, M. 2007, PhR, 442, 109

Lin, D., Remillard, R. A., & Homan, J. 2007, The Astrophysical Journal, 667, 1073

Liu, Q. Z., van Paradijs, J., & van den Heuvel, E. P. J. 2006, A&A, 455, 1165

—. 2007, Astronomy & Astrophysics, 469, 807

Marsh, T. R. 2001, in Lecture Notes in Physics, Berlin Springer Verlag, Vol. 573, Astrotomography, Indirect Imaging Methods in Observational Astronomy, ed. H. M. J. Boffin, D. Steeghs, & J. Cuypers, 1

Marsh, T. R., & Horne, K. 1988, MNRAS, 235, 269

Mata Sánchez, D., Muñoz-Darias, T., Casares, J., Corral-Santana, J. M., & Shahbaz, T. 2015, MNRAS, 454, 2199

Mata Sánchez, D., Muñoz-Darias, T., Casares, J., & Jiménez-Ibarra, F. 2017, MNRAS, 464, L41

Mata Sánchez, D., et al. 2018, MNRAS, 481, 2646

Matsuoka, M., et al. 2009, PASJ, 61, 999

McClintock, J. E., Canizares, C. R., & Tarter, C. B. 1975, ApJ, 198, 641

McClintock, J. E., & Remillard, R. A. 2006, Black hole binaries, ed. W. H. G. Lewin & M. van der Klis, 157–213

Meyer, F., & Meyer-Hofmeister, E. 1982, A&A, 106, 34

Migliari, S., Tomsick, J. A., Maccarone, T. J., Gallo, E., Fender, R. P., Nelemans, G., & Russell, D. M. 2006, ApJL, 643, L41

Mirabel, I. F., & Rodríguez, L. F. 1994, Nature, 371, 46

Mitsuda, K., et al. 1984, PASJ, 36, 741

Miyamoto, S., Iga, S., Kitamoto, S., & Kamado, Y. 1993, ApJL, 403, L39

Miyamoto, S., Kitamoto, S., Hayashida, K., & Egoshi, W. 1995, ApJL, 442, L13

Miyamoto, S., Kitamoto, S., Iga, S., Negoro, H., & Terada, K. 1992, ApJL, 391, L21

Muñoz-Darias, T. 2009, PASP, 121, 935

Muñoz-Darias, T., Casares, J., & Martínez-Pais, I. G. 2005, ApJ, 635, 502

Muñoz-Darias, T., Casares, J., O'Brien, K., Steeghs, D., Martínez-Pais, I. G., Cornelisse, R., & Charles, P. A. 2009, MNRAS, 394, L136

Muñoz-Darias, T., Fender, R. P., Motta, S. E., & Belloni, T. M. 2014, MNRAS, 443, 3270

Muñoz-Darias, T., Motta, S., & Belloni, T. M. 2011, MNRAS, 410, 679

Muñoz-Darias, T., Torres, M. A. P., & Garcia, M. R. 2018, MNRAS, 479, 3987

Muñoz-Darias, T., et al. 2016, Nature, 534, 75

—. 2019, ApJL, 879, L4

Narayan, R., & Heyl, J. S. 2002, ApJL, 574, L139

Neilsen, J., & Lee, J. C. 2009, Nature, 458, 481

Orosz, J. A., Remillard, R. A., Bailyn, C. D., & McClintock, J. E. 1997, ApJL, 478, L83

Osaki, Y. 1974, PASJ, 26, 429

Paczyński, B. 1965, AcA, 15, 305

Paczyński, B. 1971, Annual Review of Astronomy and Astrophysics, 9, 183

Paczyński, B. 1976, in IAU Symposium, Vol. 73, Structure and Evolution of Close Binary Systems, ed. P. Eggleton, S. Mitton, & J. Whelan, 75

Paice, J. A., et al. 2019, MNRAS, 488, 512

Pavlenko, E. P., Martin, A. C., Casares, J., Charles, P. A., & Ketsaris, N. A. 1996, MNRAS, 281, 1094

Podsiadlowski, P., & Rappaport, S. 2000, ApJ, 529, 946

Ponti, G., Bianchi, S., Muñoz-Darias, T., De, K., Fender, R., & Merloni, A. 2016, Astronomische Nachrichten, 337, 512

Ponti, G., Fender, R. P., Begelman, M. C., Dunn, R. J. H., Neilsen, J., & Coriat, M. 2012, MNRAS, 422, L11

Pringle, J. E. 1981, Annual Review of Astronomy and Astrophysics, 19, 137

Rahoui, F., Chaty, S., Rodriguez, J., Fuchs, Y., Mirabel, I. F., & Pooley, G. G. 2010, ApJ, 715, 1191

Reid, M. J., McClintock, J. E., Steiner, J. F., Steeghs, D., Remillard, R. A., Dhawan, V., & Narayan, R. 2014, ApJ, 796, 2

Reynolds, A. P., Quaintrell, H., Still, M. D., Roche, P., Chakrabarty, D., & Levine, S. E. 1997, MNRAS, 288, 43

Rhoades, C. E., & Ruffini, R. 1974, Physical Review Letters, 32, 324

Russell, D. M., Fender, R. P., Hynes, R. I., Brocksopp, C., Homan, J., Jonker, P. G., & Buxton, M. M. 2006, MNRAS, 371, 1334

Russell, D. M., et al. 2013, MNRAS, 429, 815

Salpeter, E. E. 1964, ApJ, 140, 796

Sandage, A., et al. 1966, ApJ, 146, 316

Schreier, E., Levinson, R., Gursky, H., Kellogg, E., Tananbaum, H., & Giacconi, R. 1972, ApJL, 172, L79

Shahbaz, T., & Kuulkers, E. 1998, MNRAS, 295, L1

Shahbaz, T., Zurita, C., Casares, J., Dubus, G., Charles, P. A., Wagner, R. M., & Ryan, E. 2003, ApJ, 585, 443

Shakura, N. I., & Sunyaev, R. A. 1973, A&A, 24, 337

Shidatsu, M., Nakahira, S., Murata, K. L., Adachi, R., Kawai, N., Ueda, Y., & Negoro, H. 2019, ApJ, 874, 183

Shklovsky, I. S. 1967, ApJL, 148, L1

Smak, J. 1969, AcA, 19, 155

Smak, J. 1971, AcA, 21, 15

—. 1984, AcA, 34, 93

Smith, D. A., & Dhillon, V. S. 1998, MNRAS, 301, 767

Steeghs, D. 2003, MNRAS, 344, 448

Steeghs, D., & Casares, J. 2002, The Astrophysical Journal, 568, 273

Steeghs, D., McClintock, J. E., Parsons, S. G., Reid, M. J., Littlefair, S., & Dhillon, V. S. 2013, ApJ, 768, 185

Syunyaev, R. A., & Shakura, N. I. 1986, Soviet Astronomy Letters, 12, 117

Tetarenko, B. E., Lasota, J.-P., Heinke, C. O., Dubus, G., & Sivakoff, G. R. 2018, Nature, 554, 69

Thorsett, S. E., & Chakrabarty, D. 1999, ApJ, 512, 288

Torres, M. A. P., Callanan, P. J., Garcia, M. R., Zhao, P., Laycock, S., & Kong, A. K. H. 2004, ApJ, 612, 1026

Torres, M. A. P., Casares, J., Jiménez-Ibarra, F., Muñoz-Darias, T., Armas-Padilla, M., Jonker, P. G., & Heida, M. 2019, arXiv e-prints

van Paradijs, J., & McClintock, J. E. 1995, X-ray Binaries, 58

Van Paradijs, J., & Verbunt, F. 1984, in American Institute of Physics Conference Series, Vol. 115, American Institute of Physics Conference Series, ed. S. E. Woosley, 49–62

von Zeipel, H. 1924, MNRAS, 84, 665

Vrtilek, S. D., Raymond, J. C., Garcia, M. R., Verbunt, F., Hasinger, G., & Kurster, M. 1990, A&A, 235, 162

Wade, R. A., & Horne, K. 1988, ApJ, 324, 411

Wang, L., Steeghs, D., Casares, J., Charles, P. A., Muñoz-Darias, T., Marsh, T. R., Hynes, R. I., & O'Brien, K. 2017, MNRAS, 466, 2261

White, N. E., & Mason, K. O. 1985, SSRv, 40, 167

Zel'dovich, Y. B. 1964, Soviet Physics Doklady, 9, 195

Zurita, C., Casares, J., & Shahbaz, T. 2003, ApJ, 582, 369

A

Differential aperture photometry procedure

In this appendix we describe the differential aperture photometry procedure used in the analysis of the photometric data presented in this thesis. The code was written with the aim of dealing efficiently with a large number of images. In particular, it was developed to be used in the work presented in Chapter 4, when up to 3000 images were analysed.

Differential photometry

The instrumental magnitude in a given band, $m_{\rm inst}(\lambda)$, is defined as:

$$m_{\rm inst}(\lambda) = -2.5 \log f_\lambda + K$$

where f_λ is the number of counts per second from the object in the observed band, and K is a constant which depends on the observing system (i.e. detector, telescope, and filter), the atmospheric conditions, and the elevation of the object (i.e. airmass).

In order to compare observations from different instruments, it is mandatory to transform the instrumental magnitude to a standard photometric system, which is defined based on a set of filters and calibration stars. The equation to transform instrumental into apparent magnitudes (m_λ) is given by:

$$m_\lambda = m_{\rm inst} + k_1 + k_2 C + k_3 \chi \tag{A.1}$$

where C is the colour of the object in the standard system and χ its airmass. The coefficients k_1, k_2, and k_3 express the sensitivity of the system (telescope/detector), the colour term, and the atmospheric extinction coefficient, respectively. They are determined by solving Eq. A.1 using observations of a set of stars whose magnitudes and colours are known in the standard system. It is worth noting that Eq. A.1 can only be applied provided that the observations are made under photometric conditions (i.e. without clouds and dust, and with a stable seeing).

Alternatively, photometric data can be obtained in a non-photometric night by applying differential photometry. This technique is based on measuring the magnitude of an object by comparison with that of a field star taken at the same time. Let's suppose two stars: a target and a comparison, field star. By applying Eq. A.1 to both and subtracting one from the other we obtain:

$$m_\lambda - m^*_\lambda = m_{\rm inst} - m^*_{\rm inst} + k_2 \left(C - C^*\right) + k_3 \left(\chi - \chi^*\right)$$

where asterisks refer to the comparison star. If both the target and the comparison star have similar colours and are close to each other (i.e. a few arcmin), the colour (k_2) and extinction (k_3) terms in the latter expression can be neglected, obtaining:

$$m_\lambda - m^*_\lambda = m_{\rm inst} - m^*_{\rm inst} \tag{A.2}$$

In addition, if the true magnitude of the comparison (m^*_λ) is known, the calibrated magnitude of the target can be determined using Eq. A.2 by measuring the instrumental magnitudes of the target and the comparison star.

Python procedure

All the photometric data presented in this thesis were obtained following the technique described above and reduced using a PYTHON procedure based on the ASTROPY-PHOTUTILS package (Astropy Collaboration et al., 2013). Initially, we developed the code to analyse data from RISE, the fast-readout camera attached to the 2-m Liverpool Telescope on La Palma. Nevertheless, other instruments were later included: ACAM (the Auxiliary-port Camera) attached to the 4.2-m William Herschel Telescope, and the acquisition images of OSIRIS (Optical System for Imaging and low-Intermediate-Resolution Integrated Spectroscopy) on the Gran Telescopio Canarias, both also on La Palma.

The routine performs aperture photometry, that is, the sum of the counts within a circular area centred on the object, and subtracts the local background, which is estimated within a annulus around it. In this way, the instrumental magnitude is determined by:

$$m_{\rm inst} = -2.5 \log \left(\Sigma C_\star - A \bar{C}_{\rm b} \right) / t_{\rm exp}$$

where $\Sigma C_\star$ are the counts contained in the central aperture of area A, $\bar{C}_{\rm b}$ is the median background counts per pixel, and $t_{\rm exp}$ is the exposure time. The routine can take up to four field stars in order to determine the flux calibration. The error of the measured magnitudes are computed following the same method as in the commonly used IRAF-PHOT task [1]. Our procedure has the advantage of being able to handle a large number of images with minimal user intervention. It also provides a graphic interface for the users to interact intuitively. The main steps followed are summarised below (see also the flowchart in Fig. A.1):

Input. In addition to the reduced science images, the program requires the celestial coordinates of the target and at least one comparison star. For the latter, the magnitude and its associated error are also needed as input. The science images are expected to be astrometrised. However, in case no astrometric solution exists both target and calibration stars can be interactively selected from an image preview.

Re-centring. The centroid position of both the target and the comparison stars are computed by Gaussian fits. In those cases where the target is too faint and no reliable centroid can be achieved by Gaussian fitting, its position can be measured relative to the fitted positions of the calibration stars.

[1] http://iraf.noao.edu/scripts/irafhelp?phot

Seeing determination. The aperture sizes (both the central aperture and sky annulus) are defined according to the seeing. For that purpose, the seeing is determined by using the nearby stars within a radius around the target that is defined by the user. By default, the central aperture has a radius of 1.25×seeing, however, this value can be modified.

Sky determination. The background value is determined by analysing an annuls around the central aperture. By default, this annulus is 5 pixels wide and its inner radius is set at 3.5×seeing from the centre of the aperture. As in the case of the central aperture, both the annulus radius and width can be defined by the user. The number of counts per pixel of the sky is estimated from the median value within the annulus aperture, computed using a sigma-clipping statistic algorithm in order to reject outliers due to e.g. the contamination from a nearby star, cosmic ray hits, saturated pixels, etc.

Output. In addition to the target magnitude (and its associated error), the procedure also produces a set of control images where the apertures and the sky statistics for each processed image can be visualised (see Fig. A.2).

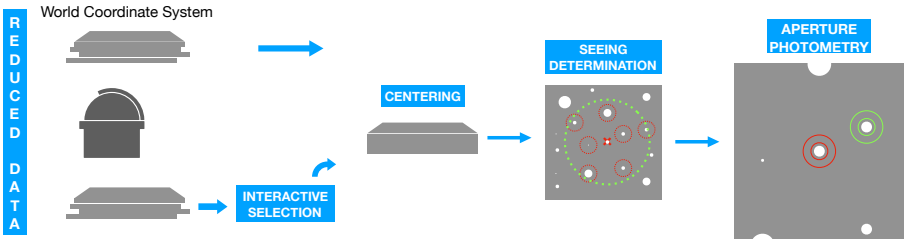

FIGURE A.1— Flowchart describing the main steps of the procedure.

The program was used in two of the works presented in this thesis (Chapter 2 and Chapter 4), but also in other works published by our team. As part of the potential improvements, we plan to include PSF photometry, which is a suitable technique for crowded fields.

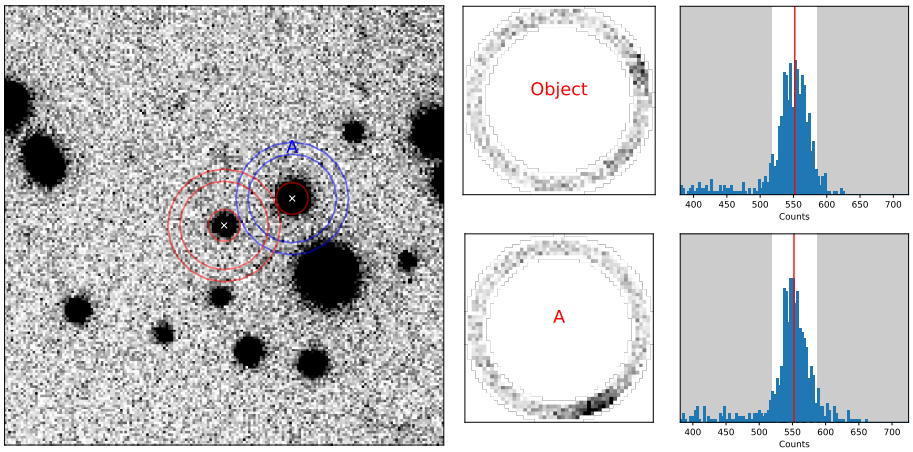

FIGURE A.2— Example of the control images produced by the task. Left: the apertures used in the photometry are displayed; red for the target aperture and blue for the calibration star (the latter labelled as A). The centroids are indicated with white crosses. Middle: background determination for the target (top) and the calibrations star (bottom). Right: the distributions of the number of counts are represented in blue. The vertical red line marks the sigma-clipped median, while grey areas indicate the excluded values ($> 2\sigma$).